



# Proton-conducting solid acid electrolytes based upon $\text{MH}(\text{PO}_3\text{H})$

( $\text{M} = \text{Li}^+, \text{Na}^+, \text{K}^+, \text{Rb}^+, \text{Cs}^+, \text{NH}_4^+$ )

Weihoa Zhou  
University of Twente

Proton-conducting solid acid electrolytes

based upon  $\text{MH}(\text{PO}_3\text{H})$

( $\text{M} = \text{Li}^+, \text{Na}^+, \text{K}^+, \text{Rb}^+, \text{Cs}^+, \text{NH}_4^+$ )

**Graduation committee:**

Chairman:	prof. dr. G. van der Steenhoven	University of Twente
Promotor:	prof. dr. ir. A. Nijmeijer	University of Twente
Assistant promotor:	dr. H.J.M. Bouwmeester	University of Twente
Committee members:	dr. B.A. Boukamp	University of Twente
	prof. dr. M.C. Elwenspoek	University of Twente
	dr. G.J.M. Janssen	ECN, Petten
	prof. dr. ir. L. Lefferts	University of Twente
	prof. dr. M. Stoukides	Aristotle University of Thessaloniki, Greece

The research described in this thesis was carried out in the Inorganic Membranes group and the MESA+ Institute of Nanotechnology at the University of Twente, Enschede, the Netherlands. This project was financially supported by the Dutch Technology Foundation STW (project number: TPC 6611).

Proton-conducting solid acid electrolytes based upon  $\text{MH}(\text{PO}_3\text{H})$

( $\text{M} = \text{Li}^+, \text{Na}^+, \text{K}^+, \text{Rb}^+, \text{Cs}^+, \text{NH}_4^+$ )

Weihua Zhou, PhD Thesis, University of Twente, the Netherlands

ISBN: 978-90-365-3149-8

DOI: 10.3990/1.9789036531498

Cover designed by Xinfu Xu and Danchao Hu

Copyright © 2011 by Weihua Zhou, Enschede, the Netherlands

All rights reserved.

PROTON-CONDUCTING SOLID ACID  
ELECTROLYTES BASED UPON  $\text{MH}(\text{PO}_3\text{H})$   
( $\text{M} = \text{Li}^+, \text{Na}^+, \text{K}^+, \text{Rb}^+, \text{Cs}^+, \text{NH}_4^+$ )

DISSERTATION

to obtain  
the doctor's degree at the University of Twente,  
on the authority of the rector magnificus,  
prof. dr. H. Brinksma,  
on account of the decision of the graduation committee,  
to be publicly defended  
on Wednesday, 2<sup>nd</sup> of February, 2011 at 16:45 hrs.

by

Weihua Zhou  
born on 1<sup>st</sup> of January, 1978  
in Beijing, China

This dissertation has been approved by,

Promotor :                      prof. dr. ir. A. Nijmeijer

Assistant promotor :        dr. H.J.M. Bouwmeester

- To the persons who love me and whom I love.

天生我材必有用，千金散尽还复来。

《将进酒》 李白



# Table of Contents

<b>1 Introduction</b>	1
1.1 Introduction	2
1.2 Proton-conducting electrolytes	2
1.2.1 Polymer and hybrid organic-inorganic proton conductors	3
1.2.2 Inorganic proton conductors	6
1.3 Solid acid proton conductors	7
1.4 Fuel cells	11
1.5 Scope of this thesis	13
References	15
<b>2 Superprotonic phase transitions in solid acid phosphites <math>MH(PO_3H)</math> (<math>M = Li^+, Na^+, K^+, Rb^+, Cs^+, NH_4^+</math>)</b>	17
2.1 Introduction	18
2.2 Experimental	19
2.3 Results and discussion	20
2.3.1 Phase analysis	20
2.3.2 Impedance measurements	26
2.4 Conclusions	30
References	31
<b>3 Proton conductivity of composite electrolytes <math>KH(PO_3H)-SiO_2</math></b>	33
3.1 Introduction	35
3.2 Experimental	36
3.3 Results and discussion	38
3.3.1 X-Ray powder diffraction and thermal analysis	38
3.3.2 Impedance measurements	42
3.3.3 Stability measurements	46
3.3.4 Thin film composite electrolyte	47
3.4 Conclusions	49
References	51
<b>4 Superprotonic phase transitions in solid solutions <math>K_xCs_{1-x}H(PO_3H)</math> and <math>K_x(NH_4)_{1-x}H(PO_3H)</math></b>	53



4.1	Introduction	55
4.2	Experimental	56
4.3	Results and discussions	57
4.3.1	Phase analysis by X-ray powder diffraction	57
4.3.2	Thermal analysis	60
4.3.3	AC impedance spectroscopy	63
4.4	Summary and conclusions	65
	References	67

## **5 The effect of humidification on the electrochemical performance of Pt/KH(PO<sub>3</sub>H) electrodes for solid acid-based fuel cells**

		69
5.1	Introduction	71
5.2	Experimental	72
5.2.1	Preparation of electrolyte/electrode assembly	72
5.2.2	Impedance measurements	73
5.3	Results	75
5.3.1	Electrode microstructure	75
5.3.2	Impedance spectroscopy	75
5.4	Discussion	76
5.4.1	Analysis of impedance spectra	76
5.4.2	Electrolyte resistance	79
5.4.3	Electrode impedance	82
5.5	Conclusions	85
	References	87
	Appendix	89

## **6 Outlook and recommendations**

	References	99
--	------------	----

## **Appendix: Reverse microemulsion synthesis of nano sized CsHSO<sub>4</sub>**

A.1	Introduction	102
A.2	Experimental	103
A.2.1	Reveries microemulsion	103
A.2.2	Characterizations	104
A.3	Results and discussions	105

A.3.1	Microemulsion synthesis	105
A.3.2	Proton conductivity	113
A.4	Conclusions	113
References		114
<b>Summary</b>		117
<b>Samenvatting</b>		121
<b>Acknowledgements</b>		127



## 1 Introduction

### *Abstract*

*In this chapter different classes of proton-conducting electrolytes are presented, with special emphasis on solid acids. A brief introduction into fuel cells and the scope of this thesis are given as well.*

### **1.1 Introduction**

A hydrogen-based fuel cell is an electrochemical device that produces electricity from separate hydrogen (fuel) and oxygen (oxidant) gas streams, with water and heat as by-products. Fuel cells are different from conventional combustion-based power plants, which convert chemical energy into thermal energy (which is transformed to kinetic energy and, subsequently, to electrical energy). Consequently, fuel cells have a high theoretical efficiency, approximately 83 % [1], implying that almost all chemical energy is converted into electrical energy. Because of their high fuel efficiencies, widespread implementation of fuel cells aids to solutions for the energy and climate change crisis. For this reason, research projects on fuel cells have received significant amounts of support in some developed countries. One of the key components of a fuel cell is the electrolyte, a material that conducts ions. In this chapter, different classes of proton-conducting electrolytes and a brief introduction into fuel cells are presented.

### **1.2 Proton-conducting electrolytes**

Interest in proton conduction arose from the discovery of proton conductivity in ice one hundred years ago [2]. As a special type of ionic conductor, proton conductors are applicable to numerous electrochemical devices, such as fuel cells, chemical sensors, batteries, hydrogen pumps, etc. [2]. To date, a large number of proton-conducting electrolytes has been investigated, and different mechanisms of proton conduction have been identified. In the following, a brief overview of state-of-the-art proton-conducting electrolytes is given. It is considered beyond the scope of this chapter to give a comprehensive review of proton-conductors as excellent reviews in this highly active field are provided

by Colombaro [2], Kreuer [3], Iwahara *et al.* [4], Phair and Badwal [5], and Malavasi *et al.* [6].

### 1.2.1 Polymer and hybrid organic-inorganic proton conductors

Nafion<sup>®</sup> is the primary choice for use as electrolyte in low-temperature fuel cells. Its structure consists of a perfluorinated backbone with side chains terminated by strongly acidic -SO<sub>3</sub>H groups, as shown in Figure 1.1. The cluster-channel or cluster-network model provides a conceptual basis for rationalizing the properties of Nafion<sup>®</sup>, especially ionic and water transport [2]. The model describes the hydrophilic sulfonate ion clusters as inverted micelles,

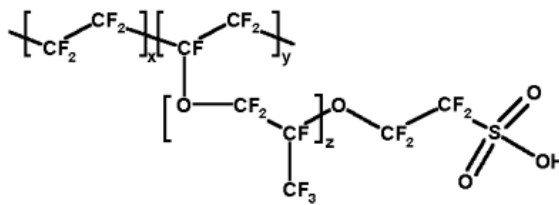


**Figure 1.1** Structure of Nafion<sup>®</sup> Ref. 7.

40 Å in diameter, distributed within a continuous, hydrophobic fluorocarbon lattice [7]. Narrow pores or channels, about 10 Å in diameter, interconnect the clusters, as shown schematically in Figure 1.2. Alternative models proposed in

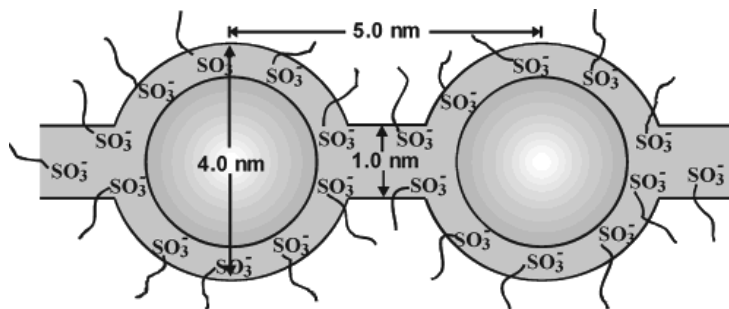


**Figure 1.2** Cluster network model for Nafion<sup>®</sup> [7]

literature include the core-shell, rod and water-channel models. For more details, see references 7 and 8. Both the water content and the concentration of sulfonic sites determine the magnitude of the proton conductivity. Proton transport in Nafion<sup>®</sup> occurs by a vehicle mechanism, in which the water molecules, forming hydronium ions, carry the protons to adjacent sulfonic sites. In the absence of water, *i.e.*, under dry conditions, or above ~80 °C, the predominant proton transport mechanism is the direct hopping between sulfonic sites (Grotthuss mechanism). Under these conditions Nafion<sup>®</sup> and other perfluorosulfonic ionomers significantly lose proton conductivity and mechanical stability.

Blends of inorganic oxo-acids H<sub>3</sub>PO<sub>4</sub> and H<sub>2</sub>SO<sub>4</sub> in polymers with basic sites have been studied, aiming at developing anhydrous proton-conducting hybrid inorganic-organic polymer electrolytes. In these materials, the oxo-acid is confined within the polymeric phase. Probably, polyethylene oxide (PEO) blended with phosphoric acid, PEO-H<sub>3</sub>PO<sub>4</sub>, has been studied most extensively [9-11]. At room temperature, its proton conductivity is poor, about 10<sup>-5</sup> S cm<sup>-1</sup> [12]. Under dry conditions, PEO-H<sub>3</sub>PO<sub>4</sub> shows a temperature dependent conductivity, which satisfies the VTF (Vogel- Tamma-Fulcher) equation [9]

$$\sigma = \sigma_0 \exp\left(\frac{-B}{T - T_0}\right) \quad (1.1)$$

where  $\sigma_0$  is a constant,  $B$  the pseudo activation energy, and  $T_0$  the critical (ideal glass transition) temperature. NMR studies demonstrated the temperature-dependent conductivity in PEO-H<sub>3</sub>PO<sub>4</sub> to be governed by segmental motions of the polymer chains [9]. In general, the proton conductivity of acid-blended polymers strongly depends on the nature of both polymer and acid, and on the acid concentration. At high acid concentrations, when all basic sites are protonated, conduction is supposed to occur along mixed SO<sub>4</sub><sup>2-</sup>/HSO<sub>4</sub><sup>-</sup> and

$\text{HPO}_4^{2-}/\text{H}_2\text{PO}_4^-$  hydrogen-bonded anion chains (Grotthuss mechanism), in a manner which bears resemblance to proton transport in solid acids, like  $\text{CsHSO}_4$  [2].

In recent years, research has been redirected to basic polymers with an aromatic backbone structure, which demonstrate excellent thermal and chemical stability at elevated temperature. Among them, thermoplastic polybenzimidazole (PBI) has appealed significant interest. While PBI, both in its pure and sulfonated form, exhibits poor conductivity, excellent conductivities are reported for hybrid membranes formed from PBI and several oxo-acids [13]. So far the most successful one is the system PBI with phosphoric acid (PBI- $\text{H}_3\text{PO}_4$ ). Phosphoric acid is known to exhibit high intrinsic proton conduction due to self-dissociation (autoprotolysis) as discussed above. A strong acid/base interaction in the hybrid membrane (between the benzimidazole group and the first acid layer) is responsible for partial immobilization of the acid [14]. At very small acid contents, when all the acid is immobilized, the conductivity is poor. The conductivity increases if the content of the confined oxo-acid increases. If, however, the acid content is too high, this leads to a soft paste, unsuitable to be processed in the form of a membrane. Much progress has been made during the last decade in polymer synthesis and membrane fabrication (for a recent review, see Ref. 15). Although a number of issues still needs to be addressed, there is general consensus in literature that the PBI- $\text{H}_3\text{PO}_4$  based membranes show great promise for use as electrolyte in fuel cells. This is mainly motivated by their low-cost, chemical and mechanical stability, and ability to operate at temperatures above  $\sim 120^\circ\text{C}$  up to  $\sim 200^\circ\text{C}$  without significant humidification of reactant gases [16]. The elevated operating temperature simplifies thermal management of the fuel cell and, most importantly, greatly increases the CO tolerance of commonly used Pt-based anode and cathode electrocatalysts.



### 1.2.2 Inorganic proton conductors

The use of water-containing or hydrated compounds restricts application to low temperature, as the proton conductivity is highly related to the water content. Of notable interest are oxo-acid salts and solid oxides, which show anhydrous proton transport at elevated temperature.

Oxo-acid salts or solid acids are partially neutralized polyprotic acids, such as  $\text{CsHSO}_4$  and  $\text{CsH}_2\text{PO}_4$ , which exhibit high proton conductivities of the order of  $10^{-3} - 10^{-2} \text{ S cm}^{-1}$  in the range of temperature  $120 - 300 \text{ }^\circ\text{C}$  [17]. The solid nature, elevated operating temperature and anhydrous proton transport mechanism render them inherently advantageous over liquid and polymeric electrolytes. As this thesis focuses on the potential application of solid acids in fuel cells, the properties of solid acids are separately discussed in Section 1.3.

Numerous reports have been made during the last two decades of high proton conductivities, typically  $10^{-3} - 10^{-2} \text{ S cm}^{-1}$  at  $600 - 1000 \text{ }^\circ\text{C}$ , in perovskite-structured cerates and zirconates [3, 18, 19]. Pure  $\text{BaCeO}_3$ ,  $\text{SrCeO}_3$ ,  $\text{CaZrO}_3$  and  $\text{SrZrO}_3$  show little proton incorporation unless doped with subvalent cations, typically  $\text{Y}^{3+}$  or  $\text{Yb}^{3+}$ . Doping is charge compensated by the formation of oxygen vacancies. These play an essential role in proton conduction in the oxides [20]. As water dissociates at the oxide surface, mobile protons are created by incorporation of the formed hydroxyl ion into the oxygen vacancy, and the proton forming a covalent bonding with lattice oxygen. Of the listed materials, the derivatives of  $\text{SrCeO}_3$  and  $\text{BaCeO}_3$  display the highest proton conductivities. Major drawback in the use of the cerates, however, is their poor chemical stability in  $\text{CO}_2$ -containing atmospheres [18]. The latter has strongly stimulated research on acceptor-doped niobates and tantalates of general formulae  $\text{RE}_{1-x}\text{A}_x\text{MO}_4$ , where  $\text{RE} = \text{La, Gd, Nd, Tb, or Y}$ ,  $\text{M} = \text{Nb or Ta}$ ,  $\text{A} = \text{Ca, Sr or Ba}$ , and  $x = 0.01 - 0.05$ . Though showing somewhat lower proton

conductivities than the perovskite-type cerates, these families of materials enable operation as a thin-film electrolyte in CO<sub>2</sub>-containing atmospheres [6].

### 1.3 Solid acid proton conductors

Generally, oxo-acid salts or solid acids can be presented by the general formulae  $M_aH_b(XO_4)_c$ , where M is a monovalent or divalent cation, and  $XO_4$  is a tetrahedral oxy-anion [21]. Possible combinations of tetrahedral oxy-anions and cations occurring in solid acids are listed in Table 1.1.

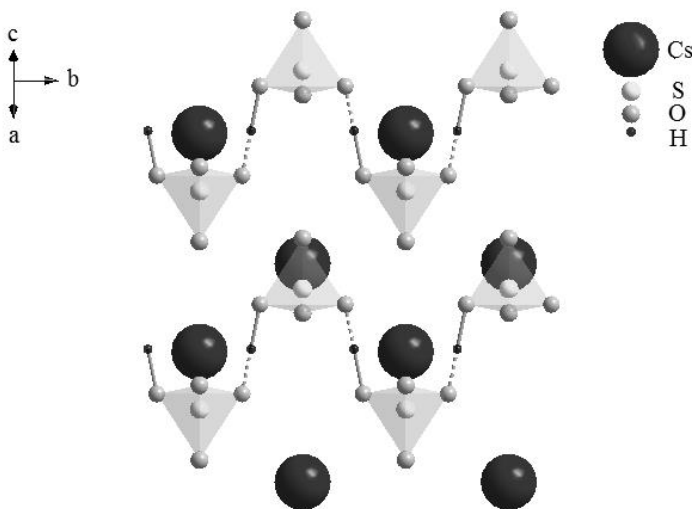
**Table 1.1.** Cations ( $M^{z+}$ ) and tetrahedral oxy-anions ( $XO_4^{z-}$ ) in solid acids.

Table adapted from data in Ref. 21.

Cations		Tetrahedral oxy-anions	
$M^+$	Li <sup>+</sup> , Na <sup>+</sup> , K <sup>+</sup> , Rb <sup>+</sup> , Cs <sup>+</sup> , Tl <sup>+</sup> , NH <sub>4</sub> <sup>+</sup> ,	$XO_4^{2-}$	SO <sub>4</sub> <sup>2-</sup> , SeO <sub>4</sub> <sup>2-</sup> , CrO <sub>4</sub> <sup>2-</sup> , TeO <sub>4</sub> <sup>2-</sup> , MoO <sub>4</sub> <sup>2-</sup> , WO <sub>4</sub> <sup>2-</sup> ,
$M^{2+}$	Be <sup>2+</sup> , Mg <sup>2+</sup> , Ca <sup>2+</sup> , Sr <sup>2+</sup> , Ba <sup>2+</sup> , Pb <sup>2+</sup> ,	$XO_4^{3-}$	PO <sub>4</sub> <sup>3-</sup> , AsO <sub>4</sub> <sup>3-</sup> , VO <sub>4</sub> <sup>3-</sup> , NbO <sub>4</sub> <sup>3-</sup> , MnO <sub>4</sub> <sup>3-</sup> , SbO <sub>4</sub> <sup>3-</sup> ,
		$XO_4^{4-}$	SiO <sub>4</sub> <sup>4-</sup> , GeO <sub>4</sub> <sup>4-</sup> ,

A hydrogen bond exists if one hydrogen atom is bonded to more than one atom, mostly oxygen ions, creating a link between atoms or functional groups [22]. Hydrogen bonds link the oxy-anions in the ordered room temperature structure of the solid acids into infinite chains. In CsHSO<sub>4</sub>, the hydrogen bonds connect the oxy-anions to infinite zigzag chains, as shown in Figure 1.3. As a matter of fact, a wide variety of 0D [23], 1D [24], 2D [25, 26] and 3D [27]

intermolecular networks of hydrogen bonds has been probed in solid acids. A few of them are illustrated in Table 1.2.

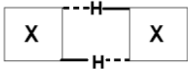
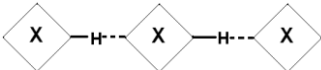
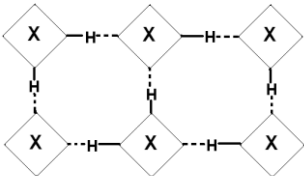
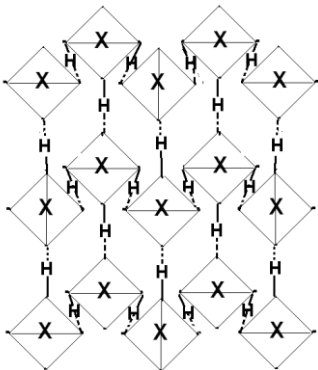


**Figure 1.3** Hydrogen-bonded infinite chains of tetrahedral oxyanions in CsHSO<sub>4</sub>. Dashed line: O••H hydrogen bond; Solid line: O—H covalent bond. Drawn using atomic coordinates listed in Ref. 28.

A key characteristic of the solid acid compounds is that the proton conductivity increases by 2 – 4 orders of magnitude upon a first-order polymorphic phase transition, termed a superprotonic transition, at elevated temperature (Figure 1.4). A disordering of the hydrogen-bonded network occurs to accommodate the change to a structure with higher symmetry. Unlike sulfonated polymers, *e.g.* Nafion<sup>®</sup>, no water molecules are required to enable proton transport, eliminating the problem of humidification of the electrolyte. The transport of protons in the solid acids occurs by hopping to neighboring oxy-anion tetrahedra (Grotthuss mechanism), assisted by rapid reorientations of these oxy-anions in the high-temperature disordered structure. Using supported

thin  $\text{CsH}_2\text{PO}_4$  electrolyte membranes on porous stainless steel gas-diffusion electrodes, peak power densities as high as  $415 \text{ mW cm}^{-2}$  were obtained [29]. This observation highly inspired the work presented in this thesis.

**Table 1.2** Different intermolecular hydrogen-bonded networks in solid acids. Table adapted from data in Ref. 24-28.

Dimensionality	Networks	Examples
0D		$\beta\text{-NaHSO}_4$
1D		$\text{CsHSO}_4$
2D		$\text{Cs}_2(\text{HSO}_4)(\text{H}_2\text{PO}_4)$ $\text{CsH}_2\text{PO}_4$
3D		$\alpha\text{-Cs}_3(\text{HSO}_4)_2(\text{H}_2\text{PO}_4)$

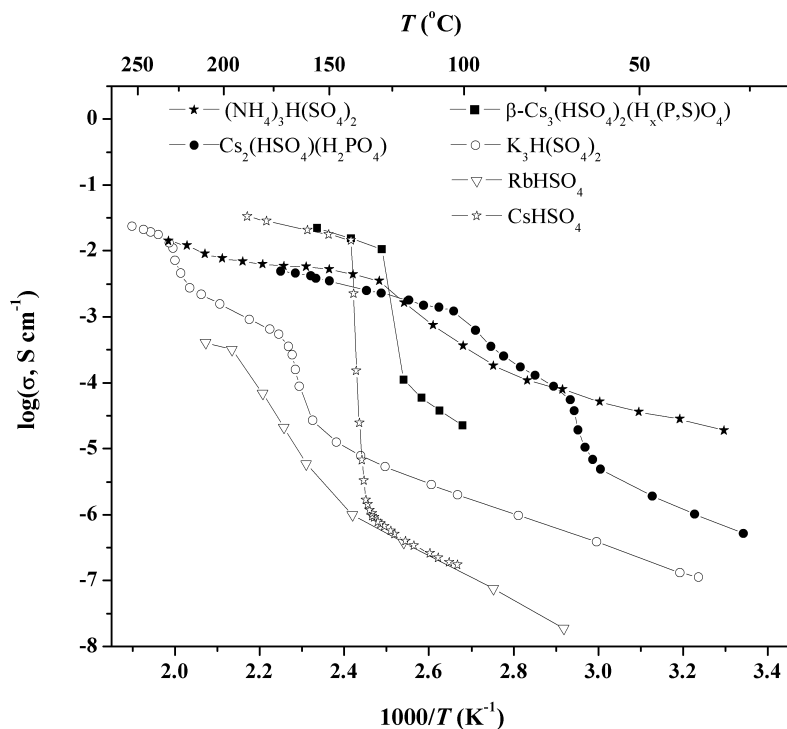
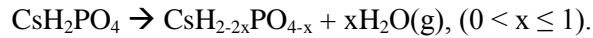


**Figure 1.4** Arrhenius plots of the proton conductivities of selected solid acids. Redrawn from data presented in Ref. 29.

To date, however, widespread implementation of superprotonic solid acids in fuel cells is hindered by a poor thermochemical and mechanical stability of the materials investigated so far (see Chapter 3). The solid acids may be subject to thermal decomposition/dehydration behavior above the superprotonic transition temperature [21, 30-33]. The decomposition process for  $\text{CsHSO}_4$  and  $\text{CsH}_2\text{PO}_4$  can be expressed as



and



respectively. Despite moderate water partial pressures can be used to provide thermal stability, and several laboratories have demonstrated the feasibility of humidity-stabilized solid acid fuel cells [31, 33], the necessity of water management and preventing condensed water from contacting the electrolyte in case of fuel cell shut down complicates their design. In addition, under reducing conditions chemical decomposition of sulfate and selenate solid acids can occur, which is accelerated in the presence of commonly used catalysts, *e.g.* RuO<sub>2</sub>, Pt, Pd, Ir [32].

## 1.4 Fuel cells

Basically, a fuel cell comprises three basic components: the ion-conducting electrolyte, the cathode and the anode, as schematically shown in Figure 1.5. There is an overall driving force for the hydrogen and oxygen to react and to produce water. However, direct combustion of the fuel, *i.e.*, hydrogen, by oxygen is prevented by the electrolyte, which acts as a separator and allows (in the ideal case) selective migration of ions, *e.g.* H<sup>+</sup> or O<sup>2-</sup>, depending on the nature of the electrolyte. These ions migrate across the electrolyte, sustaining the reactions occurring at the cathode and anode. An electronic current via the external circuit, producing electrical energy by means of an external load, balances the ionic current through the electrolyte. The electrons arriving at the cathode participate in the reduction reaction, *e.g.*, O<sub>2</sub> + 4e<sup>-</sup> + 4H<sup>+</sup> → 2H<sub>2</sub>O or O<sub>2</sub> + 4e<sup>-</sup> → 2O<sup>2-</sup> in case the ion-conducting electrolyte conducts H<sup>+</sup> or O<sup>2-</sup>, respectively.

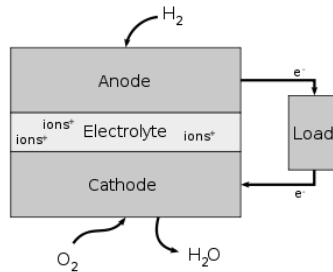


**Figure 1.5** Schematic representation of a fuel cell comprising an electrolyte, an anode and a cathode. Figure taken from Ref. 1.

Fuel cells are classified according to the type of electrolyte employed. The five common types of fuel cells and their main characteristics are listed in Table 1.3. The low-temperature fuel cells, including the alkaline fuel cell (AFC), polymer electrolyte membrane fuel cell (PEMFC) and the phosphoric acid fuel cell (PAFC), require relatively pure hydrogen to be supplied at the anode (to avoid potential poisoning of the precious metal electrocatalyst by CO, SO<sub>2</sub> or H<sub>2</sub>S). The molten-carbonate fuel cell (MCFC) and solid oxide fuel cell (SOFC), operating at temperatures above 500 °C, have the advantage that both hydrogen and carbon monoxide can be oxidized directly at the anode, or indirectly through internal reforming of methane [35]. Given the high operation temperatures of the MCFC and SOFC, their applicability is more to be found in stationary power generation. The low-temperature fuel cells are more suitable for portable power applications, due to obvious reasons like rapid start-up, minimization of stresses due to thermal cycling, etc. The PEMFC, exploiting hydrated polymer electrolytes (such as Nafion<sup>®</sup>), however, demand delicate water management. Current efforts are aimed at developing anhydrous proton conducting membranes for PEMFC's that can be operated at slightly elevated temperatures (above 100 °C).

**Table 1.3** Types of fuel cells according to the electrolyte employed and their main characteristics. Table adapted from data presented in Ref. 34.

	AFC	PEMFC	PAFC	MCFC	SOFC
Temperature (°C)	70	80	200	650	500-1000
Electrode	Metal or carbon	Pt-on-carbon	Pt-on-carbon	Ni + Cr	Ni/Y <sub>2</sub> O <sub>3</sub> -ZrO <sub>2</sub>
Electrolyte	KOH solution	Hydrated polymer membrane	H <sub>3</sub> PO <sub>4</sub> contained in porous matrix	LiCO <sub>3</sub> -K <sub>2</sub> CO <sub>3</sub> Molten salt contained in porous matrix	Y <sub>2</sub> O <sub>3</sub> doped ZrO <sub>2</sub>
Primary fuel	H <sub>2</sub>	H <sub>2</sub>	H <sub>2</sub>	H <sub>2</sub> / CO	H <sub>2</sub> /CO/CH <sub>4</sub>
Mobile ion	OH <sup>-</sup>	H <sup>+</sup>	H <sup>+</sup>	CO <sub>3</sub> <sup>2-</sup>	O <sup>2-</sup>
Efficiency	60%	60%	55%	47%	60-70 %

## 1.5 Scope of this thesis

The focus of thesis is on the development and characterization of selected solid acids and composites for possible use as electrolyte in a fuel cell. In Chapter II, the preparation and characterization of a new family of solid acids, derived from the polyprotic acid H<sub>2</sub>(PO<sub>3</sub>H), are described. In Chapter III, the effect of dispersion of nanosized SiO<sub>2</sub> particles in KH(PO<sub>3</sub>H) on its proton conductivity is investigated. The influences of SiO<sub>2</sub> mass fraction and particle size are both evaluated. In Chapter IV, the effect of isovalent substitution of NH<sub>4</sub><sup>+</sup> or Cs<sup>+</sup> for K<sup>+</sup> on the proton conductivity of KH(PO<sub>3</sub>H) is investigated. The effect of humidification on the electrochemical performance of



## *Chapter I*

---

Pt/KH(PO<sub>3</sub>H) electrodes is investigated in Chapter V. Chapter VI provides a general outlook and recommendations for further research. Finally, in the appendix of this PhD thesis, a micro emulsion-based synthesis is described for the preparation of nanoparticles of the solid acid CsHSO<sub>4</sub>.

## **References**

1. F. Barbir, PEM fuel cells : theory and practice, Elsevier Academic Press, Amsterdam ; Boston (2005).
2. P. Colomban, Proton conductors: solids, membranes and gels: materials and devices, Cambridge University Press, Cambridge (1992).
3. K.D. Kreuer, Annu. Rev. Mater. Res. 33 (2003) 333.
4. H. Iwahara, Solid State Ionics 86-8 (1996) 9.
5. J.W. Phair, S.P.S. Badwal, Ionics 12 (2006) 103.
6. L. Malavasi, C.A.J. Fisher, M.S. Islam, Chem. Soc. Rev. 39 (2010) 4370.
7. K.A. Mauritz, R.B. Moore, Chem. Rev. 104 (2004) 4535.
8. K. Schmidt-Rohr, Q. Chen, Nat. Mater. 7 (2008) 75.
9. P. Donoso, W. Gorecki, C. Berthier, F. Defendini, C. Poinsignon, M.B. Armand, Solid State Ionics 28-30 (1988) 969.
10. J. Qiao, N. Yoshimoto, M. Morita, J. Power Sources 105 (2002) 45.
11. E.F. Silva, R.P. Pereira, A.M. Rocco, Eur. Polym. J. 45 (2009) 3127.
12. J. Przyluski, W. Wieczorek, Synth. Met. 45 (1991) 323.
13. R.H. He, Q.F. Li, G. Xiao, N.J. Bjerrum, J. Membr. Sci. 226 (2003) 169.
14. K. D. Kreuer, S. J. Paddison, E. Spohr, and M. Schuster, Chem. Rev. 104, (2004) 4637.
15. Q.F. Li, J.O. Jensen, R.F. Savinell, N.J. Bjerrum, Prog. Polym. Sci. 34 (2009) 449.
16. T.J. Schmidt, J. Baurmeister, J. Power Sources 176 (2008) 428.
17. T. Norby, Nature 410 (2001) 877.
18. H. Matsumoto, In: T. Ishihara, Editor, Perovskite Oxide for Solid Oxide Fuel Cells, Springer US (2009), p.243-259.
19. T. Norby, In: T. Ishihara, Editor, Perovskite Oxide for Solid Oxide Fuel Cells, Springer US (2009), p.217-241.

20. A.L. Samgin, *Russ. J. Inorg. Chem.* 36 (2000) 816.
21. D.A. Boysen, *Superprotonic Solid Acids: Structure, Properties, and Applications*, California Institute of Technology, Ph.D., (2004).
22. P. Schuster, G. Zundel, C. Sandorfy, *The Hydrogen bond : recent developments in theory and experiments*, North-Holland Pub. Co. , Amsterdam (1976).
23. C.D. Zangmeister, J.E. Pemberton, *J. Solid State Chem.* 180 (2007) 1826.
24. E. Ortiz, R.A. Vargas, B.E. Mellander, *J. Phys. Condens. Matter* 18 (2006) 9561.
25. C.R.I. Chisholm, S.M. Haile, *Acta Crystallogr. B* 55 (1999) 937.
26. C.R.I. Chisholm, S.M. Haile, *Solid State Ionics* 136 (2000) 229.
27. S.M. Haile, G. Lentz, K.-D. Kreuer, J. Maier, *Solid State Ionics* 77 (1995) 128.
28. K. Itoh, T. Ukeda, T. Ozaki, E. Nakamura, *Acta Crystallogr. C* 46 (1990) 358.
29. S.M. Haile, D.A. Boysen, C.R.I. Chisholm, R.B. Merle, *Nature* 410 (2001) 910.
30. D.A. Boysen, S.M. Haile, H.J. Liu, R.A. Secco, *Chem. Mater.* 15 (2003) 727.
31. D.A. Boysen, T. Uda, C.R.I. Chisholm, S.M. Haile, *Science* 303 (2004) 68.
32. R.B. Merle, C.R.I. Chisholm, D.A. Boysen, S.M. Haile, *Energ. Fuel* 17 (2003) 210.
33. T. Uda, D.A. Boysen, S.M. Haile, *Solid State Ionics* 176 (2005) 127.
34. B.C.H. Steele, A. Heinzl, *Nature* 414 (2001) 345.
35. F. Alcaide, P.L. Cabot, E. Brillas, *J. Power Sources* 153 (2006) 47.

## 2 Superprotonic phase transitions in solid acid phosphites $MH(PO_3H)$ ( $M = Li^+, Na^+, K^+, Rb^+, Cs^+, NH_4^+$ )

### **Abstract**

*The ionic conductivity and thermal stability of solid acid phosphites  $MH(PO_3H)$  with  $M = Li^+, Na^+, K^+, Rb^+, Cs^+, NH_4^+$  have been investigated. Superprotonic conductivity following a polymorphic phase transition in the temperature range of 120 to 190 °C is observed for the monoclinic forms with  $M = Na^+, K^+, Rb^+, Cs^+$  and  $NH_4^+$ ; no superprotonic phase transition is observed for orthorhombic  $LiH(PO_3H)$ . At temperatures slightly beyond their superprotonic phase transition temperature, abrupt declines in the morphological stability and proton conductivity due to dehydration and/or melting are apparent in the  $Na^+, Rb^+$ , and  $NH_4^+$  containing acid salts. Under the experimental conditions maintained throughout this study,  $KH(PO_3H)$  and  $CsH(PO_3H)$  show good stability. Their superprotonic conductivities are  $4.2 \cdot 10^{-3} S cm^{-1}$  (at 140 °C) and  $3 \cdot 10^{-3} S cm^{-1}$  (at 160 °C), respectively, which values are comparable to that of widely investigated  $CsHSO_4$ . Rather than  $CsHSO_4$ ,  $KH(PO_3H)$  is demonstrated to show good stability in both oxidizing and reducing atmospheres, referring to conditions of relevance to its potential application as an electrolyte in fuel cells.*

## 2.1 Introduction

The superprotonic properties of solid acids compounds like  $\text{CsHSO}_4$  and  $\text{CsH}_2\text{PO}_4$  have attracted considerable attention due to their possible application as electrolyte in fuel cells operating at medium temperatures (100 - 300 °C) [1-5]. The superprotonic state relates to a phase transition to a disordered state at which the proton conductivity increases by several orders of magnitude, reaching values up to  $10^{-3}$  and  $10^{-2}$   $\text{S cm}^{-1}$  [1-7]. The uniqueness of the solid acids is that, in contrast with proton conducting polymeric electrolytes, the protons themselves are the mobile species, *i.e.*, no water molecules are required to enable transport, eliminating the problem of humidification of the electrolyte.

The onset of superprotonic behavior in the solid acid compounds, typically containing symmetrical tetrahedral oxy-anions  $\text{XO}_4$  ( $\text{X} = \text{S}, \text{Se}, \text{P}$ ), occurs upon dynamic disordering of the hydrogen-bond network in response to the phase change to a structure with higher crystallographic symmetry. The transport of protons is facilitated by rapid reorientations of the tetrahedra in combination with a high rate of proton transfer between adjacent tetrahedra in the disordered structure (Grotthuss mechanism) [4-7]. Generally, it is assumed that monoclinic solid acid structures containing large cations such as  $\text{Cs}^+$  and  $\text{Rb}^+$  are candidates to exhibit superprotonic behavior at elevated temperature [4, 5]. Among solid acids containing smaller cations, *e.g.*,  $\text{K}^+$  or  $\text{Na}^+$ , only potassium hydrogen sulphate,  $\text{K}_3\text{H}(\text{SO}_4)_2$ , has been found to exhibit superprotonic properties [8, 9].

Solid acid compounds with asymmetric oxy-anions may also give rise to superprotonic phase formation. Chisholm *et al.* [10] showed cesium dihydrogen phosphite,  $\text{CsH}(\text{PO}_3\text{H})$ , to exhibit superprotonic behavior above the monoclinic-to-cubic phase transition observed in this material, reaching a proton conductivity of  $4.6 \cdot 10^{-3}$   $\text{S cm}^{-1}$  at 150 °C. Cesium hydrogen sulfate,  $\text{CsHSO}_4$ , is by far the most extensively studied among the superprotonic solid acids, but

turns out not to be stable in hydrogen atmospheres [3, 11], limiting its potential use in fuel cells. The known stability of phosphites under hydrogen atmosphere inspired us to investigate the  $\text{MH}(\text{PO}_3\text{H})$  family of solid acids. This chapter presents results of conductivity measurements and thermal analysis on  $\text{MH}(\text{PO}_3\text{H})$  phosphites, where M is  $\text{Li}^+$ ,  $\text{Na}^+$ ,  $\text{K}^+$ ,  $\text{Rb}^+$ ,  $\text{Cs}^+$  or  $\text{NH}_4^+$ .

## **2.2 Experimental**

Powders of  $\text{MH}(\text{PO}_3\text{H})$  were prepared by slow evaporation of aqueous solutions of carbonates (or hydroxides) of the corresponding metals in phosphorous acid (99%, Aldrich) in mole ratio  $\text{M}:\text{H}_3\text{PO}_3$  of 1:1. All powders were dried in an oven in air at  $\sim 105^\circ\text{C}$  during 20 h prior to experiments. Chemicals used for powder syntheses included potassium hydroxide (Merck, 99.5%), sodium hydroxide (Merck, 99.5%), lithium carbonate (Sigma-Aldrich, 99%), rubidium carbonate (Alfa Aesar, 99.8%), caesium carbonate (Aldrich, 99.9%), and ammonium hydrogen carbonate (Alfa Aesar).

X-ray powder diffraction data were recorded at room temperature using a Philips XRD PW3020 (50kV, 35 mA,  $\text{Cu K}\alpha_1$ ). Data were analyzed using the Philips X'Pert program for phase identification. Thermal analysis was performed to detect and characterize the presence of phase transitions in the  $\text{MH}(\text{PO}_3\text{H})$  phosphites as well as to establish their dehydration/decomposition and melting behaviour. Thermogravimetry (TG) and differential thermal analysis (DTA) were carried out under flowing, dry nitrogen ( $45\text{ ml min}^{-1}$ ) using a TG-DTA system (Setaram SETSYS 16/18) at a scan rate of  $3\text{ K min}^{-1}$ . Samples were finely ground in an agate mortar before measurements.  $\text{KH}(\text{PO}_3\text{H})$  was further investigated by testing its stability under oxidizing and reducing atmospheres. To this end, TG-DTA measurements were conducted on powders of  $\text{KH}(\text{PO}_3\text{H})$ , either pure or mixed with Pt/C catalyst (Pt, 50% on carbon black,

Alfa Aesar), under dry hydrogen ( $p_{\text{H}_2} \approx 0.05$  atm) and humidified air ( $p_{\text{H}_2\text{O}} \approx 0.02$  atm). Humidification of the air was accomplished by passing the gas through a water bubbler held at 21 °C.

Conductivity measurements were carried out using electrochemical impedance spectroscopy. Powders of the phosphites were isostatically pressed into discs of 1 mm thickness and 10 mm diameter at 4000 bar. The relative density was about 90%. Platinum electrodes were sputtered on both sides of a disc. Impedance spectra were recorded using a PGstat20 Autolab Potentiostat (ECO-Chemie) with integrated frequency response analyzer under flowing (45 ml min<sup>-1</sup>), dry nitrogen. An excitation voltage with amplitude 10 mV was used to ensure that measurements were performed in the linear regime. No bias voltage was applied. The temperature was incremented stepwise, with a heating/cooling rate of 0.8 K min<sup>-1</sup>, at which the sample was equilibrated for at least 30 min. Impedance spectra were recorded over the frequency range 0.5 MHz to 100 Hz below, and from 50 kHz to 100 or 10 Hz above the superprotonic phase transition temperature, and approved only after passing a Kramer-Kronig transformation test [12, 13]. Data analysis was carried out using complex nonlinear least squares fitting routines [14, 15].

## 2.3 Results and discussion

### 2.3.1 Phase analysis

Room temperature XRD patterns of the MH(PO<sub>3</sub>H) phosphites are shown in Figure 2.1. In accordance with prior results from literature [16-18], the patterns obtained for M = K<sup>+</sup>, Rb<sup>+</sup>, Cs and NH<sub>4</sub><sup>+</sup> could be indexed on the basis of a monoclinic unit cell, whilst that for Li<sup>+</sup> could be indexed on a orthorhombic unit cell. The XRD pattern for NaH(PO<sub>3</sub>H) showed the co-existence of monoclinic

and orthorhombic phases. No attempt was undertaken to investigate this any further. Similar to the low temperature phase of superprotonic sulphates and phosphates, containing symmetrical tetrahedral oxyanions, the  $\text{PO}_3\text{H}$  tetrahedra in the ordered monoclinic phosphites form infinite chains via hydrogen bonds (see Figure 2.2). In all cases, XRD diffraction patterns showed no evidence of impurity phases.

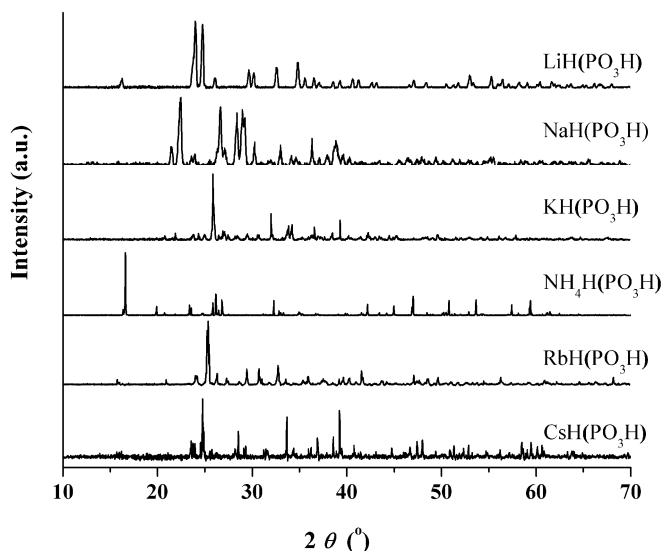
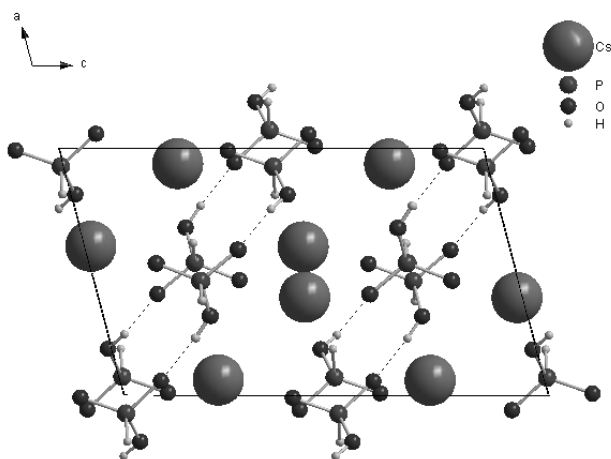


**Figure 2.1** X-ray powder diffraction patterns of the room temperature polymorphs of  $\text{MH}(\text{PO}_3\text{H})$  phosphites.

Thermal analysis in dry nitrogen was performed to detect the superprotonic phase transition and to monitor weight losses due to dehydration/decomposition events. DTA data shown in Figure 2.3a in conjunction with data from conductivity measurements (See Section 2.3.2) reveal that superprotonic phase transitions are only apparent in the phosphites adopting a monoclinic crystal structure at room temperature. No superprotonic phase transition is observed for orthorhombic  $\text{LiH}(\text{PO}_3\text{H})$ . Superprotonic phase transition temperatures for

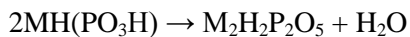


MH(PO<sub>3</sub>H) with M = Na<sup>+</sup>, K<sup>+</sup>, Rb<sup>+</sup>, Cs<sup>+</sup> and NH<sub>4</sub><sup>+</sup> are found in the range 120–190 °C; no obvious relationship emerges between the onset temperature of the superprotonic phase transition and the radius [19] of the involved cation as can be judged from Figure 2.4. The superprotonic transition temperature for CsH(PO<sub>3</sub>H) is found to be in good agreement with the value of 137 °C reported by Chisholm *et al.* [10]. In the case of RbH(PO<sub>3</sub>H), the peak associated with the superprotonic phase transition partially overlaps the peak attributed to melting.



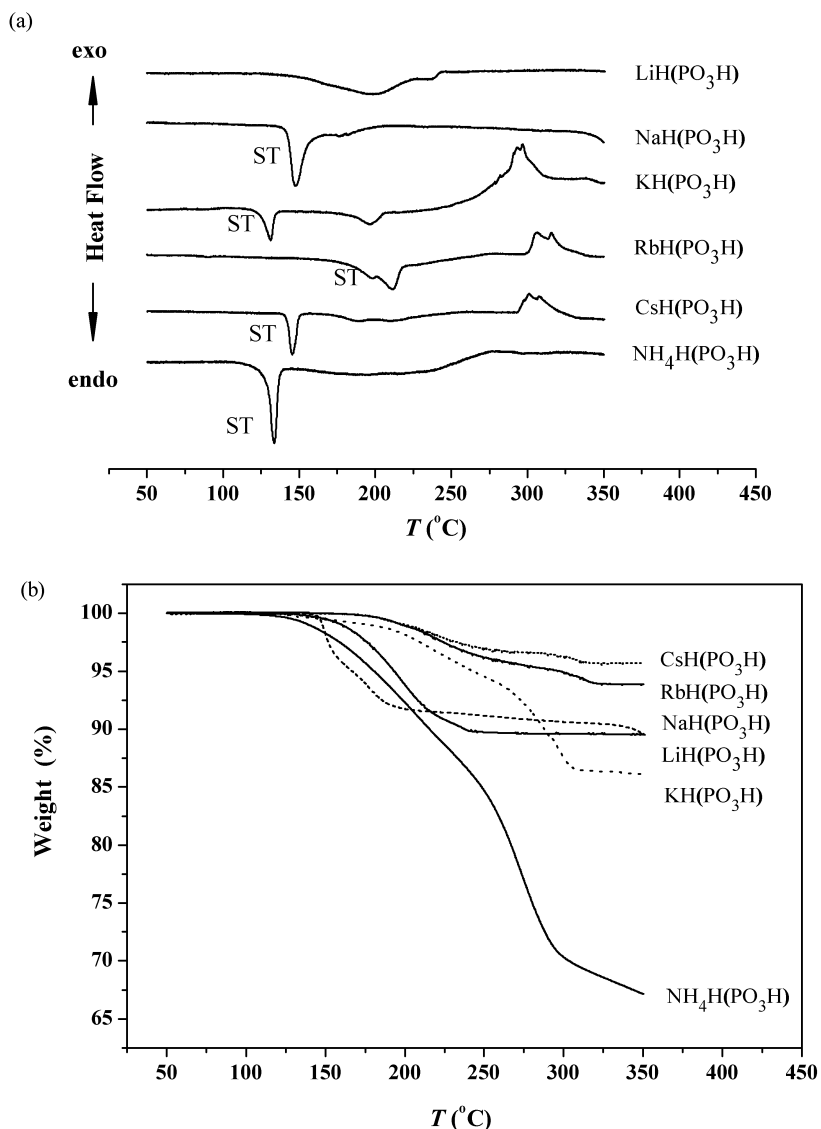
**Figure 2.2** Monoclinic crystal structure of CsH(PO<sub>3</sub>H) drawn using atom coordinates listed in Ref. 16.

Figure 2.3b shows that thermal decomposition of MH(PO<sub>3</sub>H) begins just above the superprotonic phase transition. The gradual weight loss observed for each of the phosphites extends over a wide temperature range. While being relatively small for Cs<sup>+</sup> and Rb<sup>+</sup> acid salts, it is much more pronounced for the K<sup>+</sup> and NH<sub>4</sub><sup>+</sup> containing acid salts. The weight loss plateaus for CsH(PO<sub>3</sub>H), RbH(PO<sub>3</sub>H) and LiH(PO<sub>3</sub>H) observed at the highest temperature covered by experiment are found to be in good agreement with the following dimerization reaction,



3.1

In the case of  $\text{KH}(\text{PO}_3\text{H})$  and  $\text{NH}_4\text{H}(\text{PO}_3\text{H})$  it is assumed that dimerization is



**Figure 2.3.** Thermal analysis of phosphites  $\text{MH}(\text{PO}_3\text{H})$ . Data from (a) DTA and (b) TG measurements carried out under nitrogen. Superprotonic transitions are labelled with ST.

just an intermediate step in the entire dehydration process. The constant weight plateau observed for  $\text{KH}(\text{PO}_3\text{H})$  at high temperature, above  $\sim 310^\circ\text{C}$ , would correspond with the formation of metaphosphite  $\text{KPO}_2$ .

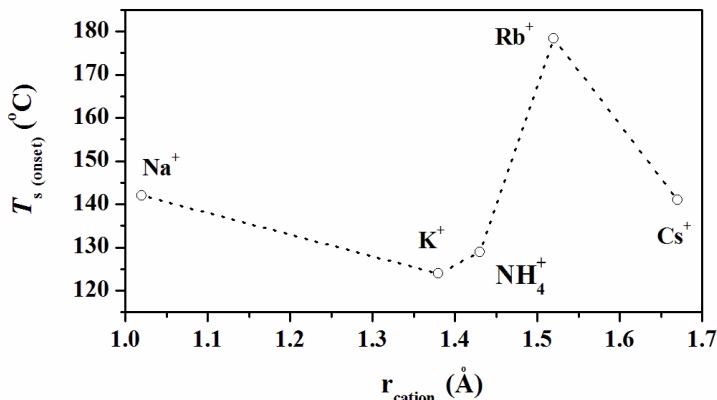


**Figure 2.4** Dependence of the extrapolated onset temperature of the superprotonic phase transition ( $T_s$ ) for phases  $\text{MH}(\text{PO}_3\text{H})$  on the alkali metal cation radius. Cation

Figure 2.5 compares data obtained thermal analysis of  $\text{KH}(\text{PO}_3\text{H})$  under dry nitrogen with those from measurements under hydrogen ( $p_{\text{H}_2} = 0.05 \text{ atm}$ ) and humidified air ( $p_{\text{H}_2\text{O}} \approx 0.02 \text{ atm}$ ).<sup>1</sup> In each of the atmospheres, the superprotonic phase transition with an onset temperature of  $125^\circ\text{C}$  is well-resolved from other thermal events, and is accompanied by a small weight loss ( $< 1 \text{ wt}\%$ ). A gradual weight loss due to partial dehydration is observed upon further heating, which is independent on whether the atmosphere is reducing or oxidizing. Similar behavior was found when  $\text{KH}(\text{PO}_3\text{H})$  powder was mixed with a Pt catalyst, noting that reaction rates might be small in the absence of a catalyst [11]. Further note that the weight losses in each of the test atmospheres

<sup>1</sup> The effect of humidification on the long-term conductivity of  $\text{KH}(\text{PO}_3\text{H})$  is discussed in Chapter 3 of this thesis. It is demonstrated that dehydration in air at  $140^\circ\text{C}$  can be suppressed by humidification of the air stream to  $p_{\text{H}_2\text{O}} \approx 0.02 \text{ atm}$ .

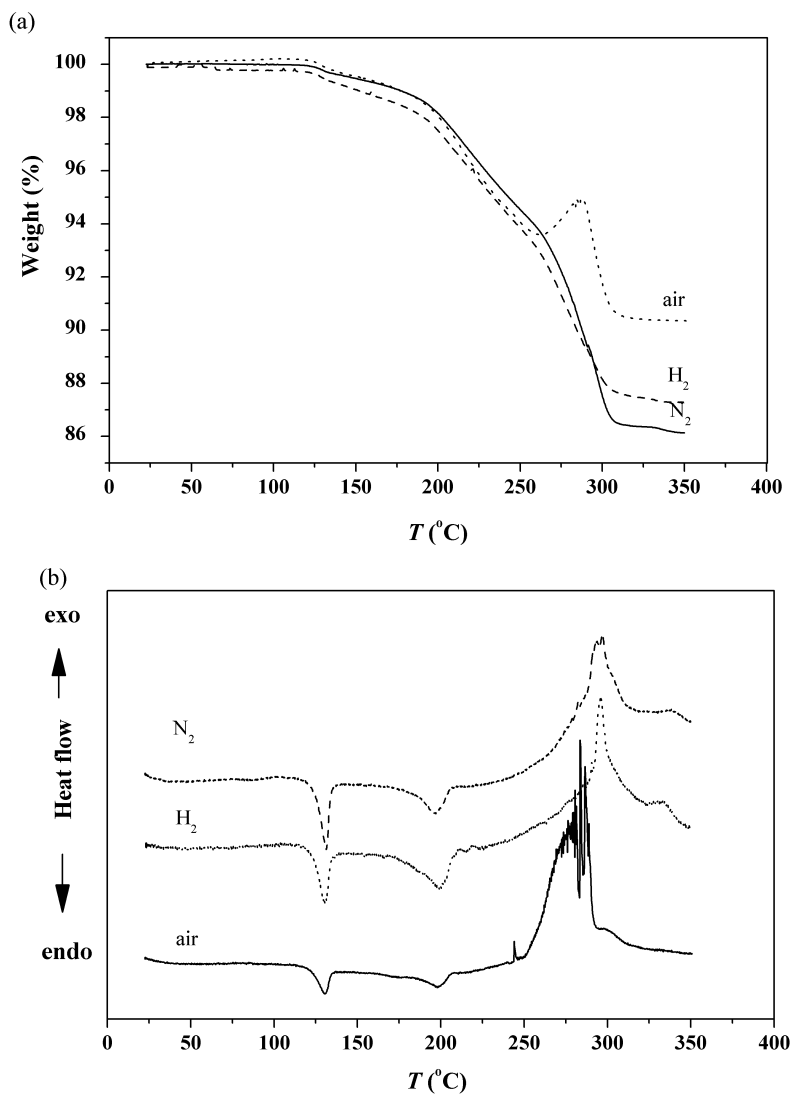


**Figure 2.5** Thermal analysis of KH(PO<sub>3</sub>H) powder under different atmospheres. Data from (a) thermogravimetric and (b) differential thermal analysis under dry nitrogen, a mixture of N<sub>2</sub> and H<sub>2</sub> ( $p_{\text{H}_2} = 0.05$  atm), and humidified air ( $p_{\text{H}_2\text{O}} \approx 0.02$  atm).

become more pronounced after endothermic melting at 195 °C. Finally it is noted that oxidation of  $\text{KH}(\text{PO}_3\text{H})$  in air starts at an onset temperature around 250 °C, which is far higher than the melting temperature, and far beyond the temperature range where  $\text{KH}(\text{PO}_3\text{H})$  might be used as electrolyte.

### 2.3.2 Impedance measurements

Typical impedance spectra obtained at temperatures before and after the superprotonic phase transition are given in Figure 2.6 a and b, respectively. Due to the change in relative contributions of bulk electrolyte and interface to the total impedance, the spectra change remarkably below and above the superprotonic transition temperature. Good agreement is observed between the experimental and calculated data using the equivalent circuits shown in Figure 2.6c and d, respectively, where CPE represents a constant phase element, C a capacitance, and  $R_E$  the electrolyte resistance. Subscripts *E* and *I* designate the electrolyte and Pt | electrolyte interface, respectively.  $C_p$  is attributed to a parasitic capacitance. The relative deviations between the experimental and calculated spectra are less than 2%. No effort was made in this work to obtain a detailed understanding of the interfacial contributions to the impedance spectra.

Arrhenius plots of the proton conductivity of the  $\text{MH}(\text{PO}_3\text{H})$  phosphites on temperature extracted from data of impedance measurements are presented in Figure 2.7. The conductivity of the monoclinic phases is found to increase profoundly at the superprotonic phase transition temperature, which coincides with the onset of the corresponding peaks (labeled with *ST*) observed by DTA (see Figure 2.3a).

The present data gives clear evidence that similar to  $\text{CsH}(\text{PO}_3\text{H})$  all the monoclinic phases of  $\text{MH}(\text{PO}_3\text{H})$  with  $\text{M} = \text{Na}^+, \text{K}^+, \text{Rb}^+, \text{Cs}^+, \text{and } \text{NH}_4^+$  exhibit superprotonic behavior at high temperature. However, only  $\text{KH}(\text{PO}_3\text{H})$  and  $\text{CsH}(\text{PO}_3\text{H})$  showed fair stability towards active dehydration beyond the

structural phase transformation. In contrast to the monoclinic dihydrogen phosphites, orthorhombic  $\text{LiH}(\text{PO}_3\text{H})$  does not exhibit superprotonic behavior and its conductivity remains below  $10^{-8} \text{ S cm}^{-1}$  at all temperatures before thermal decomposition.

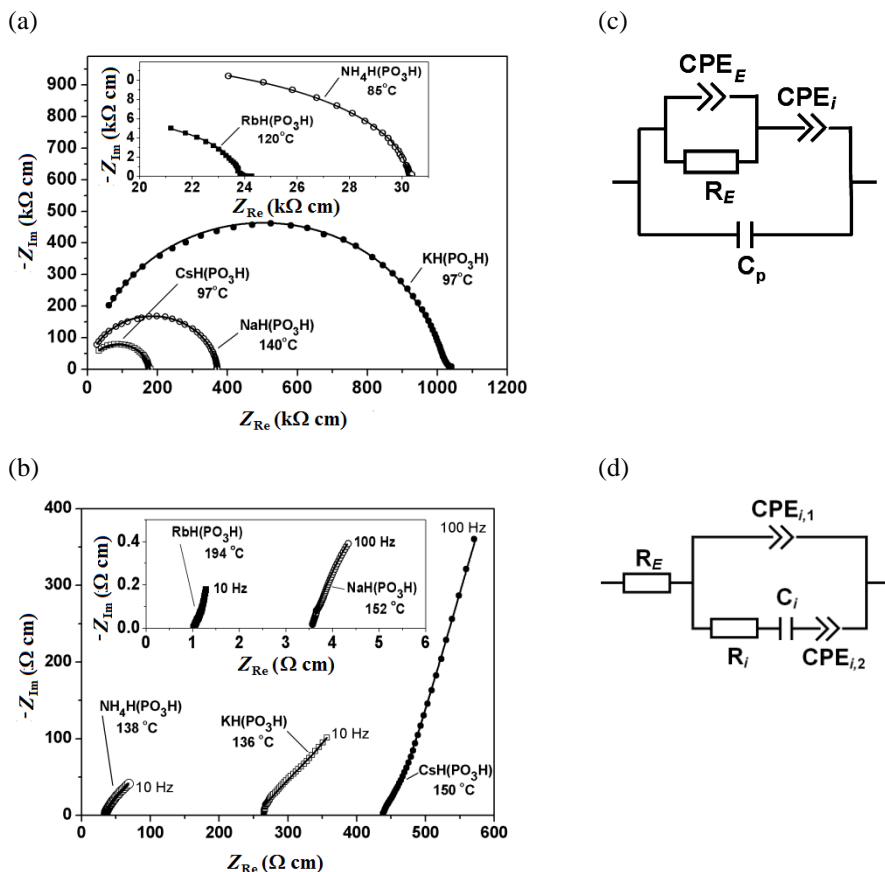


**Figure 2.6** Impedance spectra obtained for polycrystalline samples of  $\text{MH}(\text{PO}_3\text{H})$ , where  $M = \text{Na}^+$ ,  $\text{K}^+$ ,  $\text{Rb}^+$ ,  $\text{Cs}^+$  and  $\text{NH}_4^+$ , measured (a) below and (b) above the superprotonic phase transition temperature. Measurements were conducted in flowing, dry nitrogen. Solid lines represent calculated data using the equivalent electric circuits shown in (c) and (d), respectively.

Under the conditions of the experiments, the  $\text{Na}^+$ ,  $\text{Rb}^+$ , and  $\text{NH}_4^+$  containing acid salts were found to be subject to dehydration and/or melting just above the superprotonic phase transition. In these cases a serious loss in the morphological stability of the materials and abrupt declines in the proton conductivity were observed. Similar dehydration events were observed in  $\text{CsH}_2\text{PO}_4$  upon heating in a dry nitrogen atmosphere above the superprotonic transition temperature [6].

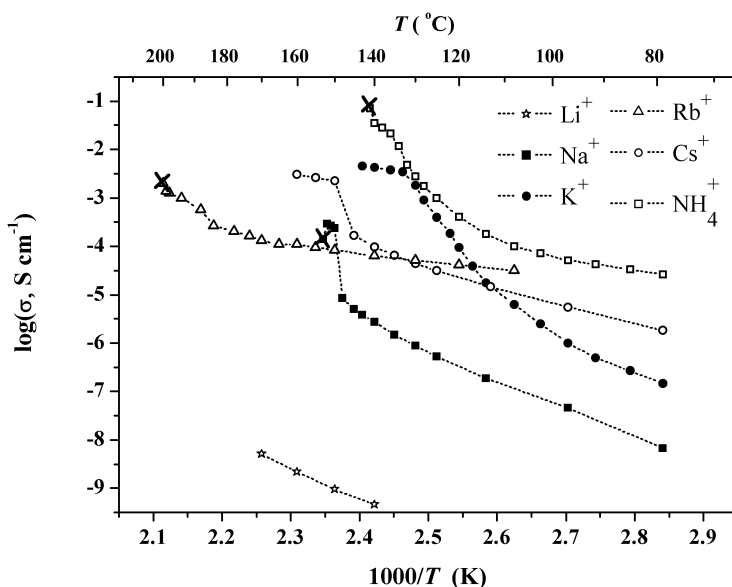


**Figure 2.7** Arrhenius plot of the proton conductivity of polycrystalline  $\text{MH}(\text{PO}_3\text{H})$ . The onset of significant loss in the conductivity due to thermal decomposition is marked with a cross. Measurements were conducted in a dry  $\text{N}_2$  atmosphere.

Figure 2.8 shows the proton conductivity of the two most stable compounds in this study,  $\text{KH}(\text{PO}_3\text{H})$  and  $\text{CsH}(\text{PO}_3\text{H})$ , upon thermal cycling. It is readily apparent from this figure that the superprotonic phase transition in both compounds exhibit significant hysteresis. Upon heating for the first time the

conductivity of  $\text{KH}(\text{PO}_3\text{H})$  increases from  $1.4 \cdot 10^{-7} \text{ S cm}^{-1}$  at  $80^\circ\text{C}$  to  $4.2 \cdot 10^{-3} \text{ S cm}^{-1}$  at  $140^\circ\text{C}$  just above the superprotonic phase transition temperature, and

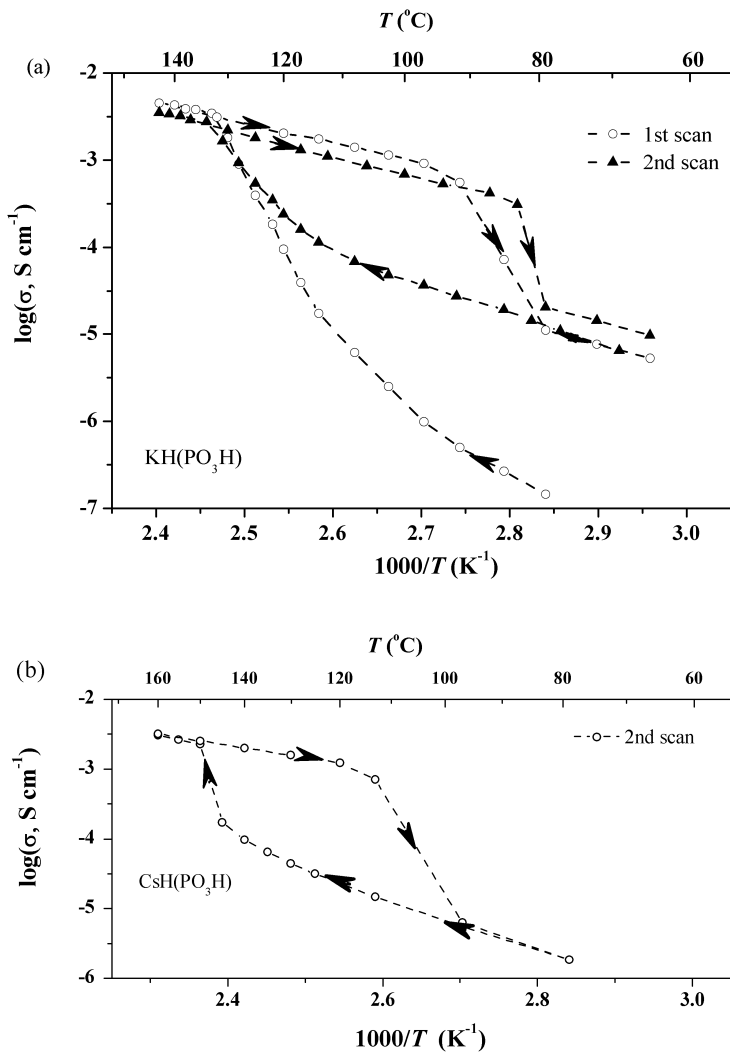


**Figure 2.8** Arrhenius plot of the conductivity of (a)  $\text{KH}(\text{PO}_3\text{H})$  and (b)  $\text{CsH}(\text{PO}_3\text{H})$ , showing the effect of thermal cycling. Measurements were performed in a dry nitrogen atmosphere. For  $\text{KH}(\text{PO}_3\text{H})$  the results of two thermal cycles are shown; for  $\text{CsH}(\text{PO}_3\text{H})$  only results for the second thermal cycle are shown.



sharply drops at an onset temperature of  $\sim 95$  °C to reach a value of  $5.2 \cdot 10^{-6}$  S cm<sup>-1</sup> at 65 °C. Upon the second thermal cycle, a small loss in the conductivity is apparent above the superprotonic transition temperature, which may be due to partial dehydration. A hysteresis in the conductivity is also found for CsH(PO<sub>3</sub>H), as shown in Figure 2.8b. The superprotonic conductivity observed for this material is found to be slightly smaller than the value of  $3 \cdot 10^{-3}$  S cm<sup>-1</sup> in dry argon at 160 °C reported for CsH(PO<sub>3</sub>H) by Chisholm *et al.* [10]. This may be attributed to possible differences in the thermal history of the samples.

## 2.4 Conclusions

Superprotonic conductivity has been confirmed to occur in the monoclinic phosphites MH(PO<sub>3</sub>H) where M = Na<sup>+</sup>, K<sup>+</sup>, Rb<sup>+</sup>, Cs<sup>+</sup>, and NH<sub>4</sub><sup>+</sup> following a polymorphic phase transition in the temperature range of 120 to 190 °C. No superprotonic phase transition is observed for orthorhombic LiH(PO<sub>3</sub>H). While the proton conductivity of Na<sup>+</sup>, Rb<sup>+</sup>, and NH<sub>4</sub><sup>+</sup> containing phosphites above the superprotonic transition temperature severely deteriorates in dry nitrogen due to dehydration and/or melting, a stable proton conductivity is observed for KH(PO<sub>3</sub>H) and CsH(PO<sub>3</sub>H) at the conditions maintained throughout this study. The measured proton conductivity for these materials reaches values of  $4.2 \cdot 10^{-3}$  S cm<sup>-1</sup> (at 140 °C) and  $3 \cdot 10^{-3}$  S cm<sup>-1</sup> (160 °C), respectively, which are comparable to values reported for CsHSO<sub>4</sub>, which is known to exhibit a superprotonic phase transition at 141 °C [1, 3, 7, 20]. Unlike sulphate and selenate solid acid electrolytes, KH(PO<sub>3</sub>H) and CsH(PO<sub>3</sub>H) can be operated in both oxidizing and reducing atmospheres. Strong hygroscopic properties of CsH(PO<sub>3</sub>H) experienced in this study may, however, restrict its use. Further investigations are required to test the possible use of KH(PO<sub>3</sub>H) and CsH(PO<sub>3</sub>H) as electrolytes in fuel cells.

## References

1. E. Ortiz, R.A. Vargas, B.E. Mellander, *J. Phys. Condens. Mat.* 18 (2006) 9561.
2. S.M. Haile, C.R.I. Chisholm, K. Sasaki, D.A. Boysen, T. Uda, *Faraday Discuss.* 134 (2007) 17.
3. T. Uda, D.A. Boysen, S.M. Haile, *Solid State Ionics* 176 (2005) (1-2), p. 127.
4. S.M. Haile, D.A. Boysen, C.R.I. Chisholm, R.B. Merle, *Nature* 410 (2001) 910.
5. A.I. Baranov, V.V. Grebenev, A.N. Khodan, V.V. Dolbinina, E.P. Efremova, *Solid State Ionics* 176 (2005) 2871.
6. J. Otomo, N. Minagawa, C.J. Wen, K. Eguchi, H. Takahashi, *Solid State Ionics* 156 (2003) 357.
7. C.R.I. Chisholm, Y.H. Jang, S.M. Haile, W.A. Goddard, *Phys. Rev. B* 72 (2005) 134103.
8. C.R.I. Chisholm, S.M. Haile, *Solid State Ionics* 145 (2001) 179.
9. C.R.I. Chisholm, L.A. Cowan, S.M. Haile, *Chem. Mater.* 13 (2001) 2909.
10. C.R.I. Chisholm, R.B. Merle, D.A. Boysen S.M. Haile, *Chem. Mater.* 14 (2002) 3889.
11. R.B. Merle, C.R.I. Chisholm, D.A. Boysen, S.M. Haile, *Energy & Fuels* 17 (2003) 210.
12. B.A. Boukamp, *J. Electrochem. Soc.* 142 (1995) 1885.
13. B.A. Boukamp, *Solid State Ionics* 169 (2004) 65.
14. B.A. Boukamp, *Solid State Ionics* 18-9 (1986) 136.
15. B.A. Boukamp, *Solid State Ionics* 20 (1986) 31.
16. B. Kratochvil, J. Podlahova, J. Hasek, *Acta Crystallogr., Sect. C: Cryst. Struct. Commun.* 39 (1983) 326.

17. E.V. Kosterina, S.I. Troyanov, E. Kemnitz, L.A. Aslanov, *Russ. J. Coord. Chem.* 27 (2001) 458.
18. A.W. Frazier K.R. Waerstad, *Fert. Res.* 32 (1992) 161.
19. R.D. Shannon, *Acta Crystallogr., Sect. A: Found. Crystallogr.* 32 (1976) 751.
20. V.G. Ponomareva G.V. Lavrova, *Solid State Ionics* 145 (2001)197.

## 3 Proton conductivity of composite electrolytes $\text{KH}(\text{PO}_3\text{H})\text{-SiO}_2$

### *Abstract*

*The influence of dispersion of nano particulate  $\text{SiO}_2$  in the solid acid  $\text{KH}(\text{PO}_3\text{H})$  on superprotonic behavior has been investigated by X-ray powder diffraction, thermal analysis and impedance spectroscopy. Both mass fraction and particle size of the  $\text{SiO}_2$  dispersoids in the composite electrolytes are varied. Dispersion of  $\text{SiO}_2$  in the solid acid matrix is found to lower proton conductivity of the composites in their superprotonic forms. Simultaneously, the superprotonic phase transition temperature is reduced and the conductivity jump at the superprotonic phase transition is smoothed due to significant enhancement of the low-temperature proton conductivity. At  $\text{SiO}_2$  mass fraction  $\omega = 0.5$  (with particle size  $d_p \approx 14$  nm) in the composite, the protonic conductivity above the superprotonic phase transition, at  $140^\circ\text{C}$ , has dropped almost one order of magnitude relative to parent  $\text{KH}(\text{PO}_3\text{H})$ , owing to a reduced volume and to blocking effects by insulating  $\text{SiO}_2$  nano particles, while the low-temperature conductivity is enhanced such that the characteristic conductivity rise at the superprotonic phase transition temperature is hardly noticeable. The enhancement of the low-temperature conductivity is attributed to the presence of fast conduction pathways along  $\text{KH}(\text{PO}_3\text{H})/\text{SiO}_2$  interfaces,*

*the concentration of which increases (as does the conductivity) with the degree of dispersion of SiO<sub>2</sub> nano particles and associated amorphization of the solid acid.*

*It is further demonstrated that dehydration and associated degradation of the proton conductivity, at 140 °C, can be prevented by a slight humidification of the gas streams, corresponding to a water partial pressure as low as ~ 0.02 atm. The proton conductivity of the composite electrolyte KH(PO<sub>3</sub>H)-SiO<sub>2</sub> ( $\omega = 0.2$ ;  $d_p \approx 14$  nm) measured under these conditions amounts to  $1.15 \cdot 10^{-3} \text{ S cm}^{-1}$ . Finally, it is shown that the dispersion-strengthened composite electrolyte can be easily made into a thin film in the  $\mu\text{m}$  range by dip-coating from a colloidal suspension.*

### **3.1 Introduction**

Inorganic solid acids like CsHSO<sub>4</sub> and CsH<sub>2</sub>PO<sub>4</sub>, exhibiting high proton conductivity, have potential for use as electrolyte in fuel cells [1-6]. The higher operating temperatures relative to polymer electrolytes, typically in the range 100 - 250 °C, contribute to improved electrode kinetics and CO tolerance of known electrode catalysts. Unlike hydrated sulphonated polymers such as Nafion<sup>®</sup>, no water molecules are required to facilitate proton transport in the solid acids, eliminating the need for continuous humidification of reactant gases. Haile and co-workers have shown the use of solid acid proton conductors both in H<sub>2</sub>/O<sub>2</sub> and direct methanol fuel cells [3, 4]. Using supported thin CsH<sub>2</sub>PO<sub>4</sub> electrolyte membranes on porous stainless steel gas-diffusion electrodes, peak power densities as high as 415 mW cm<sup>-2</sup> were obtained [3].

Proton conductivity in the solid acid compounds (*e.g.*, sulphates, selenates and phosphates) arises upon a polymorphic phase transition at elevated temperature. The transition, often referred to as superprotonic phase transition [5, 6], creates dynamical disorder in the H-bonded XO<sub>4</sub> network (where X= S, Se, P), enabling fast transport of protons mediated by rapid reorientations of the XO<sub>4</sub> tetrahedra and rapid transfer of protons between adjacent oxyanions (Grotthuss mechanism) [5, 7]. The proton conductivity at the superprotonic phase transition rises by 2-3 orders of magnitude and may reach values up to 10<sup>-3</sup> to 10<sup>-2</sup> S cm<sup>-1</sup> [5, 8, 9]. To date, however, implementation of superprotonic solid acids in fuel cells is hindered by a poor chemical and mechanical stability [1, 7]. The alkali-metal hydrogen sulphates and selenates decompose in hydrogen containing atmospheres [10, 11], whereas their dihydrogen phosphate counterparts need significant levels of humidification, up to a water vapour pressure of 0.30 atm. for CsH<sub>2</sub>PO<sub>4</sub> [1, 4, 12], to maintain their superprotonic properties. These facts prompted us in previous research to explore the proton

conducting properties of alkali-metal acid phosphites  $MH(PO_3H)$  ( $M = Li^+, Na^+, K^+, Rb^+, Cs^+, NH_4^+$ ) [13]. The superprotonic monoclinic-to-cubic phase transition in potassium dihydrogen phosphite,  $KH(PO_3H)$  was observed at an onset temperature of 132 °C, with the proton conductivity increasing to  $4.2 \cdot 10^{-3} \text{ S cm}^{-1}$  at 140 °C. This value is comparable to that of widely investigated  $CsHSO_4$ , showing a conductivity of  $4 \cdot 10^{-3} \text{ S cm}^{-1}$  at 160 °C [9]. Furthermore, it was demonstrated that  $KH(PO_3H)$  shows stability in both oxidizing and reducing environments [14].

Dispersion of fine oxide particles, *e.g.*,  $TiO_2$  or  $SiO_2$ , is known to be an effective way of improving the mechanical properties of solid acids [15, 16]. In this study, the proton conductivity and thermal stability of  $KH(PO_3H)-SiO_2$  composites obtained from evaporation of water from colloidal suspensions of  $SiO_2$  nano particles in aqueous solutions of  $KH(PO_3H)$  are investigated. Also initial results are reported on the preparation and characterisation of thin films of  $KH(PO_3H)-SiO_2$ .

### 3.2 Experimental

Powders of  $KH(PO_3H)$  were prepared by slow evaporation of aqueous solutions of potassium hydroxide (Fluka, ultra pure) in phosphorous acid (99%, Aldrich), in which the mole ratio  $K:H_3PO_3$  was fixed at 1:1. The powders were dried in an oven at ~105 °C during 20 h, ground in an agate mortar and stored in a desiccator, because of the hygroscopicity of the pure salt. Powders of  $KH(PO_3H)-SiO_2$  composites were prepared using a wet impregnation method. Silica powder with known particle size ( $d_p \approx 14\text{nm}$ , Aldrich;  $d_p \approx 80 \text{ nm}$ , Alfa-Aesar;  $d_p \approx 2\mu\text{m}$ , Riedel- de Haën), was colloiddally suspended in aqueous solutions of  $KH(PO_3H)$ , assisted by ultrasonic treatment to destroy agglomerates, to an amount that would yield various concentrations, containing

up to 50 wt% of SiO<sub>2</sub>. Water was removed by slow evaporation under rigorous stirring of the suspensions. The obtained samples were dried in an oven at 100 °C for one day, and subsequently grounded in an agate mortar to obtain fine powders, prior to further investigations. X-ray powder diffraction data were recorded using a Philips XRD PW3020 (50kV, 35 mA, Cu K $\alpha$ 1) diffractometer at room temperature, and processed with the Philips X'Pert program for phase identification. Differential thermal analysis (DTA) was carried out using a TG-DTA system (Setaram SETSYS 16/18) at a scan rate of 3 K min<sup>-1</sup> in flowing N<sub>2</sub> (40 ml min<sup>-1</sup>). Brunauer-Emmet-Teller (BET) surface area measurements of SiO<sub>2</sub> powders were made by nitrogen adsorption at 77 K (Micromeritics ASAP 2020M).

Powders of pure KH(PO<sub>3</sub>H) and composites KH(PO<sub>3</sub>H)-SiO<sub>2</sub> were uniaxially pressed at 4000 bar into discs of 0.5 mm thickness and 10 mm diameter. The relative density of the pressed specimens was about 90%. Thin composite KH(PO<sub>3</sub>H)-SiO<sub>2</sub> films on a Pt-coated silicon wafer were prepared by dip coating from an aqueous suspension at a concentration of 200 g L<sup>-1</sup> with a ratio KH(PO<sub>3</sub>H):SiO<sub>2</sub> = 4:1 by weight. The films were dried in an oven at 45 °C for 10h and then at 100 °C for ~24h. For conductivity measurements, platinum electrodes were sputtered using a JOEL JFC-1300 auto coating machine (deposition rate 20 nm min<sup>-1</sup>).

Conductivity measurements were performed using electrochemical impedance spectroscopy (EIS) using a PGstat20 Autolab Potentiostat (ECO-Chemie) with integrated frequency response analyzer. An excitation voltage with an amplitude of 10 mV was used to ensure that measurements were performed in the linear regime. No bias voltage was applied. The temperature was incremented stepwise, with a heating/cooling rate of 0.8 K min<sup>-1</sup>, at which the sample was equilibrated for at least 30 min prior to data acquisition. Measurements were performed under flowing dry nitrogen or humidified air



(45 ml min<sup>-1</sup>) at atmospheric pressure. Humidification of the air was performed by passing the gas through a water bubbler held at 21 °C. Impedance spectra were recorded over the frequency range 0.5 MHz to 100 Hz below and from 50 kHz to 10 Hz above the superprotonic phase transition temperature. Spectra were analyzed only after passing a Kramer-Kronig transformation test [17, 18]. Data analysis was carried out using complex nonlinear least squares fitting routines [19, 20].

### 3.3 Results and discussion

#### 3.3.1 X-Ray powder diffraction and thermal analysis

Figure 3.1 shows the room temperature diffraction patterns of KH(PO<sub>3</sub>H)-SiO<sub>2</sub> composites with different mass fractions of silica. All patterns can be ascribed to the low-temperature monoclinic phase potassium dihydrogen phosphite, KH(PO<sub>3</sub>H). No evidence is apparent of formation of new phases. With increasing SiO<sub>2</sub> content, broadening and loss of intensity of the peaks occur. This is attributed to a loss of crystallinity and/or possible amorphization of part of the KH(PO<sub>3</sub>H), increasing with SiO<sub>2</sub> content. During the evaporation of water from the aqueous colloidal suspension, SiO<sub>2</sub> nanoparticles serve as heterogeneous nucleation sites for the precipitation of KH(PO<sub>3</sub>H). Amorphization of KH(PO<sub>3</sub>H) may occur, depending on the degree of dispersion of silica particles, available surface area, and internal pore structure, considering possible infiltration of the solid acid in pores of SiO<sub>2</sub>, and preparation conditions. In fact, amorphization has been postulated or demonstrated in a number of studies where oxide additives are dispersed within superprotonic solid acids, including SiO<sub>2</sub>, and TiO<sub>2</sub> [21-24].

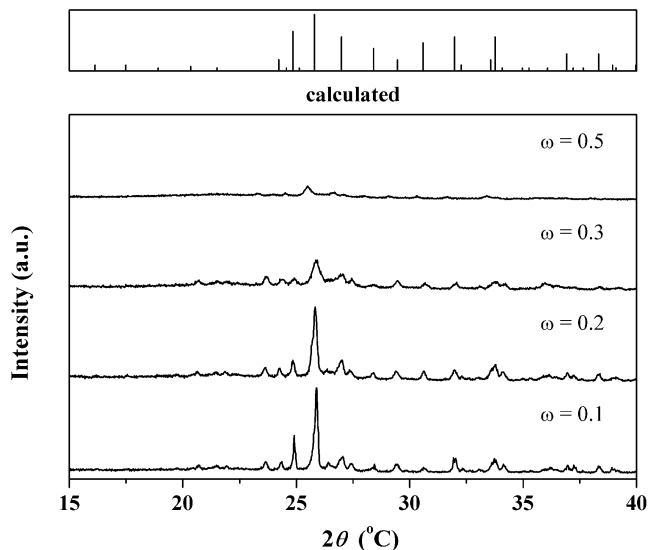


**Figure 3.1.** X-ray powder diffraction patterns of KH(PO<sub>3</sub>H)-SiO<sub>2</sub> composites with different mass fractions,  $\omega$ , of SiO<sub>2</sub> ( $d_p \approx 14$  nm). Also shown is the calculated diffraction pattern for the room temperature structure of KH(PO<sub>3</sub>H).

DTA curves of KH(PO<sub>3</sub>H)-SiO<sub>2</sub> composites with different mass fractions of silica with particle size  $\sim 14$  nm are shown in Figure 3.2. The onset temperatures of the superprotonic phase transitions in KH(PO<sub>3</sub>H) and composites KH(PO<sub>3</sub>H)-SiO<sub>2</sub> are indicated in the figure. It is seen that the onset temperature decreases from 125 °C to 101 °C upon increasing the SiO<sub>2</sub> mass fraction from  $\omega = 0$  (pure KH(PO<sub>3</sub>H)) to  $\omega = 0.5$ . Simultaneously, the endothermic heat of the phase transition decreases. The observations are interpreted to reflect the structural disordering, and/or amorphization, due to surface interactions of the solid acid with SiO<sub>2</sub>. Many hydrogen bonds are weakened or broken, especially in the vicinity of the silica surface, due to interaction of the proton-carrying oxyanion groups with, for example, silanol groups at the silica surface [25]. The observed

lowering of the phase transition temperature with increasing  $\text{SiO}_2$  content indicates lowering of the enthalpy of the first-order monoclinic-to-cubic phase transition dominates over possible changes in the excess entropy associated with the phase transition.

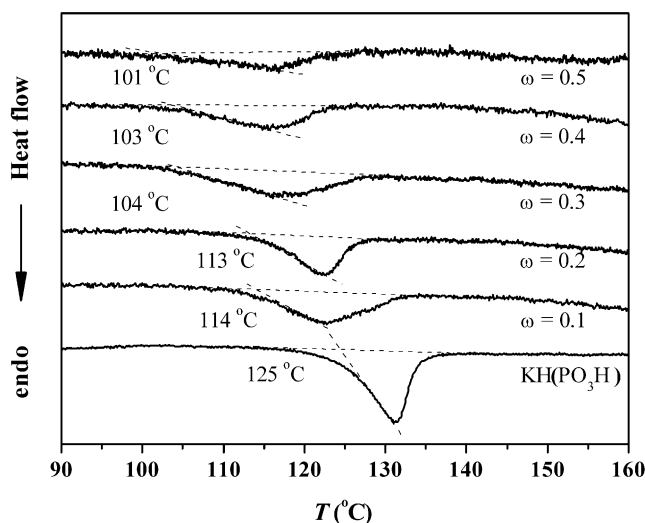


**Figure 3.2** DTA curves for  $\text{KH}(\text{PO}_3\text{H})\text{-SiO}_2$  composites with different mass fractions ( $\omega$ ) of  $\text{SiO}_2$  ( $d_p \approx 14$  nm). Measurements were performed under flowing dry nitrogen at a heating rate of  $3 \text{ K min}^{-1}$ . Data were normalized to the number of moles  $\text{KH}(\text{PO}_3\text{H})$ . The extrapolated onset temperature of the superprotonic phase transition occurring in each of the compositions is indicated.

Figure 3.3 shows the effect of particle size on the data of thermal analysis of composites  $\text{KH}(\text{PO}_3\text{H})\text{-SiO}_2$ . Decreasing the particle size of  $\text{SiO}_2$  dispersoids, at constant  $\text{SiO}_2$  mass fraction, lowers the heat of the phase transition. Concomitantly, the superprotonic phase transition temperature is lowered from  $125 \text{ }^{\circ}\text{C}$  for pure  $\text{KH}(\text{PO}_3\text{H})$  to  $120 \text{ }^{\circ}\text{C}$ ,  $114 \text{ }^{\circ}\text{C}$  and  $113 \text{ }^{\circ}\text{C}$  upon decreasing the  $\text{SiO}_2$  particle size from  $2 \text{ }\mu\text{m}$ ,  $80 \text{ nm}$  to  $14 \text{ nm}$ , respectively. These observations

are seemingly explained by the increased surface area of the  $\text{SiO}_2$  dispersoids with decreasing particle size. BET measurements, however, indicate that the trend for their specific surface areas is different;  $0.91 \text{ m}^2 \text{ g}^{-1}$ ,  $326 \text{ m}^2 \text{ g}^{-1}$ , and  $196 \text{ m}^2 \text{ g}^{-1}$  for  $\text{SiO}_2$  with particle sizes  $2 \mu\text{m}$ ,  $80 \text{ nm}$  to  $14 \text{ nm}$ , respectively. The latter is most likely related to a different internal pore structure of the  $\text{SiO}_2$  dispersoids. Since the data of thermal analysis, as presented in Figure 3.3, exhibits a clear trend with particle size, it is suggested that infiltration of  $\text{KH}(\text{PO}_3\text{H})$  in pores of the  $\text{SiO}_2$  dispersoids is limited.

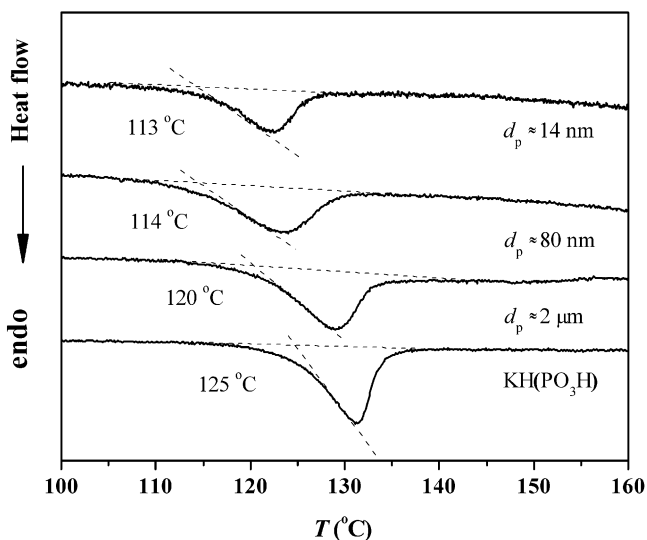


**Figure 3.3** DTA curves for  $\text{KH}(\text{PO}_3\text{H})\text{-SiO}_2$  ( $\omega = 0.2$ ) composites with different particle size of the  $\text{SiO}_2$  dispersoids. Measurements were performed under flowing dry nitrogen at a heating rate of  $3 \text{ K min}^{-1}$ . Data were normalized to the number of moles  $\text{KH}(\text{PO}_3\text{H})$ . The extrapolated onset temperature of the superprotonic phase transition occurring in each of the compositions is indicated.

### 3.3.2 Impedance measurements

Arrhenius plots of the proton conductivity of  $\text{KH}(\text{PO}_3\text{H})\text{-SiO}_2$  composites from ac impedance measurements are presented in Figure 3.4. Also shown in the figure are the extrapolated onset temperatures of the superprotonic phase transitions. The conductivity of  $\text{KH}(\text{PO}_3\text{H})$  increases profoundly at the superprotonic phase transition, rising to a value of  $4.2 \cdot 10^{-3} \text{ S cm}^{-1}$  at  $140 \text{ }^\circ\text{C}$ , which is in agreement with prior results [13]. It is immediately evident that the discontinuity of the conductivity behavior at the superprotonic phase transition is smoothed in the composite electrolytes as a result of significant enhancement of the low temperature conductivity. The latter is more pronounced upon increasing the mass fraction of dispersed silica in the composite. For the composite with  $\text{SiO}_2$  mass fraction  $\omega = 0.5$  almost linear Arrhenius behavior is observed. Consistent with the data from thermal analysis, the superprotonic phase transition temperature is found to decrease with increasing the  $\text{SiO}_2$  mass fraction. A good correlation is found between both trends evaluated from conductivity measurements and thermal analysis. Of note is that the data of thermal analysis were obtained at a linear heating rate of  $3 \text{ K min}^{-1}$ , causing some possible delay, while the conductivity data were obtained after equilibration at each temperature for approximately half an hour.

Figure 3.5 shows the conductivity, at  $140 \text{ }^\circ\text{C}$ , *i.e.*, above the superprotonic phase transition temperature, as a function of  $\text{SiO}_2$  ( $d_p \approx 14 \text{ nm}$ ) mass fraction. It is seen that the conductivity is lowered by almost one order of magnitude by dispersing 50 wt% of silica in  $\text{KH}(\text{PO}_3\text{H})$ . Similar observations have been reported for solid acid based composites  $\text{CsHSO}_4\text{-SiO}_2$  [22],  $\text{CsHSO}_4\text{-TiO}_2$  [24], and  $\text{CsH}_2\text{PO}_4\text{-SiO}_2$  [1, 21]. The effect can be ascribed primarily to the reduced volume and the blocking of proton transport by the insulating silica particles, although in the case of  $\text{KH}(\text{PO}_3\text{H})\text{-SiO}_2$  composites a contribution to impeding

of proton transport by grain boundary effects cannot be excluded (see discussion below). Using the resistor network approach to predict the conductivity of randomly distributed phases developed by Wu and Liu [26], the percolation threshold would be predicted to occur at the volume fraction of 0.67.

In addition to data for SiO<sub>2</sub> particle size 14 nm, additional conductivity data is shown in Figure 3.5, at  $\omega = 0.2$ , for SiO<sub>2</sub> particle sizes  $\sim 2 \mu\text{m}$  and  $\sim 80 \text{ nm}$ . The conductivity is found to drop with lowering the particle size of SiO<sub>2</sub>. In accord with the larger degree of amorphization upon dispersion of SiO<sub>2</sub> into the KH(PO<sub>3</sub>H) matrix at lower particle sizes of SiO<sub>2</sub>, this observation suggests that grain boundary effects actually contribute to lowering of the conductivity of KH(PO<sub>3</sub>H)-SiO<sub>2</sub> composite in its superprotonic state. The low-temperature conductivity in the composites is enhanced, which is commonly attributed to contributions of fast proton transport along silica/solid acid interfaces. Proton hopping across the silica surface may occur via multiple sites, such as Si-O<sup>-</sup>, Si-OH and bridging siloxane, -Si-O-Si-, groups [27]. Water molecules may assist in hopping along the interface and/or transfer of protons from the solid acid to the SiO<sub>2</sub> surface. In fact, we have recently demonstrated that proton conductivity in KH(PO<sub>3</sub>H)-SiO<sub>2</sub> ( $\omega = 0.1$ ) in its superprotonic state, at 142 °C, is enhanced over more than order of magnitude by increasing the humidity level from  $p\text{H}_2\text{O} = 0.05$  to  $p\text{H}_2\text{O} = 0.6 \text{ atm}$ , while no evidence of such an enhancement is found in KH(PO<sub>3</sub>H) and silica in their phase pure modifications (Chapter 5). It is anticipated that humidity will also enhance the proton conductivity of KH(PO<sub>3</sub>H)-SiO<sub>2</sub> composites below their superprotonic phase transition temperature. This needs to be confirmed by experiment.

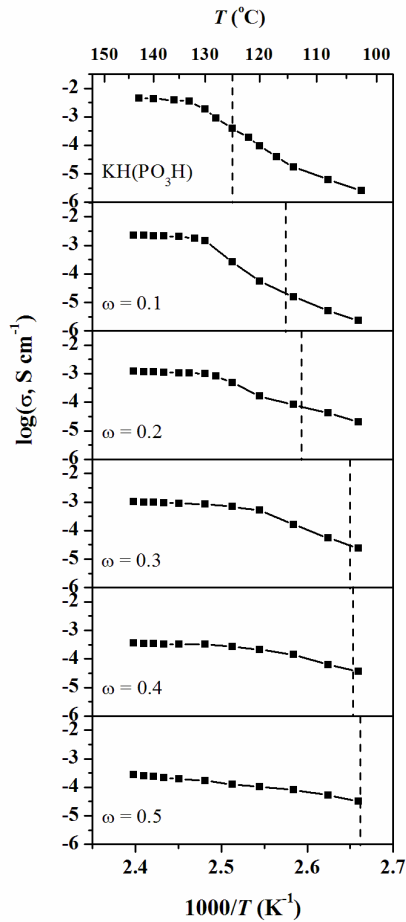


**Figure 3.4** Arrhenius plots of the proton conductivity of KH(PO<sub>3</sub>H)-SiO<sub>2</sub> composites with different mass fractions  $\omega$  of SiO<sub>2</sub> ( $d_p \approx 14$  nm). Measurements were performed in humidified air ( $p_{\text{H}_2\text{O}} = 0.02$  atm). The dashed lines indicate the extrapolated onset temperatures of the superprotonic phase transition estimated from data of DTA (see Figures 3.2).

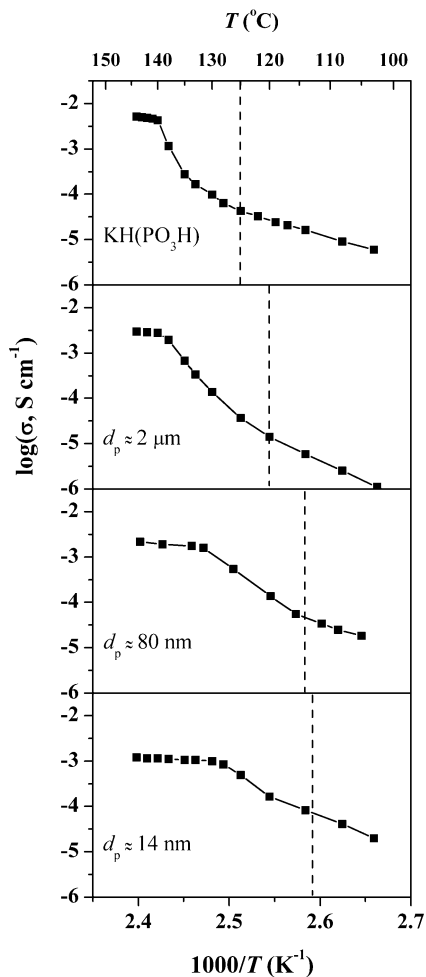


**Figure 3.5** Arrhenius plots of the proton conductivity of  $\text{KH}(\text{PO}_3\text{H})\text{-SiO}_2$  ( $\omega = 0.2$ ) composites with different particle size of the dispersoids  $\text{SiO}_2$ . Measurements were performed in humidified air ( $p_{\text{H}_2\text{O}} = 0.02$  atm). The dashed lines indicate the extrapolated onset temperatures of the superprotonic phase transition estimated from data of DTA (see Figure 3.3).



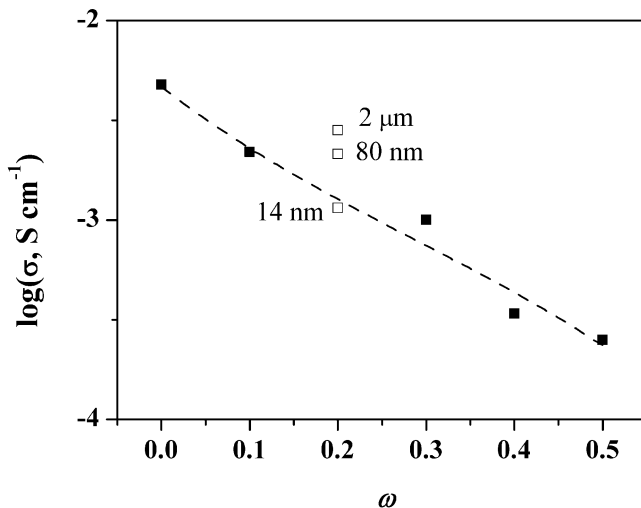


**Figure 3.6** Superprotonic conductivity, at 140 °C, of  $\text{KH}(\text{PO}_3\text{H})\text{-SiO}_2$  as a function of the mass fraction  $\omega$  of  $\text{SiO}_2$  ( $d_p \approx 14$  nm). Data were taken from Figure 3.4. Also shown are conductivity data, at  $\omega = 0.2$ , for  $\text{SiO}_2$  particle sizes  $\sim 80$  nm and  $\sim 2\mu\text{m}$  (from Figure 3.5).

### 3.3.3 Stability measurements

Duration tests were conducted at 140 °C to evaluate the effect of dehydration on the conductivity of  $\text{KH}(\text{PO}_3\text{H})$ , in its pure form, and that of the composite  $\text{KH}(\text{PO}_3\text{H})\text{-SiO}_2$  ( $\omega = 0.2$ ). Figure 3.7 shows that the superprotonic conductivity of pure  $\text{KH}(\text{PO}_3\text{H})$  in dry nitrogen gradually decreases with time due to slow dehydration. Dehydration caused the pressed disc of  $\text{KH}(\text{PO}_3\text{H})$  to lose much of its mechanical strength. A water partial pressure as low as  $p_{\text{H}_2\text{O}} = \sim 0.02$  atm, however, turned out to be sufficient to suppress dehydration of both  $\text{KH}(\text{PO}_3\text{H})$  and  $\text{KH}(\text{PO}_3\text{H})\text{-SiO}_2$  ( $\omega = 0.2$ ). The curve 2 in Figure 3.7 shows that  $\text{KH}(\text{PO}_3\text{H})\text{-SiO}_2$  ( $\omega = 0.2$ ) exhibits a stable proton conductivity of  $\sim 1.2 \cdot 10^{-3} \text{ S cm}^{-1}$  under the experimental conditions over more than 80 h. Besides the enhancement of the mechanical properties, and preservation of its

mechanical properties under the conditions of the experiments, it was found that hygroscopicity of  $\text{KH}(\text{PO}_3\text{H})\text{-SiO}_2$  was greatly reduced relative to parent  $\text{KH}(\text{PO}_3\text{H})$ .

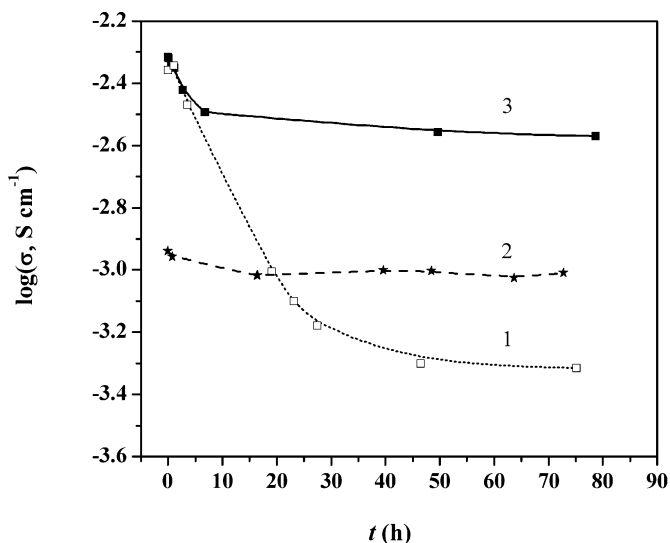


**Figure 3.7** Time dependence of the superprotonic conductivity, at 140 °C, of (1) pure  $\text{KH}(\text{PO}_3\text{H})$  in dry nitrogen, (2)  $\text{KH}(\text{PO}_3\text{H})\text{-SiO}_2$  ( $\omega = 0.2$ ;  $d_p \approx 14$  nm) in air,  $p_{\text{H}_2\text{O}} = 0.02$  atm and (3). pure  $\text{KH}(\text{PO}_3\text{H})$  in air,  $p_{\text{H}_2\text{O}} = 0.02$  atm,

### 3.3.4 Thin film composite electrolyte

Reducing the electrolyte thickness is a preferable way to reduce Ohmic losses. Figure 3.8 shows a typical scanning electron micrograph of a thin film of the composite electrolyte  $\text{KH}(\text{PO}_3\text{H})\text{-SiO}_2$  ( $\omega = 0.2$ ;  $d_p = 14$  nm) produced by dip-coating on a Pt pre-coated silicon wafer. The high-temperature specific conductivity measured for the thin film is found to be in good agreement with that measured for pressed specimens. As shown in the inset of Figure 3.9, the area specific resistance (ASR) decreases linearly with film thickness to reach  $\sim 1 \Omega \text{ cm}^2$  at the lowest value within the experimental range 10 - 50  $\mu\text{m}$ .

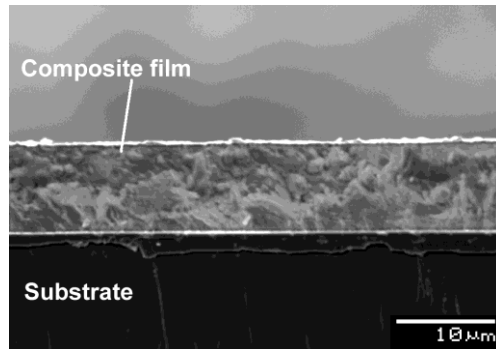


**Figure 3.8** Cross-sectional scanning electron microscopy (SEM) image of a KH(PO<sub>3</sub>H)-SiO<sub>2</sub> film ( $\omega = 0.2$ ;  $d_p \approx 14$  nm).

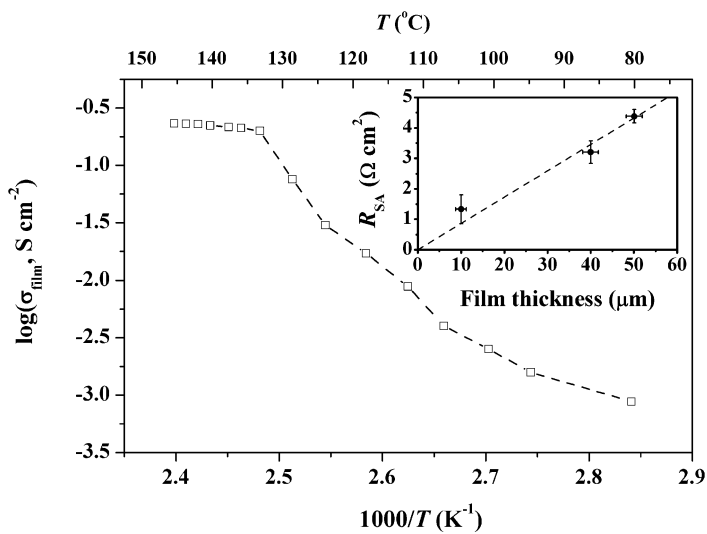


**Figure 3.9** Arrhenius plot of the area specific conductivity ( $\sigma_{\text{AS}}$ ) of a thin film of composite electrolyte KH(PO<sub>3</sub>H)-SiO<sub>2</sub> ( $\omega = 0.2$ ;  $d_p \approx 14$  nm) with thickness  $\sim 10$   $\mu\text{m}$  (see Figure 3.7). Data was collected in humidified air ( $p_{\text{H}_2\text{O}} = 0.02$  atm). The inset shows the dependence of the area specific resistance (ASR) on film thickness, at 140  $^{\circ}\text{C}$ .

### **3.4 Conclusions**

The influence of dispersion of nano particulate  $\text{SiO}_2$  on the superprotonic phase transition in  $\text{KH}(\text{PO}_3\text{H})$  has been investigated using X-ray powder diffraction, thermal analysis and conductivity measurements. X-ray diffraction patterns of samples obtained by variation of either the  $\text{SiO}_2$  mass fraction (in range 0 - 0.5) or particle diameter (in range 14 nm - 80  $\mu\text{m}$ ) indicate significant loss of crystallinity or increase of amorphization, increasing with the degree of  $\text{SiO}_2$  dispersion. Along with amorphization, significant reduction of the onset temperature of the superprotonic phase transition (as confirmed by DTA and conductivity measurements), and smoothing of the associated characteristic discontinuity in the proton conductivity occur. While above the superprotonic phase transition temperature the proton conductivity is lowered owing to reduced volume and blocking effects of insulating  $\text{SiO}_2$  nano particles, the low-temperature conductivity is significantly enhanced. The latter is attributed to the presence of fast conduction pathways along  $\text{KH}(\text{PO}_3\text{H})/\text{SiO}_2$  interfaces. As an example, at  $\text{SiO}_2$  mass fraction  $\omega = 0.5$  ( $d_p \approx 14$  nm), the protonic conductivity, at 140 °C, has dropped almost one order of magnitude relative to parent  $\text{KH}(\text{PO}_3\text{H})$ , while the conductivity discontinuity at the superprotonic phase transition temperature is scarcely noticeable.

As shown previously  $\text{KH}(\text{PO}_3\text{H})$  can be operated in both oxidizing and reducing atmospheres [14]. Besides improvement of its mechanical properties, the dispersion with nano particulate  $\text{SiO}_2$  is found to reduce hygroscopicity of  $\text{KH}(\text{PO}_3\text{H})$ . It is demonstrated that the dispersion-strengthened composite electrolytes can be easily made into a thin film in the  $\mu\text{m}$  range, whereas a slight humidification of the gas streams (with an equivalent  $p_{\text{H}_2\text{O}}$  of 0.02 atm) prevents degradation of the proton conductivity due to partial dehydration of  $\text{KH}(\text{PO}_3\text{H})$ . The elevated temperature of operation and low humidification

requirement of the  $\text{KH}(\text{PO}_3\text{H})\text{-SiO}_2$  thin films will enable significant system simplifications in comparison with polymer electrolyte fuel cells.

## References

1. J. Otomo, N. Minagawa, C.J. Wen, K. Eguchi, H. Takahashi, *Solid State Ionics* 156 (2003) 357.
2. G.V. Lavrova, M.V. Russkikh, V.G. Ponomareva, N.F. Uvarov, *Russ. J. Electrochem.* 41 (2005) 485.
3. S.M. Haile, D.A. Boysen, C.R.I. Chisholm, R.B. Merle, *Nature* 410 (2001) 910.
4. D.A. Boysen, T. Uda, C.R.I. Chisholm, S.M. Haile, *Science* 303 (2004) 68.
5. A.I. Baranov, L.A. Shuvalov, N.M. Shchagina, *JETP Lett.* 36 (1982) 459.
6. A.I. Baranov, V.P. Khiznichenko, L.A. Shuvalov, *Ferroelectrics* 100 (1989) 135.
7. H.S. Lee, M.E. Tuckerman, *J. Phys. Chem. C* 112 (2008) 9917.
8. D.A. Boysen, S.M. Haile, H.J. Liu, R.A. Secco, *Chem. Mater.* 15 (2003) 727.
9. E. Ortiz, R.A. Vargas, B.E. Mellander, *Journal of Physics-Condensed Matter* 18 (2006) 9561.
10. T. Uda, D.A. Boysen, S.M. Haile, *Solid State Ionics* 176 (2005) 127.
11. S.M. Haile, C.R.I. Chisholm, R.B. Merle, D. Boysen, S.R. Narayanan, *Solid acid electrolytes for electrochemical devices* In: USPTO, Editor, United States of America (2009).
12. J. Otomo, T. Tamaki, S. Nishida, S.Q. Wang, M. Ogura, T. Kobayashi, C.J. Wen, H. Nagamoto, H. Takahashi, *J. Appl. Electrochem.* 35 (2005) 865.
13. W.H. Zhou, A.S. Bondarenko, B.A. Boukamp, H.J.M. Bouwmeester, *Solid State Ionics* 179 (2008) 380.
14. A.S. Bondarenko, W.H. Zhou, H.J.M. Bouwmeester, *J. Power Sources* 194 (2009) 843.

15. V.G. Ponomareva, G.V. Lavrova, V.V. Malakhov, L.S. Dovlitova, *Inorg. Mater.* 42 (2006) 1115.
16. K. Sasaki, Electrochemical characterization of solid acid fuel cell electrodes, California Institute of Technology, Ph.D., (2009).
17. B.A. Boukamp, *J. Electrochem. Soc.* 142 (1995) 1885.
18. B.A. Boukamp, *Solid State Ionics* 169 (2004) 65.
19. B.A. Boukamp, *Solid State Ionics* 20 (1986) 31.
20. B.A. Boukamp, *Solid State Ionics* 18-9 (1986) 136.
21. S.Q. Wang, J. Otomo, M. Ogura, C. Wen, H. Nagamoto, H. Takahashi, *Solid State Ionics* 176 (2005) 755.
22. V.G. Ponomareva, N.F. Uvarov, G.V. Lavrova, E.F. Hairetdinov, *Solid State Ionics* 90 (1996) 161.
23. G.V. Lavrova, V.G. Ponomareva, *Inorg. Mater.* 38 (2002) 1172.
24. V.G. Ponomareva, G.V. Lavrova, *Solid State Ionics* 106 (1998) 137.
25. N.F. Uvarov, V.G. Ponomareva, G.V. Lavrova, *Russ. J. Electrochem.* 46 (2010) 722.
26. Z. Wu, M. Liu, *Solid State Ionics* 93 (1996) 65.
27. G.K. Lockwood, S.H. Garofalini, *J. Chem. Phys.* 131 (2009) 074703.

## 4 Superprotonic phase transitions in solid solutions $K_{1-x}Cs_xH(PO_3H)$ and $K_{1-x}(NH_4)_xH(PO_3H)$

### **Abstract**

*The effect of  $Cs^+$  or  $NH_4^+$  substitution for  $K^+$  on the proton transport properties of  $KH(PO_3H)$  have been studied by X-Ray powder diffraction, differential thermal analysis and conductivity measurements. Partial substitution in both series  $K_{1-x}Cs_xH(PO_3H)$  and  $K_{1-x}(NH_4)_xH(PO_3H)$  ( $0 \leq x \leq 1$ ) lowers the endothermic heat associated with the superprotonic phase transition and, consequently, the onset temperature of the transition relative to that exhibited by the end-members. This is most pronounced for  $K_{0.1}(NH_4)_{0.9}H(PO_3H)$ , where the onset temperature of the superprotonic phase transition is observed as low as  $67^\circ C$ , as compared to  $125^\circ C$  and  $127^\circ C$  observed for  $KH(PO_3H)$  and  $(NH_4)H(PO_3H)$ , respectively (albeit that for the given composition a second superprotonic transition may be discerned at  $\sim 114^\circ C$ , which is close to the onset temperature of melting). These observations suggest that in the solid solutions the hydrogen bonds are either weakened, relative to their strength in the parent compounds, or broken. Contrary to  $K_{1-x}(NH_4)_xH(PO_3H)$ , isovalent substitution of  $Cs^+$  for  $K^+$  in  $KH(PO_3H)$  significantly increases the low-temperature conductivity, which*



*renders conductivity rises at the superprotonic phase transition in this series scarcely noticeable or even absent. The results from this study demonstrate that homogeneous substitution of solid acids offers a useful strategy for tuning the properties of proton-conducting solid acids.*

## 4.1 Introduction

Superprotonic phase transitions are known to occur in a number of solid acids, among which  $\text{CsH}_2\text{PO}_4$  and  $\text{CsHSO}_4$ , which materials can be considered as prototypes for potential use as electrolyte in intermediate temperature fuel cells [1-7]. The proton conductivity may increase several orders of magnitude at the transition, which is imparted by the disordering of the hydrogen-bond network above the phase transition. On passing through the superprotonic transition, the structure transforms from, usually, low-symmetry monoclinic to a crystal structure with high symmetry, cubic, tetragonal or rhombohedral.

To date, however, there is no compelling explanation as to why the superprotonic phase transition appears only in a limited number of solid acids. The role of the hydrogen-bonded network and that of the relative sizes of the constituent cations and anions on the occurrence of the phase transition are not clear. In this study, we employ homogenous substitution of the solid acid as a strategy, on one hand, to distort the hydrogen-bonded network and to see how this affects the disordering of the H-bonded network, and, on the other hand, to tune the properties of the solid acid under consideration.

Homogeneous substitution of solid acids has been the subject of a limited number of studies. Investigations in the system  $\text{NaHSO}_4$ - $\text{CsHSO}_4$  by Chisholm *et al.* [8] yielded the compounds  $\text{CsNa}_2(\text{HSO}_4)_3$  and  $\text{Cs}_2\text{Na}(\text{HSO}_4)_3$ . Thermal analysis demonstrated the absence of phase transitions for both compounds prior to melting. It should be noted that for the alkali acid sulfates  $\text{M}(\text{HSO}_4)_x$ , with  $\text{M} = \text{Li}^+$ ,  $\text{Na}^+$ ,  $\text{K}^+$ ,  $\text{NH}_4^+$ ,  $\text{Rb}^+$  and  $\text{Cs}^+$ , only the cesium-containing compound displays a superprotonic phase transition. Double salts of  $\text{CsHSO}_4$ - $\text{CsH}_2\text{PO}_4$  [9-14] and  $\text{CsHSO}_4$ - $\text{CsHSeO}_4$  [15] were investigated to explore the effect of anion substitution on superprotonic behavior. The end-members in both series all display a superprotonic phase transition. Four mixed sulfate-

phosphate compounds were found in the  $\text{CsHSO}_4\text{-CsH}_2\text{PO}_4$  system, each of them with a unique structure and hydrogen-bonded network [9-14]. Three of them display a superprotonic phase transition, among which  $\text{Cs}_2(\text{HSO}_4)(\text{H}_2\text{PO}_4)$ , in which the transition was presumed to take place in a two-step process [9]. For  $\text{CsHSO}_4\text{-CsHSeO}_4$ , the properties can be tuned in a proportion of the constituent isostructural end-members [14].

Recently, we reported a new family of solid acids,  $\text{MH}(\text{PO}_3\text{H})$  with  $\text{M} = \text{Li}^+$ ,  $\text{Na}^+$ ,  $\text{K}^+$ ,  $\text{Rb}^+$ ,  $\text{Cs}^+$ , and  $\text{NH}_4^+$  [16]. Within this family, all members, except  $\text{Li}^+$  (having the smallest size within this series), exhibit a superprotonic phase transition. We have undertaken a study of the solid solutions formed in the systems  $\text{KH}(\text{PO}_3\text{H})\text{-NH}_4\text{H}(\text{PO}_3\text{H})$  and  $\text{KH}(\text{PO}_3\text{H})\text{-CsH}(\text{PO}_3\text{H})$  in order to investigate the compositional control on disordering of the H-bonded network and associated proton conductivity. Combined X-ray powder diffraction, thermal analysis and conductivity measurements is used to detect the superprotonic transitions in the apparent solid solutions.

## 4.2 Experimental

Powders of  $\text{K}_{1-x}\text{Cs}_x\text{H}(\text{PO}_3\text{H})$  and  $\text{K}_{1-x}(\text{NH}_4)_x\text{H}(\text{PO}_3\text{H})$  ( $x = 0, 0.1, 0.2 \dots 1$ ) were prepared by slow evaporation of aqueous solutions of KOH (Merck, 99.5%),  $\text{Cs}_2\text{CO}_3$  carbonate (Merck),  $\text{NH}_4\text{HCO}_3$  (Alfa Aesar),  $\text{H}_3\text{PO}_3$  (Aldrich, 99%) mixed in the correct stoichiometric ratios. The obtained powders were dried in air at  $\sim 105^\circ\text{C}$  overnight and stored in a desiccator.

X-ray diffraction (XRD) powder patterns were recorded at room temperature using a Philips XRD PW3020 (50kV, 35 mA,  $\text{Cu K}\alpha_1$ ) diffractometer. Rietveld refinement was performed using WinPLOTR program [17]. Thermal analysis was performed using differential thermal analysis (DTA) on a Setaram SETSYS

16/18 apparatus. Measurements were carried out under flowing nitrogen (45 ml min<sup>-1</sup>) at a linear heating rate of 3 K min<sup>-1</sup>.

For electrical conductivity measurements, the powders were isostatically pressed at 400 MPa into discs 10 mm in diameter and 1 mm in thickness. The relative density was about 90%. Gold electrodes were sputtered on both sides of the discs using a JOEL JFC-1300 auto coating machine. The conductivity measurements were performed using electrochemical impedance spectroscopy (EIS), using a PGstat20 Autolab Potentiostat (ECO-Chemie) with integrated frequency response analyzer, in dried N<sub>2</sub> with a flow rate of 20 ml min<sup>-1</sup>. An excitation voltage with an amplitude of 10 mV was used to ensure that measurements were performed in the linear regime. No bias voltage was applied. The temperature was incremented to a new setpoint, with a heating/cooling rate of 0.8 K min<sup>-1</sup>, at which the sample was equilibrated for at least 30 min. Impedance spectra were recorded over the frequency range 0.5 MHz to 100 Hz below, and from 50 kHz to 100 or 10 Hz above the superprotonic phase transition temperature, and approved for further data analysis only after passing a Kramer-Kronig transformation test [18, 19]. EIS data analysis was carried out using complex nonlinear least squares fitting routines [20-22].

## **4.3 Results and discussions**

### **4.3.1 Phase analysis by X-ray powder diffraction**

The synthesis of K<sub>1-x</sub>Cs<sub>x</sub>H(PO<sub>3</sub>H) and K<sub>1-x</sub>(NH<sub>4</sub>)<sub>x</sub>H(PO<sub>3</sub>H) yielded white crystalline powders. Through variation of the salt concentrations in the initial aqueous solutions, the stoichiometry could be varied from x = 0 to x = 1. XRD

powder diffraction patterns of the compositions prepared in both series collected at room temperature are presented in Figures 4.1 and 4.2, respectively.

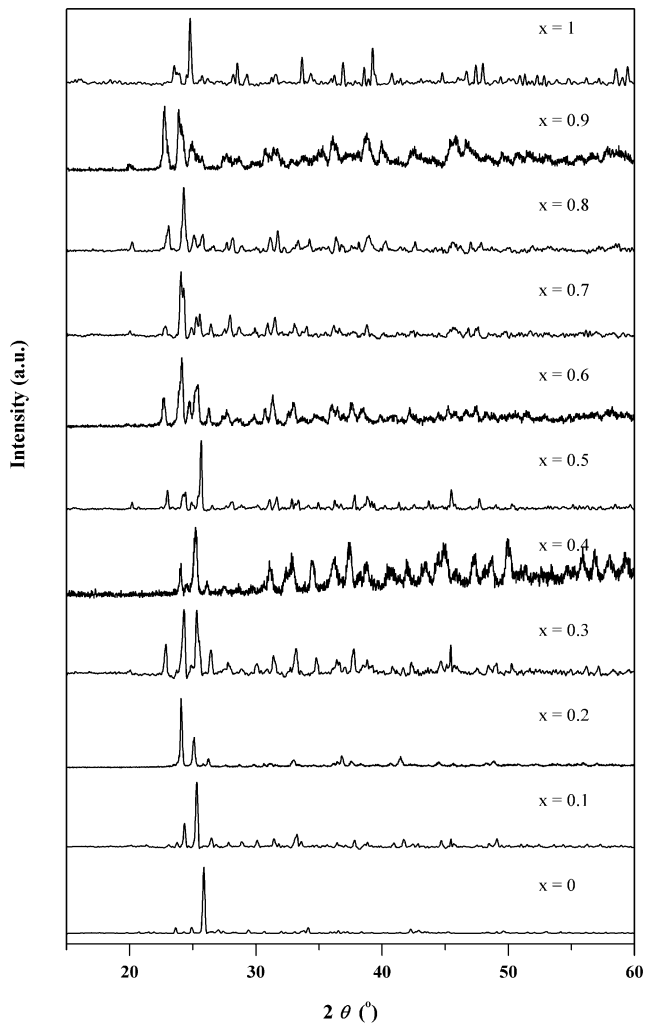


**Figure 4.1** X-ray powder diffraction patterns of solid solutions  $K_{1-x}Cs_xH(PO_3H)$  collected at room temperature.

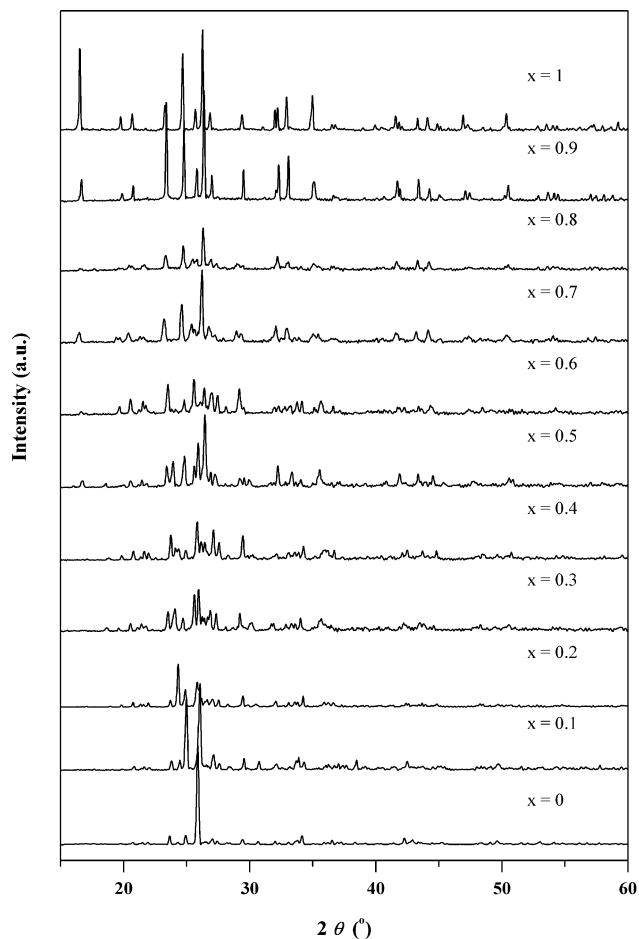


**Figure 4.2** X-ray powder diffraction patterns of solid solutions  $K_{1-x}(NH_4)_xH(PO_3H)$  collected at room temperature.

The end-members,  $KH(PO_3H)$ ,  $CsH(PO_3H)$  and  $(NH_4)H(PO_3H)$ , in both series crystallize in the monoclinic space group,  $P2_1/c$  [23-25]. In their low-temperature structures, the  $PO_3H$  tetrahedra are connected through hydrogen bonds forming infinite  $-H(PO_3H)-$  chains [26]. Cell parameters obtained from Rietveld refinements of the XRD powder patterns of the end-members are listed in Table 4.1, showing good agreement with corresponding data reported in

literature [23-25]. Little variation was noted in the cell parameters of solid solutions  $K_{1-x}Cs_xH(PO_3H)$  and  $K_{1-x}(NH_4)_xH(PO_3H)$  for compositions close to the end-members. Multiphase profile refinements of the XRD patterns of compositions with intermediate values of  $x$  gave very poor results (inherent to the poor resolution of the obtained XRD patterns), and no conclusive evidence was obtained for phase separation or formation of inhomogeneous mixtures.

**Table 4.1** Comparison of structural parameters for  $KH(PO_3H)$ ,  $NH_4H(PO_3H)$  and  $CsH(PO_3H)$  from this study with literature data.

		a (Å)	b (Å)	c (Å)	$\beta$ (°)
KH(PO <sub>3</sub> H)	Ref [24]	7.341(1)	8.579(2)	11.975(3)	101.98(2)
	This work	7.352(3)	8.575(3)	11.985(5)	101.95(1)
NH <sub>4</sub> H(PO <sub>3</sub> H)	Ref [25]	6.273(1)	8.323(2)	8.902(2)	120.11(2)
	This work	6.277(2)	8.243(3)	8.914(3)	120.18(1)
CsH(PO <sub>3</sub> H)	Ref [23]	7.930(2)	8.929(2)	13.163(3)	104.84(3)
	This work	7.948(3)	8.934(3)	13.168(5)	104.81(1)

### 4.3.2 Thermal analysis

Differential thermal analysis results obtained upon heating powders of compositions in both series  $K_{1-x}Cs_xH(PO_3H)$  and  $K_{1-x}(NH_4)_xH(PO_3H)$  are presented in Figures 4.3 and 4.4, respectively. The extrapolated onset temperatures of thermal events are indicated in the figures. The first order endothermic peaks observed for the end-members  $KH(PO_3H)$ ,  $CsH(PO_3H)$  and  $(NH_4)H(PO_3H)$  in both series, with extrapolated onset temperatures of 125 °C, 140 °C, and 127 °C, respectively, correspond to those at which superprotonic

phase transitions have been reported [16, 17], as confirmed by conductivity measurements in the present study (see next section).

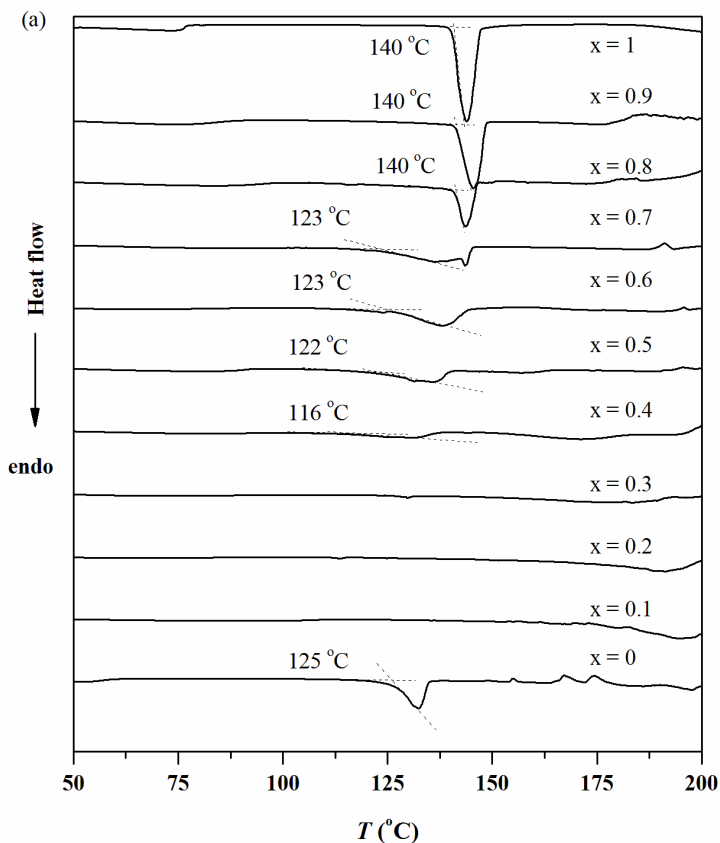


**Figure 4.3** DTA curves of solid solutions  $K_{1-x}Cs_xH(PO_3H)$  recorded under flowing nitrogen at a heating rate of  $3 \text{ K min}^{-1}$ . Data were normalized to the number of moles. The extrapolated onset temperature of the superprotonic phase transition occurring in each of the compositions is indicated.

In both  $K_{1-x}Cs_xH(PO_3H)$  and  $K_{1-x}(NH_4)_xH(PO_3H)$ , the heat of the superprotonic phase transition is noticeably large for the end-members, while it is substantially smaller in the apparent solid solutions formed. This observation



suggests that H-bonds are weakened and/or broken in the solid solutions, which probably arises from disruption of general periodicity, creating disorder in the arrangement of the constituent cations and anions.

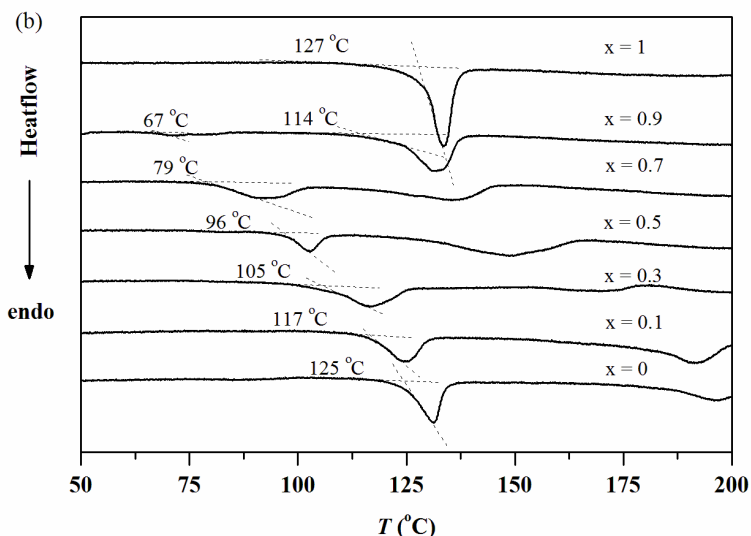


**Figure 4.4** DTA curves of solid solutions  $K_{1-x}(NH_4)_xH(PO_3H)$  recorded under flowing nitrogen at a heating rate of  $3 \text{ K min}^{-1}$ . Data were normalized to the number of moles. The extrapolated onset temperature of the superprotonic phase transition occurring in each of the compositions is indicated.

In the case of  $K_{1-x}Cs_xH(PO_3H)$ , the onset temperature of the superprotonic phase transition is reduced from  $140 \text{ °C}$  for  $x = 1$  to  $116 \text{ °C}$  for  $x = 0.4$ , which is accompanied by a substantial lowering of the heat of transformation, whilst no heat effect at all can be discerned from the DTA curves for compositions  $x = 0.2$  and  $x = 0.1$ .

For  $K_{1-x}(NH_4)_xH(PO_3H)$ , the extrapolated onset temperature of the endothermic peak associated with the superprotonic transition shifts from  $125 \text{ °C}$  for  $KH(PO_3H)$  to a minimum value as low as  $67 \text{ °C}$  observed for

$K_{0.1}(NH_4)_{0.9}H(PO_3H)$ . The latter is accompanied with a gradual lowering of the heat of transition upon partial substitution of the potassium for ammonium ions, which corresponds to an increase in the stoichiometry parameter  $x$  in  $K_{1-x}(NH_4)_xH(PO_3H)$ . Melting of  $KH(PO_3H)$  occurs at  $\sim 190$  °C, which is characterized by a broad endothermic event in the corresponding DTA curve. For  $(NH_4)H(PO_3H)$ , the endothermic peak associated with the superprotonic phase transition, at 127 °C, is known to overlap with that of melting. Note that upon partial substitution of potassium for ammonium ions, i.e., increasing  $x$  in  $K_{1-x}(NH_4)_xH(PO_3H)$ , the melting point is gradually lowered between the values of the end-members.

### **4.3.3 AC impedance spectroscopy**

Arrhenius plots of the equilibrium proton conductivities of pressed samples of  $K_{1-x}Cs_xH(PO_3H)$  are presented in Figure 4.5. The superprotonic phase transition at which the conductivity jumps noticeably is clearly visible for both end-members  $KH(PO_3H)$  and  $CsH(PO_3H)$ . In their superprotonic states, the conductivity is characterized by a small activation energy due to the fully disordered nature of the hydrogen bond network. As illustrated in the figure, the temperatures at which the conductivity jump occurs for each of the compositions  $K_{1-x}Cs_xH(PO_3H)$  correlate well with the corresponding onset temperatures of the superprotonic phase transition estimated from data of differential thermal analysis (see Figure 4.3), with the notion that the latter were obtained at a linear heating rate of  $3 \text{ K min}^{-1}$ . Most surprising is that the low-temperature conductivity of the solid solutions is much higher than that of the end-members. For the compositions with  $x = 0.2$  and  $x = 0.1$ , no conductivity jump at all can be discerned from the conductivity plots, while the conductivity may reach values even higher than those found for the end-members in their

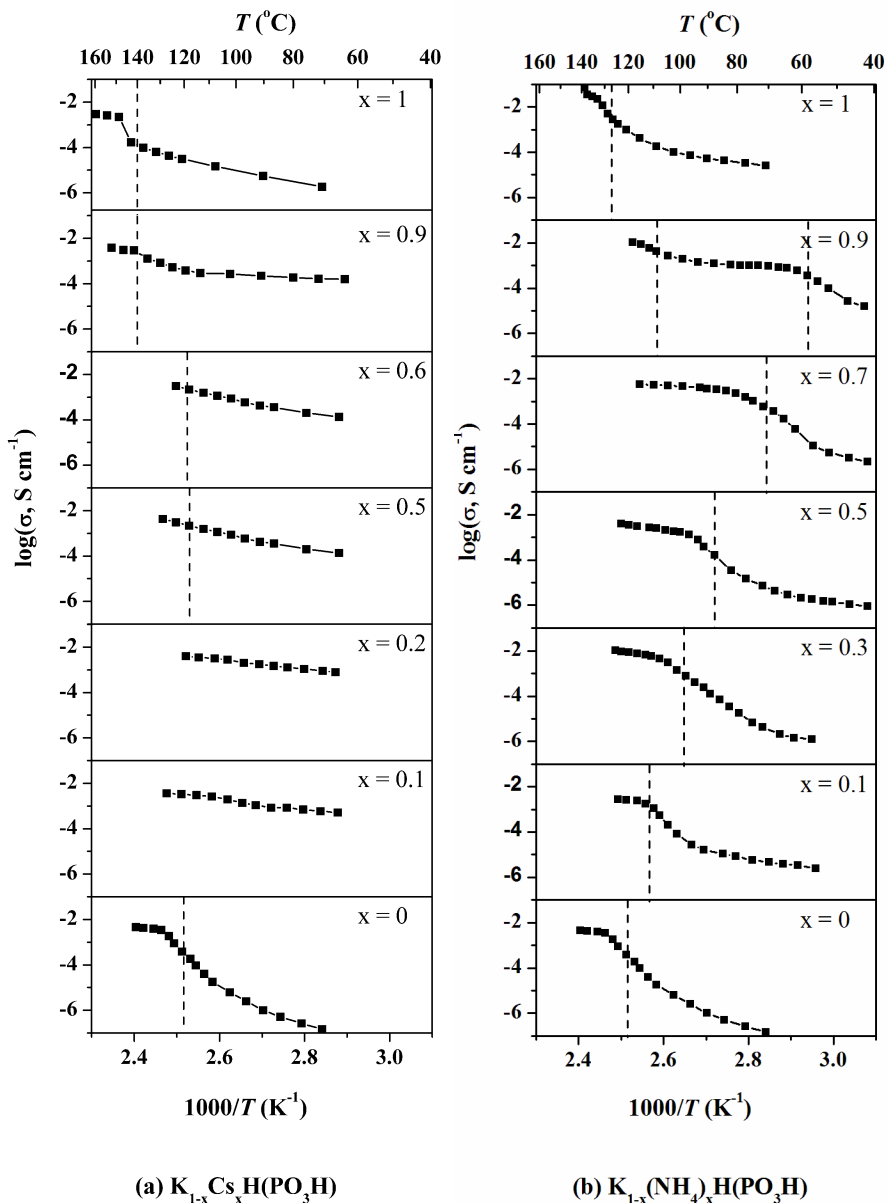


**Figure 4.5** Arrhenius plots of the equilibrium proton conductivity of solid solutions (a)  $K_{1-x}Cs_xH(PO_3H)$  and (b)  $K_{1-x}(NH_4)_xH(PO_3H)$ . Measurements were performed under dry nitrogen going from low to high temperature. The dashed lines indicate the extrapolated onset temperatures of the superprotonic phase transition estimated from data of DTA (see Figures 4.3 and 4.4).

transitions was also noted in corresponding data from thermal analysis (See Figure 4.3).

At present, we have no clear explanation for the observed low-temperature conductivity behavior of the solid solutions in the series  $K_{1-x}Cs_xH(PO_3H)$ . Generally, high conductivity in the solid acids is associated with rapid reorientations of the oxyanions groups that would occur only in the high temperature phase, i.e., upon a polymorphic phase transition from a 'low-conducting' phase to the superprotonic state. The combined data from thermal analysis and conductivity measurements of  $K_{1-x}Cs_xH(PO_3H)$  suggests that significant structural disorder is introduced in the hydrogen bond network in the low-temperature phase by partial substitution. This would explain the observed reduction of the heat effect on superprotonic phase transition and associated jump in the conductivity, or their absence, upon partial substitution. However, it cannot be excluded whether the low-temperature conductivity is due to proton migration through the bulk or along interfacial regions, the latter referring to common explanations for the enhancement of the low-temperature conductivity in solid acid systems obtained after dispersion with fine silica particles [27-31].

The conductivity results obtained for solid solutions  $K_{1-x}(NH_4)_xH(PO_3H)$  in this study are remarkably different from those for  $K_{1-x}Cs_xH(PO_3H)$ . Arrhenius plots of the conductivity of  $K_{1-x}(NH_4)_xH(PO_3H)$  are shown in Figure 4.5b. The superprotonic phase transition temperature decreases profoundly upon isovalent substitution of ammonium for potassium ions in  $KH(PO_3H)$  up to the composition  $K_{0.1}(NH_4)_{0.9}H(PO_3H)$ , which is in accord with the observations from differential thermal analysis (see Figure 4.4). It is readily apparent from the data in Figure 4.5 that this compound undergoes another apparent transition to a phase with slightly higher conductivity just before melting. According to the data of thermal analysis (see Figure 4.4), this transition would occur at  $\sim 114$  °C.

No enhancement of the low temperature conductivity is found for solid solutions of  $K_{1-x}(NH_4)_xH(PO_3H)$ . This result suggests that the order of the hydrogen bond network is maintained upon partial substitution. The latter can be reconciled by the similar sizes of potassium and ammonium ions, 1.38 Å and 1.43 Å ions, respectively, as opposed to potassium and cesium (1.67 Å) ions in solid solutions  $K_{1-x}Cs_xH(PO_3H)$ , but also by the likeness that more hydrogen bonds are formed upon substitution of potassium by ammonium ions. The presence of O—H—O and N—H—O bonds, for example, leads to a complex, three-dimensional network of hydrogen bonds in parent  $(NH_4)H(PO_3H)$  [25].

#### 4.4 Summary and conclusions

Partial substitution of  $K^+$  (1.38 Å) for  $NH_4^+$  (1.43 Å) ions in  $KH(PO_3H)$  is found to significantly lower the onset temperature of the superprotonic phase transition in  $KH(PO_3H)$ . For  $K_{0.1}(NH_4)_{0.9}H(PO_3H)$ , the onset temperature of the superprotonic phase transition is observed as low as 67 °C, as compared to 125 °C and 127 °C observed for  $KH(PO_3H)$  and  $(NH_4)H(PO_3H)$ , respectively (albeit that conductivity measurements provide evidence that the compound undergoes another transition, at ~114 °C, to a phase with a somewhat higher conductivity just before its melting). Similar observations are made for solid solutions  $K_{1-x}Cs_xH(PO_3H)$ . Upon partial substitution of  $Cs^+$  for  $K^+$  the heat of the superprotonic phase transition decreases with concomitant drop in the onset temperature of the superprotonic phase transition, from 140 °C for parent  $CsH(PO_3H)$  to 116 °C for  $K_{0.6}Cs_{0.4}H(PO_3H)$ . These results indicate that hydrogen bonds in the solid solutions are weakened, relative to their strength in the parent compounds, or broken.

There is, however, a remarkable difference upon isovalent substitution of either  $Cs^+$  or  $NH_4^+$  for  $K^+$  in  $KH(PO_3H)$ . Whilst measurements give evidence of

a significant conductivity rise for solid solutions  $K_{1-x}(NH_4)_xH(PO_3H)$  at the superprotonic phase transition, partial substitution of  $Cs^+$  for  $K^+$  in  $KH(PO_3H)$  significantly increases the low-temperature conductivity. This may render conductivity jumps at the superprotonic phase transition scarcely noticeable or even absent. The low-temperature conductivity of solid solutions  $K_{1-x}Cs_xH(PO_3H)$  may even exceed values as observed for their parent superprotonic end-members.

The results from this study clearly demonstrate that homogeneous substitution of solid acids may offer a useful strategy for tuning the properties of the proton-conducting solid acids. In view of their potential application as electrolyte in fuels, dedicated research is required to investigate the effect of doping on the structural and hydrothermal stability.

## References

1. D.A. Boysen, S.M. Haile, H.J. Liu, R.A. Secco, *Chem. Mater.* 15 (2003) 727.
2. A.I. Baranov, L.A. Shuvalov, N.M. Shchagina, *JETP Lett.* 36 (1982) 459.
3. T. Uda, D.A. Boysen, S.M. Haile, *Solid State Ionics* 176 (2005) 127.
4. S.M. Haile, C.R.I. Chisholm, K. Sasaki, D.A. Boysen, T. Uda, *Faraday Discuss.* 134 (2007) 17.
5. T. Uda, S.M. Haile, *Electrochem. Solid-State Lett.* 8 (2005) A245.
6. A.I. Baranov, V.V. Grebenev, A.N. Khodan, V.V. Dolbinina, E.P. Efremova, *Solid State Ionics* 176 (2005) 2871.
7. S.M. Haile, D.A. Boysen, C.R.I. Chisholm, R.B. Merle, *Nature* 410 (2001) 910.
8. C.R.I. Chisholm, L.A. Cowan, S.M. Haile, *Chem. Mater.* 13 (2001) 2909.
9. C.R.I. Chisholm, S.M. Haile, *Solid State Ionics* 136 (2000) 229.
10. S.M. Haile, P.M. Calkins, *J. Solid State Chem.* 140 (1998) 251.
11. S.M. Haile, P.M. Calkins, D. Boysen, *Solid State Ionics* 97 (1997) 145.
12. S.M. Haile, G. Lentz, K.D. Kreuer, J. Maier, *Solid State Ionics* 77 (1995) 128.
13. S.M. Haile, K.D. Kreuer, J. Maier, *Acta Crystallogr., Sect. B: Struct. Sci* 51 (1995) 680.
14. Y. Yamane, K. Yamada, K. Inoue, *Solid State Ionics* 179 (2008) 483.
15. Y. Matsuo, J. Hatori, Y. Yoshida, Y. Ikedo, J. Sugiyama, S. Ikehata, *Phys. Lett. A* 373 (2009) 3470.
16. W. Zhou, A.S. Bondarenko, B.A. Boukamp, H.J.M. Bouwmeester, *Solid State Ionics* 179 (2008) 380.
17. T. Roisnel, J. Rodriguez-Carvajal, WinPLOTR: a Windows tool for powder diffraction patterns analysis In: R. Delhez, E.J. Mittenmeijer, Editors, the

- 7th European Powder Diffraction Conference (EPDIC 7), Trans Tech Publications, Barcelona, Spain (2000).
18. B.A. Boukamp, *J. Electrochem. Soc.* 142 (1995) 1885.
  19. B.A. Boukamp, *Solid State Ionics* 169 (2004) 65.
  20. A.S. Bondarenko, G.A. Ragoisha, EIS Spectrum Analyser <http://www.abc.chemistry.bsu.by/vi/analyser/>, (2007).
  21. B.A. Boukamp, *Solid State Ionics* 18-9 (1986) 136.
  22. B.A. Boukamp, *Solid State Ionics* 20 (1986) 31.
  23. E.V. Kosterina, S.I. Troyanov, E. Kemnitz, L.A. Aslanov, *Russ. J. Coord. Chem.* 27 (2001) 458.
  24. B. Kratochvil, J. Podlahova, J. Hasek, *Acta Crystallogr., Sect. C: Cryst. Struct. Commun.* 39 (1983) 326.
  25. Z. Melichar, B. Kratochvil, J. Podlahova, V. Petricek, K. Maly, I. Cisarova, *Acta Crystallogr., Sect. C: Cryst. Struct. Commun.* 40 (1984) 720.
  26. C.R.I. Chisholm, R.B. Merle, D.A. Boysen, S.M. Haile, *Chem. Mater.* 14 (2002) 3889.
  27. A.S. Bondarenko, W.H. Zhou, H.J.M. Bouwmeester, *J. Power Sources* 194 (2009) 843.
  28. V.G. Ponomareva, G.V. Lavrova, *Solid State Ionics* 106 (1998) 137.
  29. V.G. Ponomareva, G.V. Lavrova, L.G. Simonova, *Inorg. Mater.* 34 (1998) 1136.
  30. V.G. Ponomareva, E.S. Shutova, *Solid State Ionics* 178 (2007) 729.
  31. H. Shigeoka, J. Otomo, C.J. Wen, M. Ogura, H. Takahashi, *J. Electrochem. Soc.* 151 (2004) J76.





## 5 The effect of humidification on the electrochemical performance of Pt/KH(PO<sub>3</sub>H) electrodes for solid acid-based fuel cells

### *Abstract*

*AC impedance spectroscopy was used to investigate the effect of humidification on the performance of porous Pt/KH(PO<sub>3</sub>H) electrodes deposited on the solid acid electrolyte composite KH(PO<sub>3</sub>H)-SiO<sub>2</sub>. Measurements were conducted, at 142 °C and under humidified conditions, in both oxidizing and reducing atmospheres, in which the pO<sub>2</sub> and pH<sub>2</sub> were respectively fixed at 0.2 atm. In the experimental pH<sub>2</sub>O range 0.05-0.6 atm, the conductivity of the composite electrolyte, obtained by dispersing 10 wt% of nano-sized SiO<sub>2</sub> particles (14 nm) in KH(PO<sub>3</sub>H), was found to increase with pH<sub>2</sub>O over more than one order of magnitude, irrespective of maintaining oxidizing or reducing conditions. Under similar conditions no evidence of such a conductivity enhancement was found in the phase pure substances, i.e., neither in KH(PO<sub>3</sub>H) nor in SiO<sub>2</sub>. The observations are interpreted to reflect contributions to the conductivity due to fast protonic transport along KH(PO<sub>3</sub>H)/SiO<sub>2</sub> interfaces. Deconvolution of the impedance spectra revealed that under both oxidizing and reducing conditions the electrode reaction is*

*comprised of three rate-determining processes; all three processes strongly depend on  $pH_2O$ . The total electrode conductivity was found to increase upon increasing the  $pH_2O$  from 0.05 to 0.6 atm about half an order of magnitude when measurements were conducted at  $pH_2 = 0.2$  atm, and almost 2 orders of magnitude when at  $pO_2 = 0.2$  atm. More research is needed to improve the Pt/KH( $PO_3H$ ) composite electrode performance and to elucidate the origins of the involved processes.*

## **5.1 Introduction**

Fuel cells are attractive alternatives to traditional power sources because they efficiently and continuously convert chemical fuels, such as H<sub>2</sub> and CH<sub>4</sub>, into electrical energy without harmful emissions. To date the polymer electrolyte fuel cell (PEFC) is one of the promising candidates for both stationary and transportation applications. Herein, hydrated perfluorosulfonic acid membranes, such as Nafion<sup>®</sup>, act as the electrolyte below 100 °C. However, complicated fuel processing and water management are required for the PEFC fuel cells, whilst CO poisoning at these low operating temperatures is one of the problems associated with the use of Pt-based electrodes [1, 2]. Electrolytes operating in the temperature range 100 - 300 °C could mitigate these problems [3-7].

Several groups have reported the potential of proton-conducting oxoacid-based electrolytes, such as CsH<sub>2</sub>PO<sub>4</sub> and CsHSO<sub>4</sub>, operating in the range 160 - 250 °C [3, 7, 8]. However, sulfate and selenate solid acids suffer from stability problems under hydrogen atmospheres [9, 10]. Furthermore, due to progressive dehydration the proton conductivity of the solid acids may lower when these are operated under dry conditions as observed, for example, in CsH<sub>2</sub>PO<sub>4</sub> [11]. As a consequence these still need to be operated under humidified conditions ( $p_{\text{H}_2\text{O}} > 0.3$  atm), although humidification is less severe than required for the polymer electrolytes [3, 7, 12]. Recently, we have reported high proton conductivity in the solid acid KH(PO<sub>3</sub>H), showing a superprotonic phase transition temperature,  $T_s$ , of 132 °C. The material shows good stability performance under both oxidizing and reducing conditions [13]. The composite electrolyte KH(PO<sub>3</sub>H)-SiO<sub>2</sub> is found to exhibit a stable long-term proton conductivity of  $2.2 \cdot 10^{-3}$  S cm<sup>-1</sup> at 140 °C under relatively low humidification conditions ( $p_{\text{H}_2\text{O}} > 0.03$  atm) [14]. The dispersion of fumed silica in KH(PO<sub>3</sub>H) greatly improves mechanical strength of the solid acid electrolyte.

In this study, electrochemical impedance spectroscopy is used to characterize the performance of porous Pt/KH(PO<sub>3</sub>H) electrodes on the composite electrolyte KH(PO<sub>3</sub>H)-SiO<sub>2</sub>. The measurements are conducted at open circuit conditions under controlled oxygen/steam and hydrogen/steam atmospheres. It is recognized that different parameters may influence the electrode kinetics, including microstructure, operating temperature, extent of catalyst dispersion, porosity, humidity, bias potential, etc. Much to our surprise, however, detailed reports in literature with regard to the electrode kinetics encountered in solid acid based fuel cells are scarcely available. An additional motivation to conduct this exploratory study was the difficulty experienced in our laboratory in fabricating electrodes for the KH(PO<sub>3</sub>H)/SiO<sub>2</sub>-based fuel cell showing fast electrode kinetics.

## 5.2 Experimental

### 5.2.1 Preparation of electrolyte/electrode assembly

KH(PO<sub>3</sub>H)-SiO<sub>2</sub> composites were prepared using a wet impregnation method. Fumed silica powder with a particle size ~ 14 nm (Aldrich) was suspended in an aqueous solution of KH(PO<sub>3</sub>H) under ultrasonification to destroy possible SiO<sub>2</sub> agglomerates. Water was removed by slow evaporation under rigorous stirring of the suspensions. The samples obtained were dried in an oven for one day at 100 °C, and subsequently ball-milled to obtain fine powders. The weight fraction of SiO<sub>2</sub> in the KH(PO<sub>3</sub>H)/SiO<sub>2</sub> composites was 10 wt%.

Electrolyte discs with diameter of 14 mm and thickness of 4.5 mm were obtained by uniaxial pressing of KH(PO<sub>3</sub>H)-SiO<sub>2</sub> powder, followed by isostatic pressing at 400 MPa for 5 min. A small groove was made around the disc at half thickness for positioning the Pt wire reference electrode. Pt paste was used to

improve the electrical contact between the electrolyte and the reference electrode ring.

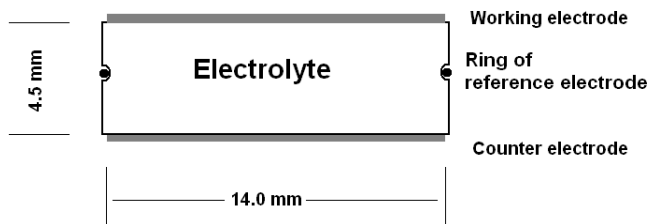


**Figure 5.1** Schematics of the three-electrode electrochemical cell. The reference electrode is placed in the groove in the middle part of the electrolyte.

The electrodes were prepared by brushing an electrode catalyst slurry on carbon paper (Toray™ TGPH090). The slurry consisted of Pt (nominally 50%, on carbon black, Alfa Aesar # 43989),  $\text{KH}(\text{PO}_3\text{H})$  and ethanol, which was treated by ultrasonication for 1 h to obtain a homogeneous mixture. After painting, the electrodes were dried at 100 °C for 24 h. The amount of Pt loading was  $\sim 1.3 \text{ mg cm}^{-2}$ . Similar porous Pt/ $\text{KH}(\text{PO}_3\text{H})$  electrodes were attached to both sides of the electrolyte disc, as illustrated in Figure 5.1. The three-electrode set-up was chosen to characterize the electrode performance as a function of overpotential. Due to time limitations, only measurements at open circuit conditions were completed.

### **5.2.2 Impedance measurements**

Impedance measurements were carried out in the frequency range from 0.01 Hz to 40 KHz in a single-gas environment using a PGstat20 Autolab Potentiostat (ECO-Chemie) with integrated frequency response analyser. An excitation voltage with an amplitude of 10 mV was used to ensure that the measurements were performed in the linear regime. Measurements were

conducted at open circuit conditions. Data analysis was carried out using complex nonlinear least squares fitting routines [15, 16]. The impedance data were checked on validity using a Kramers-Kronig transformation test program [17].

Impedance measurements were conducted, at 142 °C, under humidified conditions and in both oxidizing and reducing atmospheres, in which the  $pO_2$  and  $pH_2$  were respectively fixed at 0.2 atm, whilst using nitrogen ( $pH_2O \leq 5 \times 10^{-6}$  atm) as the balance gas. The overall flow rate was 25 ml min<sup>-1</sup>. The gas streams were humidified by passing them through constant temperature water baths using a Controlled Evaporation Mixer (CEM, Bronkhorst, The Netherlands). The measurements were conducted in the  $pH_2O$  range 0.05-0.6 atm. The compositions of the gas streams and CEM set point temperatures are listed in Table 5.1. The humidification setup is schematically presented in Figure 5.2.

**Table 5.1** Experimental conditions and CEM set point temperature.

$pH_2O$ (atm)	O <sub>2</sub> or H <sub>2</sub> (ml min <sup>-1</sup> )	H <sub>2</sub> O (g h <sup>-1</sup> )	N <sub>2</sub> (ml min <sup>-1</sup> )	Set point temperature (°C)
0.05	5.0	0.060	18.75	33.1
0.1	5.0	0.121	17.5	46.0
0.2	5.0	0.241	15.0	60.3
0.3	5.0	0.362	12.5	69.4
0.4	5.0	0.482	10.0	76.1
0.6	5.0	0.738	5.0	85.8

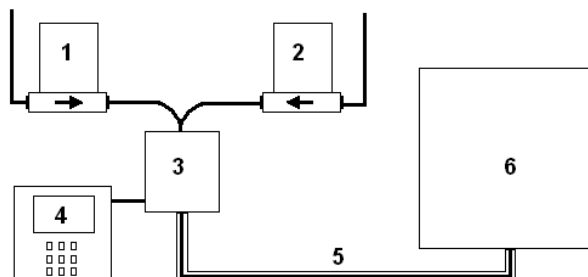


**Figure 5.2** Schematic drawing of the humidification setup: 1. liquid mass flow controller, 2. gas mass flow controller, 3. Controlled Evaporation Mixer (CEM), 4. evaporation temperature controller, 5. tubing with heating jacket, and 6. furnace.

## 5.3 Results

### 5.3.1 Electrode microstructure

The SEM microstructure of the Pt/KH(PO<sub>3</sub>H) electrode is shown in Figure 5.3. The thickness of the electrode catalyst layer is estimated around 40  $\mu\text{m}$ . The magnified SEM picture (Figure 5.3b) shows that the catalyst and solid acid are uniformly distributed. No evidence is found of significant agglomeration of KH(PO<sub>3</sub>H) particles.

### 5.3.2 Impedance spectroscopy

Impedance spectra were recorded both under oxidizing ( $p\text{O}_2 = 0.2 \text{ atm}$ ) and reducing ( $p\text{H}_2 = 0.2 \text{ atm}$ ) conditions, as a function of  $p\text{H}_2\text{O}$ . Corresponding spectra are shown in Figures 5.4a and b, respectively. Along with an obvious change in the appearance of the spectra, the high frequency cut-off value,  $R_{\text{cut-off}}$ , is found to decrease with increasing  $p\text{H}_2\text{O}$ .



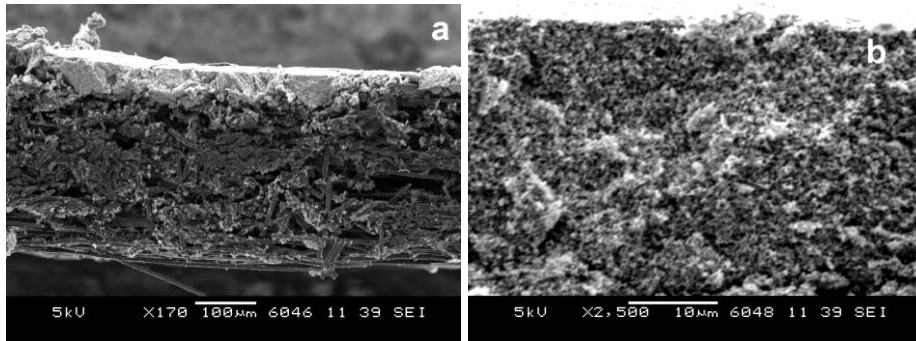


**Figure 5.3** SEM micrographs showing the microstructure of the Pt/KH(PO<sub>3</sub>H) electrode: a) cross sectional view of the electrode, and b) magnification of the catalyst layer.

## 5.4 Discussion

### 5.4.1 Analysis of impedance spectra

The electrode reactions in both oxidizing and reducing environments were found to comprise three processes. A typical deconvolution of the impedance spectrum is shown in Figure 5.5a. All spectra were analyzed using the equivalent circuit shown in Figure 5.5b. Here,  $L$  is an inductance, which is an artifact and primarily due to the leads. Variations were found within a measurement series on the same electrode. For this reason, the numerical value of  $L$  was not fixed during fitting to the experimental data [18]. The constant phase element (CPE),  $Q$ , has the admittance  $Y(\omega) = Y_0(j\omega)^n = (Y_0'j\omega)^n$ , where  $Y_0$  ( $Y_0'$ ) and  $n$  are frequency-independent parameters,  $j$  the imaginary unit, and  $\omega$  the angular frequency. When  $n$  equals -1, 0 or 1, the CPE element behaves either as a pure inductance, resistance or capacitance. When  $n = 0.5$  the CPE element acts a Warburg diffusion impedance. Although  $Y_0$  is commonly

used, using  $Y_0'$  results in a less erratic behavior in fitting of the experimental data [19]. The relationship between both parameters is given by:  $Y_0' = (Y_0)^{1/n}$ .

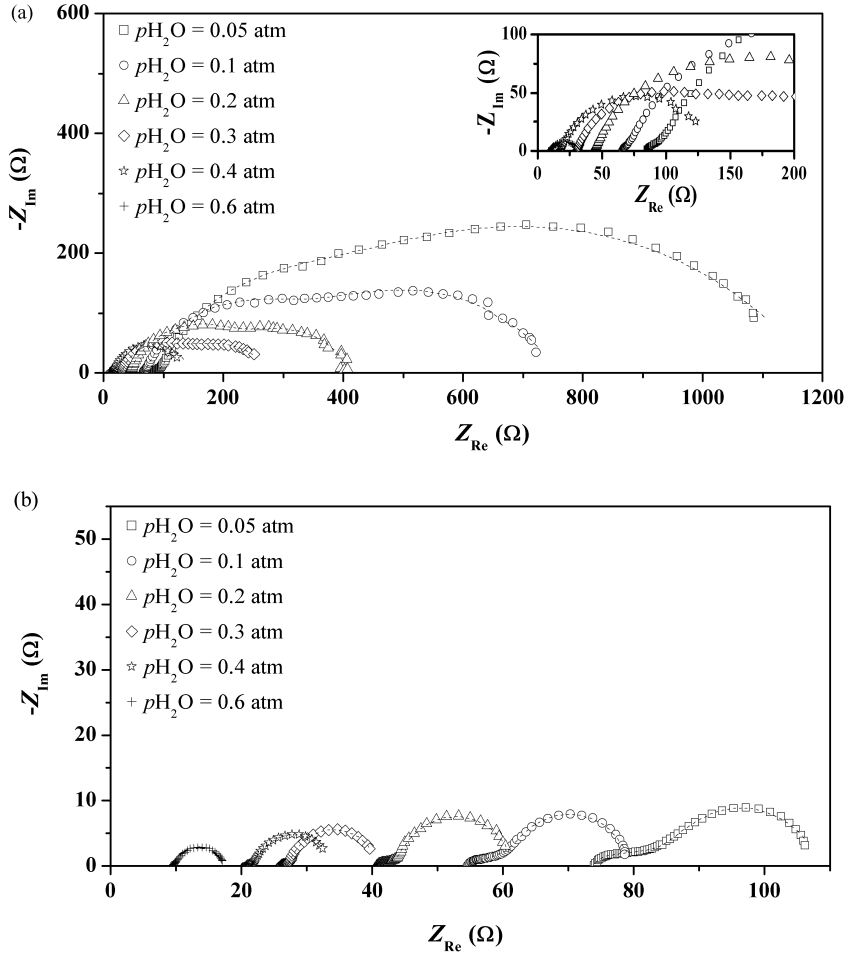


**Figure 5.4** Impedance spectra for the single chamber cell Pt/KH(PO<sub>3</sub>H)|KH(PO<sub>3</sub>H)-SiO<sub>2</sub>|Pt/KH(PO<sub>3</sub>H) at different  $p_{H_2O}$  values. Measurements were recorded, at 142 °C, and at (a)  $p_{O_2} = 0.2$  atm, and (b)  $p_{H_2} = 0.2$  atm. The inset shows a magnification of the spectra at high frequencies. Dashed lines correspond to the fits of the experimental data.

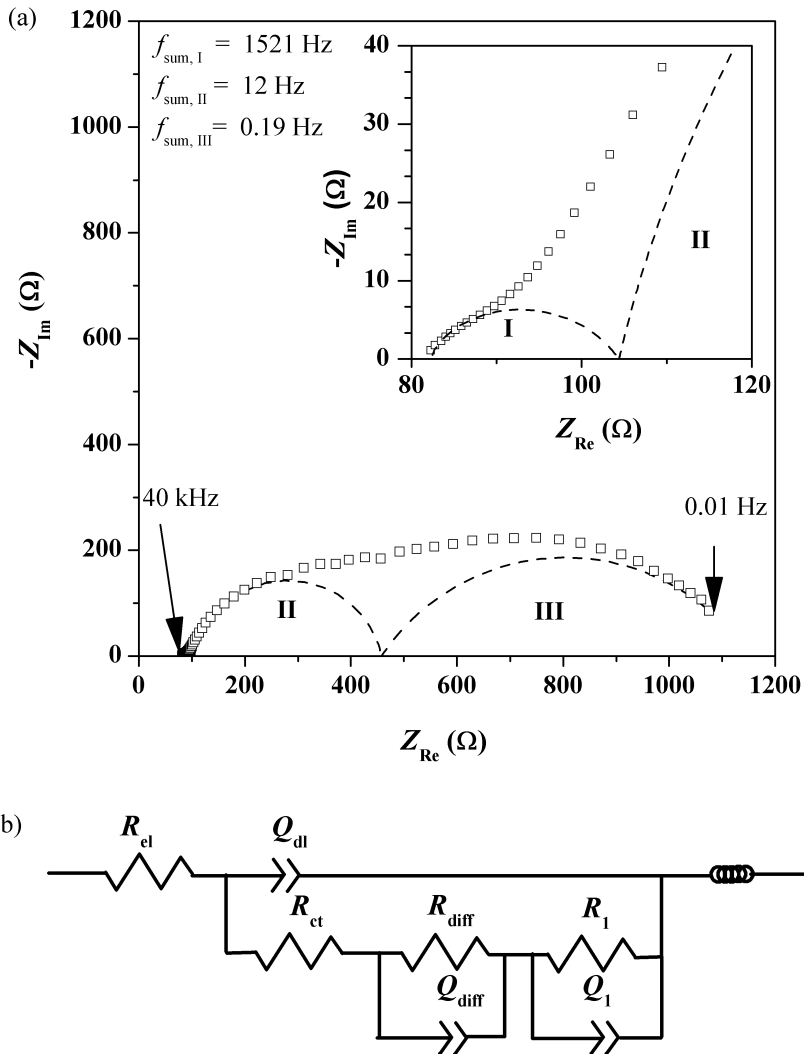


**Figure 5.5** Typical ac impedance spectrum for the single chamber cell Pt/KH(PO<sub>3</sub>H) | KH(PO<sub>3</sub>H)-SiO<sub>2</sub> | Pt/KH(PO<sub>3</sub>H). The spectrum was obtained at  $p_{\text{H}_2\text{O}} = 0.05 \text{ atm}$ ,  $p_{\text{O}_2} = 0.2 \text{ atm}$  and  $142 \text{ }^\circ\text{C}$ , and recorded at frequencies between 40 kHz and 0.01 Hz. Also shown is the equivalent circuit used in fitting of the experimental impedance spectra.

The CPE element, labeled as  $Q_{di}$  in Figure 5.5, corresponds to the double layer capacitance at the electrode/catalyst interface. The lower branch of the equivalent circuit refers to charge transfer and diffusion.  $R_{ct}$  denotes the charge transfer resistance.  $R_{diff}$  and  $Q_{diff}$  refer to the diffusion resistance and capacitance, respectively. From fitting, the  $n$  value of  $Q_{diff}$  was found to be in the range of 0.4-0.6 when measurements were conducted under oxidizing conditions ( $pO_2 = 0.2$  atm) and in the range of 0.6 - 0.7 when these were conducted under reducing conditions ( $pO_2 = 0.2$  atm). These values are reasonably close to 0.5 expected for a pure diffusion impedance (Warburg impedance) [18]. The origin of the additional parallel ( $Q_1R_1$ ) subcircuit is yet unknown. Fitting results of  $Q_1$  yielded  $n > 0.9$ , indicating almost ideal capacitive behavior.

#### **5.4.2 Electrolyte resistance**

The high frequency cut-off resistance ( $R_{cut-off}$ ) in the impedance spectra is determined by the electrolyte resistance,  $R_{el}$ . We expected the conductivity of the solid acid composite electrolyte  $KH(PO_3H)-SiO_2$  to be independent of  $pH_2O$ . However, the impedance spectra in Figure 5.4a and b clearly show that the proton conductivity of the composite electrolyte, at 142 °C, is strongly influenced by the level of humidification. At  $pO_2 = 0.2$  atm, the conductivity of the electrolyte ( $1/R_{el}$ ) increases from 8 mS cm<sup>-2</sup> to 74 mS cm<sup>-2</sup> upon increasing  $pH_2O$  from 0.05 to 0.6 atm. Similar results are found under reducing conditions ( $pH_2 = 0.2$  atm), as shown in Figure 5.4a. In both environments, the conductivities show a similar power law dependence with an exponent of 0.6 below and of 1.8 above  $pH_2O = 0.3$  atm, as demonstrated in Figure 5.6a. The change in slope suggests a change in the predominant contribution to the conductivity beyond a  $pH_2O$  of ~0.3 atm.

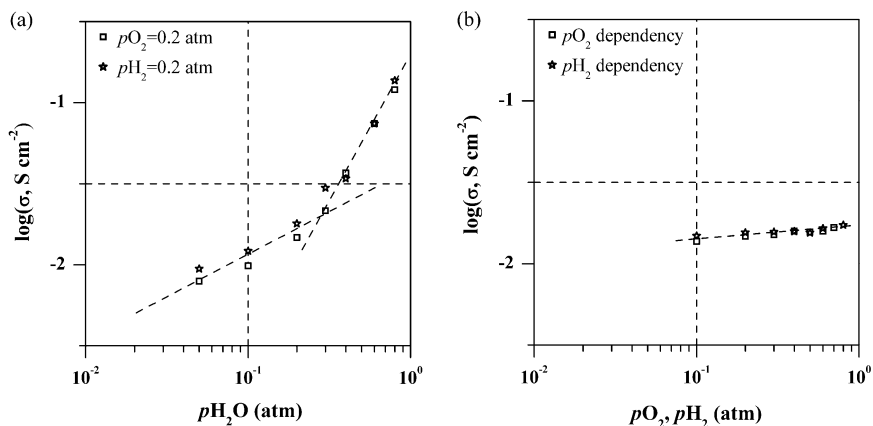


**Figure 5.6** Proton conductivity of KH(PO<sub>3</sub>H)-SiO<sub>2</sub> composite electrolyte (a) as a function of p<sub>H<sub>2</sub>O</sub> at p<sub>O<sub>2</sub></sub> = 0.2 atm (squares) and p<sub>H<sub>2</sub></sub> = 0.2 atm (stars), and (b) as a function of p<sub>O<sub>2</sub></sub> (squares) and p<sub>H<sub>2</sub></sub> (stars) at p<sub>H<sub>2</sub>O</sub> = 0.2 atm. Conductivity data was recorded at 142 °C.

Whilst the proton conductivity of KH(PO<sub>3</sub>H)-SiO<sub>2</sub>, at 142 °C, is enhanced upon humidification, no such enhancement was found for both constituents in their pure forms. Experimental data showing the effect of humidity on the proton conductivity of KH(PO<sub>3</sub>H) and silica are presented in the appendix of this chapter. It is found that the proton conductivity of pure KH(PO<sub>3</sub>H) does not vary with p<sub>H<sub>2</sub>O</sub> under conditions similar to the above (see Figure A5.1) and discussion below, whilst that of pure silica (pressed sample) under humidified conditions is comparatively poor and found to be of the order of 10<sup>-6</sup> S cm<sup>-1</sup> (see Figure A5.2).

A possible reason for the increase of proton conductivity of KH(PO<sub>3</sub>H)-SiO<sub>2</sub> with increasing humidification is the presence of fast proton transport along KH(PO<sub>3</sub>H)/SiO<sub>2</sub> interfaces. It is conceived that proton conduction is facilitated by proton hopping between sites at the silica surface [20]. Surface Si-O<sup>-</sup> and Si-OH groups, but also bridging siloxane (-Si-O-Si-) groups could act as possible sites for protonation [21]. Adsorbed water molecules could act as a bridge to

mediate proton shuttle between the solid acid and the silica surface. The change in slope above  $p\text{H}_2\text{O} = 0.3$  atm in Figure 5.6a may be associated with condensation of  $\text{H}_2\text{O}$  into mesopores of the porous electrode. Clearly, a systematic study is needed here for clarification of the observed phenomena.

No significant change in the conductivity of  $\text{KH}(\text{PO}_3\text{H})\text{-SiO}_2$  occurs when, at a  $p\text{H}_2\text{O}$  of 0.2 atm, either  $p\text{O}_2$  or  $p\text{H}_2$  is varied, as shown in Figure 5.6 b. The results confirm that the composite electrolyte can be used in both reducing and oxidizing environments.

Proton transport in the solid acids is facilitated by rapid reorientations of tetrahedral  $\text{XO}_4$  ( $\text{X} = \text{S}, \text{Se}, \text{P}$ ) oxy-anions, which is associated with the dynamic disordering of the hydrogen-bond  $-\text{O}---\text{H}---\text{O}-$  network [22, 23] above the superprotonic transition temperature, in combination with a high rate of proton transfer between adjacent tetrahedra in the disordered structure (Grotthuss mechanism) [24]. Unlike polymer electrolytes, proton conduction in the oxyanion solid acids does not rely on the migration of hydronium ions. Water molecules are claimed not to facilitate proton conduction in the oxyanion solid acids [25, 26]. Data of the proton conductivity of pure  $\text{KH}(\text{PO}_3\text{H})$  measured under nitrogen as a function of  $p\text{H}_2\text{O}$  are presented in the appendix of this chapter. At  $142^\circ\text{C}$ , *i.e.* above the superprotonic phase transition temperature, no change in the conductivity is apparent upon varying the  $p\text{H}_2\text{O}$  in the range 0 - 0.4 atm (See Figure A5.1). The conductivity under humid conditions thus resembles that measured under dry conditions. These results would essentially confirm that no water molecules are required, and are thus in support of an anhydrous mechanism for proton transport in  $\text{KH}(\text{PO}_3\text{H})$ . However, at  $100^\circ\text{C}$ , which is well below the superprotonic transition temperature of  $\text{KH}(\text{PO}_3\text{H})$ , the conductivity of the low-temperature ‘non-conducting’ monoclinic phase is surprisingly found to increase profoundly with  $p\text{H}_2\text{O}$  (See Figure A5.1). At  $p\text{H}_2\text{O} = 0.2$  atm, the conductivity is found almost 3 orders of magnitude higher

than that measured under ‘dry’ conditions ( $p_{\text{H}_2\text{O}} \sim 5 \times 10^{-6}$  atm), approaching the proton conductivity of  $\text{KH}(\text{PO}_3\text{H})$  in the superprotonic state. The observations are reminiscent of the mechanism of proton conduction in materials such as  $\alpha\text{-Zr}(\text{HPO}_4) \cdot \text{H}_2\text{O}$  (usually referred to as  $\alpha\text{-ZrP}$ ), where proton transport is dominated by surface transport, highly dependent on hydration, increasing 2 orders of magnitude as the relative humidity is increased from 5 to 90% [27]. Chemisorbed water assisting in proton conduction was also observed below the superprotonic phase transition temperature in cesium dihydrogen phosphate,  $\text{CsH}_2\text{PO}_4$ , by Otomo *et al.* [11]. As in the present study, the authors found that humidity did not affect the proton conductivity of the solid acid in its superprotonic state. Whether a surface hydration mechanism is active, enhancing the proton conductivity in the low-temperature phase of  $\text{KH}(\text{PO}_3\text{H})$ , and related solid acids, awaits further research.

### 5.4.3 Electrode impedance

Figure 5.7 show that both under hydrogen ( $p_{\text{H}_2} = 0.2$  atm) and oxygen ( $p_{\text{O}_2} = 0.2$  atm) atmospheres, the individual resistances  $R_{\text{ct}}$ ,  $R_{\text{diff}}$  and  $R_1$  all exhibit a strong dependence of  $p_{\text{H}_2\text{O}}$ . Figure 5.8 shows the corresponding values for the two parameters,  $Y_0'$  and  $n$ , of the CPE-elements obtained from fitting of the spectra. The results make clear that water has a pronounced influence on the electrode kinetics. The presence of fast, water-assisted diffusion of protons along the surface of the solid acid may contribute to an overall lowering of the electrode impedance. Such transport would explain the observed faster charge transfer and diffusion kinetics at higher  $p_{\text{H}_2\text{O}}$ , enhancing the triple-phase boundary (TPB) area at the electrode-gas phase-electrolyte boundaries. Due to time limitations, no additional experiments were conducted to investigate the overpotential dependence of the electrode impedances in different environments,

which might further aid the assignment of each of the three individual rate processes. Also, varying the flow rate of gas streams and microstructure of the electrodes might be a useful tool for further experimentation towards a more comprehensive understanding of the electrochemical reactions occurring at each of the electrodes.

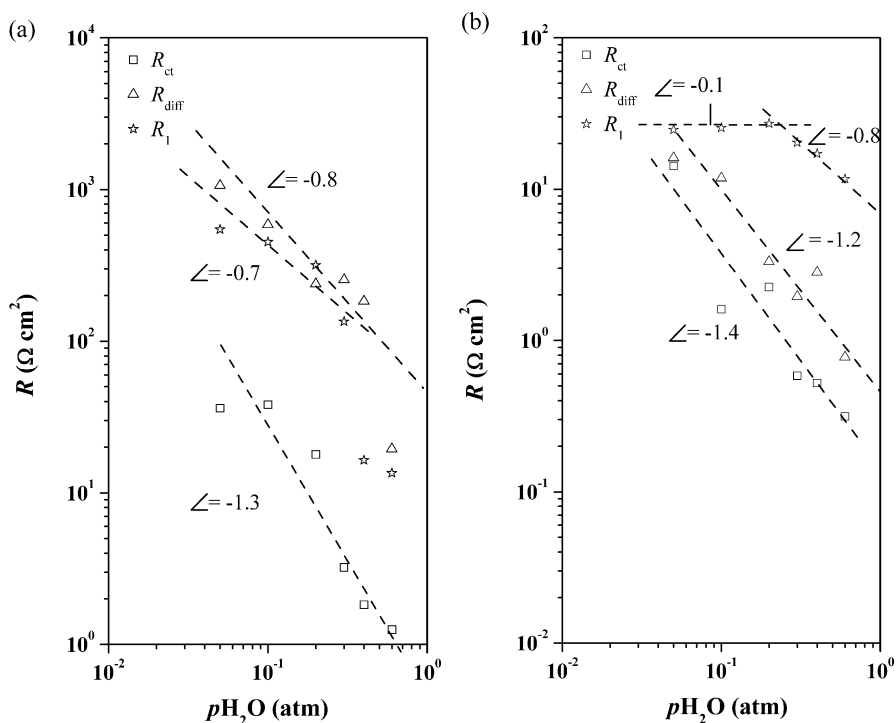


**Figure 5.7**  $p_{H_2O}$  dependencies of electrode resistances. The measurements were conducted at (a)  $p_{O_2} = 0.2$  atm and (b)  $p_{H_2} = 0.2$  atm. The slopes of trend lines are indicated. The labeling is in accordance with the equivalent circuit shown in Figure 5.5b.



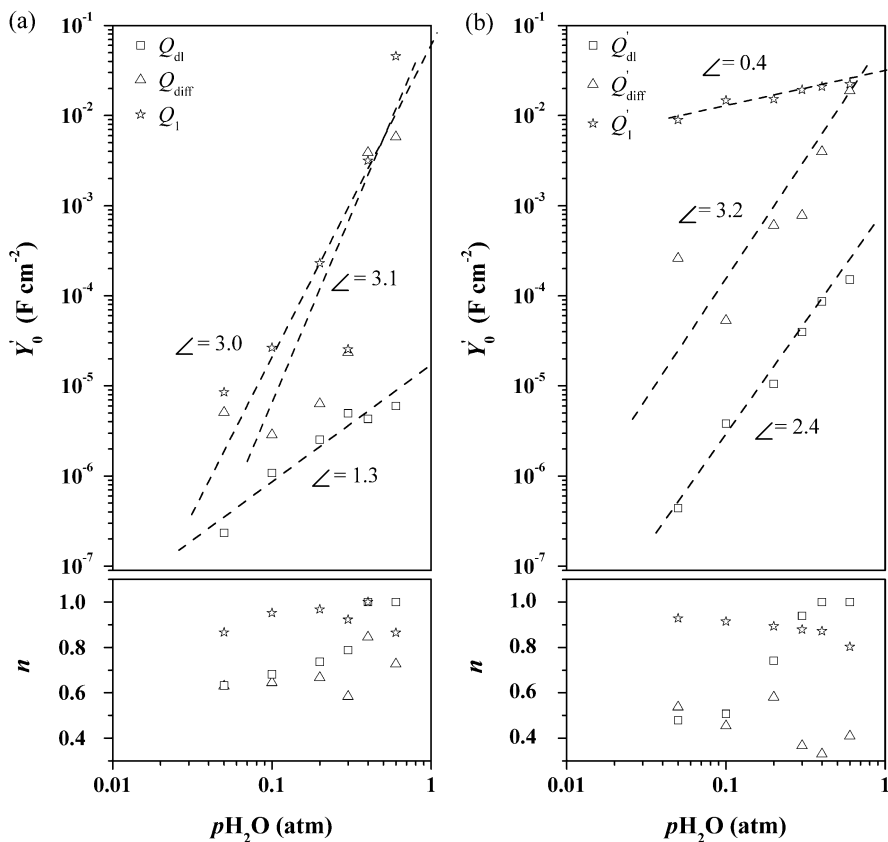


**Figure 5.8**  $p\text{H}_2\text{O}$  dependencies of parameters  $Y'_0$  (upper figure) and  $n$  (lower figure), characterizing the CPE-elements. The measurements were conducted at (a)  $p\text{O}_2 = 0.2$  atm, and (b)  $p\text{H}_2 = 0.2$  atm. The slopes of trend lines are indicated. The labeling is in accordance with the equivalent circuit shown in Figure 5.5b.

The total electrode conductivity,  $\sigma_t$ , which is simply the inverse of the sum of  $R_{\text{ct}}$ ,  $R_{\text{diff}}$  and  $R_1$ , is plotted as a function of  $p\text{H}_2\text{O}$  in Figure 5.9. Upon increasing the  $p\text{H}_2\text{O}$  from 0.05 to 0.6 atm,  $\sigma_t$  is found to increase about half an order of magnitude when measurements are conducted at  $p\text{H}_2 = 0.2$  atm, and almost 2 orders of magnitude when at  $p\text{O}_2 = 0.2$  atm. The results demonstrate that (at

zero bias conditions) major polarization is expected to occur under oxidizing conditions, involving the processes at the oxygen reduction electrode.

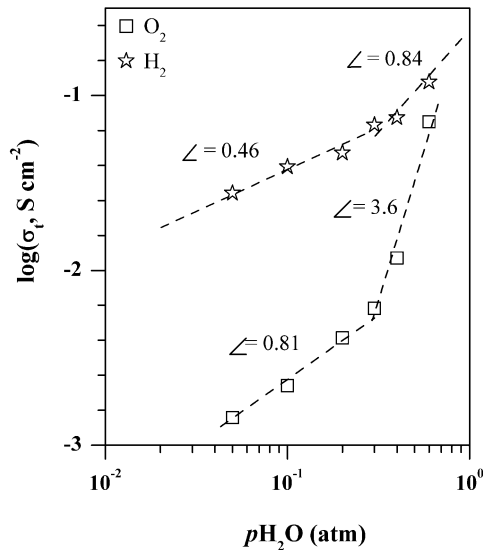


**Figure 5.9** Total electrode conductivities (142 °C) as a function of  $p_{\text{H}_2\text{O}}$  measured at  $p_{\text{O}_2} = 0.2 \text{ atm}$  (squares) and  $p_{\text{H}_2} = 0.2 \text{ atm}$  (stars).

## 5.5 Conclusions

AC impedance spectroscopy was used to gain insight into the effect of humidification on the electrochemical performance of Pt/KH(PO<sub>3</sub>H) electrodes on the composite electrolyte KH(PO<sub>3</sub>H)-SiO<sub>2</sub> under both oxidizing ( $p_{\text{O}_2} = 0.2 \text{ atm}$ ) and reducing ( $p_{\text{H}_2} = 0.2 \text{ atm}$ ) conditions. The electrode reactions were found to comprise three processes, which rates strongly depend on the extent of humidification. The total electrode conductivity was found to increase about half an order of magnitude when measurements were conducted under reducing conditions, and almost 2 orders of magnitude under oxidizing conditions, upon

increasing the  $p\text{H}_2\text{O}$  from 0.05 to 0.6 atm. More research is, however, needed to improve the Pt/KH(PO<sub>3</sub>H) composite electrode performances and to elucidate the origins of the involved processes.

Though this study was initiated to study the performance of the electrodes, humidification was found to have a pronounced effect on the conductivity of KH(PO<sub>3</sub>H)-SiO<sub>2</sub> used as the electrolyte. In the experimental  $p\text{H}_2\text{O}$  range 0.05 - 0.6 atm, the proton conductivity was found to increase with  $p\text{H}_2\text{O}$  over more than one order of magnitude, irrespective of maintaining oxidizing or reducing conditions, whilst no evidence of such a conductivity enhancement in humid environments was found in the pure substances, neither in KH(PO<sub>3</sub>H) nor in SiO<sub>2</sub>. The conductivity enhancement observed in KH(PO<sub>3</sub>H)-SiO<sub>2</sub> under humidified conditions is tentatively interpreted to reflect contributions from fast protonic transport along KH(PO<sub>3</sub>H)-SiO<sub>2</sub> interfaces by chemisorbed water molecules.

## References

1. S. Litster, G. McLean, J. Power Sources 130 (2004) 61.
2. N. Yousfi-Steiner, P. Mocoteguy, D. Candusso, D. Hissel, A. Hernandez, A. Aslanides, J. Power Sources 183 (2008) 260.
3. D.A. Boysen, T. Uda, C.R.I. Chisholm, S.M. Haile, Science 303 (2004) 68.
4. S.M. Haile, T. Uda, D. Boysen, C.R.I. Chisholm, Abstracts of Papers of ACS 231 (2006).
5. T. Uda, D.A. Boysen, C.R.I. Chisholm, S.M. Haile, Electrochem. Solid-State Lett. 9 (2006) A261.
6. T. Uda, S.M. Haile, Electrochem. Solid-State Lett. 8 (2005) A245.
7. S.M. Haile, D.A. Boysen, C.R.I. Chisholm, R.B. Merle, Nature 410 (2001) 910.
8. G.V. Lavrova, M.V. Russkikh, V.G. Ponomareva, N.F. Uvarov, Russ. J. Electrochem. 41 (2005) 485.
9. R.B. Merle, C.R.I. Chisholm, D.A. Boysen, S.M. Haile, Energy & Fuels 17 (2002) 210.
10. B. Yang, A.M. Kannan, A. Manthiram, Mater. Res. Bull. 38 (2003) 691.
11. J. Otomo, T. Tamaki, S. Nishida, S.Q. Wang, M. Ogura, T. Kobayashi, C.J. Wen, H. Nagamoto, H. Takahashi, J. Appl. Electrochem. 35 (2005) 865.
12. J. Otomo, S. Nishida, H. Takahashi, H. Nagamoto, J. Electroanal. Chem. 615 (2008) 84.
13. A.S. Bondarenko, W.H. Zhou, H.J.M. Bouwmeester, J. Power Sources 194 (2009) 843.
14. W.H. Zhou, A.S. Bondarenko, B.A. Boukamp, H.J.M. Bouwmeester, Solid State Ionics 179 (2008) 380.
15. B.A. Boukamp, Solid State Ionics 20 (1986) 31.
16. B.A. Boukamp, Solid State Ionics 18-9 (1986) 136.

17. B.A. Boukamp, *J. Electrochem. Soc.* 142 (1995) 1885.
18. S. Primdahl, Nickel/yttria-stabilised zirconia cermet anodes for solid oxide fuel cells, *Inorganic Materials Science*, University of Twente, Enschede (1999).
19. M.M.G. Cuenca, Novel Anode Materials For Solid Oxide Fuel Cells, *Inorganic Materials Science*, University of Twente, Enschede (2002).
20. M. Nogami, Y. Abe, *Phys. Rev. B* 55(1997) 10218.
21. G.K. Lockwood, S.H. Garofalini, *J. Chem. Phys* 131 (2009) 074703.
22. N.M. Plakida, *JETP Lett.* 41 (1985) 114.
23. A.V. Belushkin, R.L. McGreevy, P. Zetterstrom, L.A. Shivalov, *Physica B:* 241-243 (1997) 323.
24. C.R.I. Chisholm, S.M. Haile, *Solid State Ionics* 136 (2000) 229.
25. W. Muech, K.D. Kreuer, U. Traub, J. Maier, *Solid State Ionics* 77 (1995) 10.
26. C.R.I. Chisholm, R.B. Merle, D.A. Boysen, S.M. Haile, *Chem. Mater.* 14 (2002) 3889.
27. M. Casciola, D. Bianchi, *Solid State Ionics* 17 (1985) 287.

## **Appendix**

### **The effect of humidification on the proton conductivity of KH(PO<sub>3</sub>H) and SiO<sub>2</sub>**

The humidification effect on the conductivities of KH(PO<sub>3</sub>H) and SiO<sub>2</sub>, in their pure forms, were measured by sputtering gold electrodes on both sides of disc specimens. KH(PO<sub>3</sub>H) was prepared by slow evaporation of an aqueous solution of KOH (Merck, 99.5%) and phosphorous acid (99%, Aldrich). The powder was dried in an oven in air at ~105 °C during 20 h prior to measurements. Fumed silica (Aldrich, 14 nm) was used as received. Powders of both substances were isostatically pressed into discs of 1 mm thickness, 10 mm diameter at 400 MPa for 5 min.

Electrochemical impedance spectroscopy was used for measurement of the conductivity. Different from that described in the experimental section (Section 5.2.2.), the measurements were conducted under nitrogen (flow rate 25 ml min<sup>-1</sup>;  $p_{\text{H}_2\text{O}} \sim 5 \times 10^{-6}$  atm) in the frequency range 0.5 MHz to 100 Hz below the superprotonic phase transition ( $T_s$ ), and from 50 kHz to 100 Hz above  $T_s$ . The conductivity of KH(PO<sub>3</sub>H) was measured in the  $p_{\text{H}_2\text{O}}$  range 0.05 - 0.4 atm. The conductivity of silica was measured at  $p_{\text{H}_2\text{O}} = 0.1$  atm.

Conductivity data of polycrystalline KH(PO<sub>3</sub>H) and fumed silica are presented in Figures A5.1 and A5.2, respectively. As seen from Figure A5.1, the conductivity of KH(PO<sub>3</sub>H) measured at 142 °C, *i.e.*, above the superprotonic transition temperature,  $T_s$ , shows no obvious change upon variation of  $p_{\text{H}_2\text{O}}$ . On the other hand, the conductivity at 100 °C, *i.e.*, below  $T_s$ , is significantly enhanced upon humidification. At a  $p_{\text{H}_2\text{O}}$  of 0.4 atm, the conductivity is almost 3 orders of magnitude higher than the conductivity measured under 'dry' conditions ( $p_{\text{H}_2\text{O}} \sim 5 \times 10^{-6}$  atm), approaching values measured when KH(PO<sub>3</sub>H)

is in the superprotonic state. The conductivity enhancement observed below  $T_s$  is tentatively interpreted to reflect contributions from surface transport by chemisorbed water. As seen from Figure A5.2, the pressed sample of fumed silica shows a comparatively low conductivity of the order of  $10^{-6} \text{ S cm}^{-1}$  under humidified conditions ( $p\text{H}_2\text{O} = 0.1 \text{ atm}$ ) at all temperatures.

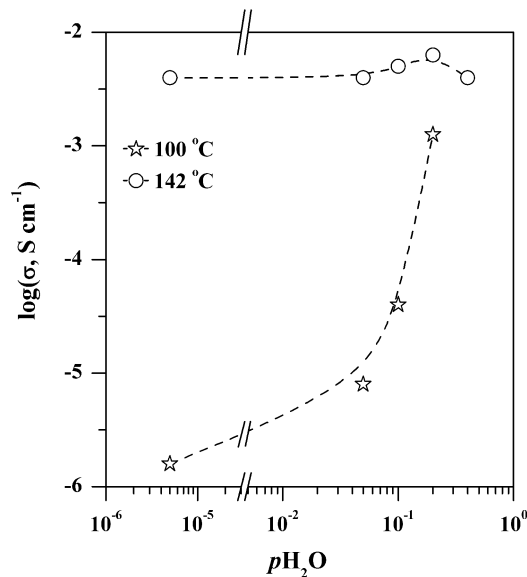


**Figure A5.1.** Effect of humidification on the proton conductivity of  $\text{KH}(\text{PO}_3\text{H})$  measured both below and above the superprotonic phase transition temperature.

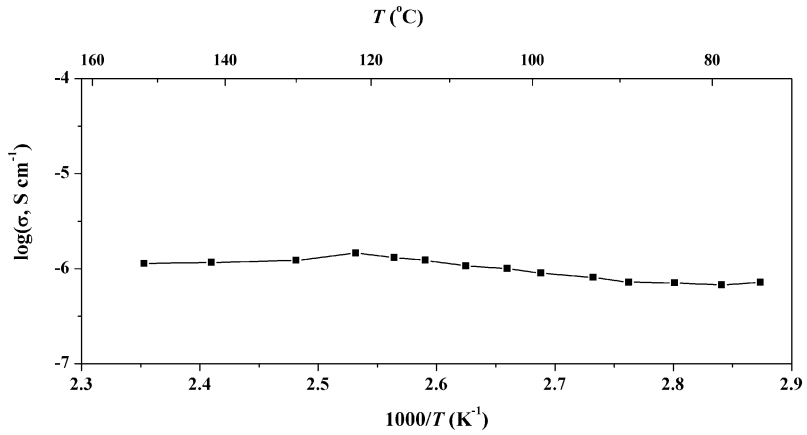


**Figure A5.2** Arrhenius plot of the proton conductivity of a pressed disc of fumed SiO<sub>2</sub> measured under nitrogen at  $p\text{H}_2\text{O} = 0.1$  atm.





## 6 Outlook and recommendations

### ***Abstract***

*In this chapter, some initial exploratory research towards is described towards a fuel cell incorporating the composite solid acid,  $KH(PO_3H)-SiO_2$ , as the electrolyte. Suggestions are provided for continued research.*

The research described in this thesis has been mainly focused on developing proton-conducting solid acid electrolytes for potential use in a micro solid acid-based fuel cell [1].

Extensive research activities have been made and are being made in many R&D laboratories to develop proton-conducting membranes operating above 100 °C. Though operation at elevated temperature tends to stress chemical and mechanical issues, the higher operating temperature will decisively simplify heat management and improve overall system efficiency [2-4]. Most importantly, this temperature increase will enhance the electrode tolerance to fuel impurities such as CO. As seen from Figure 6.1, the proton conductivity of

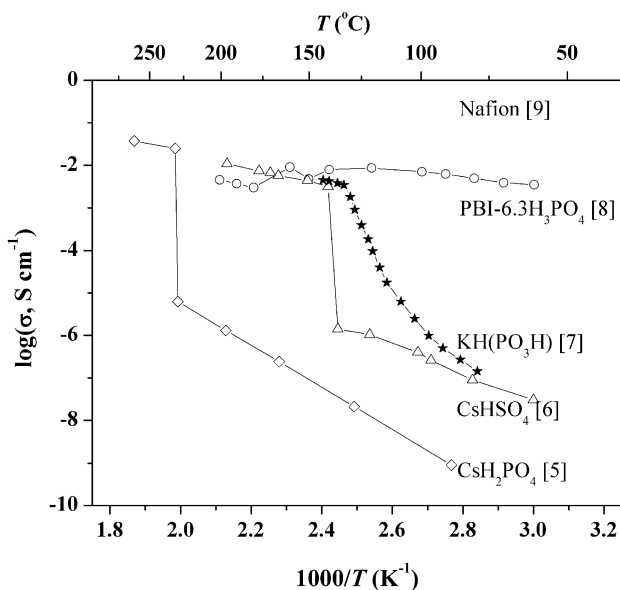


**Figure 6.1** The conductivities of selected low-temperature proton-conducting electrolytes, shown in Arrhenius form. Sources are indicated in the figure.

KH(PO<sub>3</sub>H) developed in this thesis work is comparable to that of other proton-conducting electrolytes. Unlike the solid acids CsHSO<sub>4</sub> and CsH<sub>2</sub>PO<sub>4</sub>, KH(PO<sub>3</sub>H) shows intrinsic thermodynamic stability under both oxidizing and reducing conditions [10]. Obvious drawbacks of the use of solid acids, however, are (i) their low conductivity at low temperature, which affects the cold start of a fuel cell, and (ii) their water solubility, which implies that direct contact with water, for example, during an accidental shutdown, should be avoided. It may be noted that these disadvantages also hold for widely investigated phosphoric acid-doped polybenzimidazole (PBI) membranes [11].

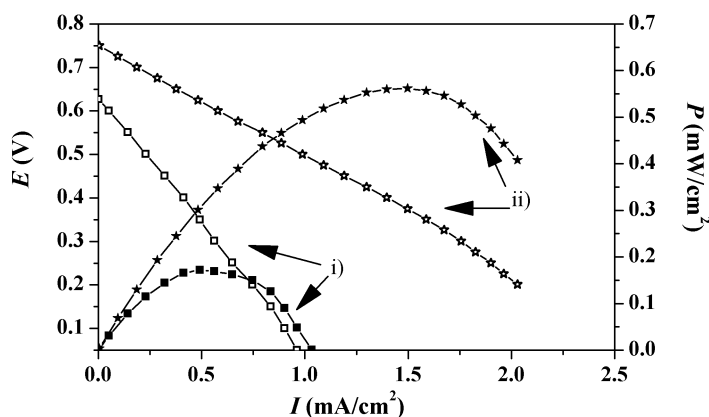


**Figure 6.2** Cell voltage and power density of a fuel cell incorporating KH(PO<sub>3</sub>H)-SiO<sub>2</sub> ( $\omega = 0.2$ ;  $d_p \approx 14$  nm) as the electrolyte. The cell was operated at 140 °C under humidified hydrogen ( $p_{H_2} = 0.05$  atm) and oxygen streams ( $p_{O_2} = 0.21$  atm), flowing at 40 sccm at the anode and the cathode, respectively; i)  $p_{H_2O} = 0.03$  atm, ii)  $p_{H_2O} = 0.3$  atm. Nitrogen was used as balance gas. The electrolyte thickness was 0.6 mm. The Pt catalyst loading of both electrodes was  $\sim 1$  mg cm<sup>-2</sup>.

Preliminary investigations were conducted with a fuel cell prepared with a 0.6-mm-thick KH(PO<sub>3</sub>H)-SiO<sub>2</sub> ( $\omega = 0.2$ ,  $d_p \approx 14$  nm) electrolyte, using

Pt/KH(PO<sub>3</sub>H) for both electrodes. The electrolyte disc ( $\varnothing = 16$  mm) was obtained by uniaxial pressing at room temperature at 400 MPa. The Pt/KH(PO<sub>3</sub>H) electrodes were prepared by brushing a mixture of Pt, C and KH(PO<sub>3</sub>H) on carbon paper, as described in detail in Chapter 5. Subsequently, the electrodes were pressed onto the electrolyte disc at a pressure of 100 MPa. The epoxy resin (Araldit®, Huntsman Advanced Materials B.V.) sealed cell was operated under H<sub>2</sub>/O<sub>2</sub> configuration at 140 °C, in which both the anode and cathode gas streams were humidified to either  $p_{\text{H}_2\text{O}} = 0.03$  atm or  $p_{\text{H}_2\text{O}} = 0.3$  atm. The corresponding cell voltage and power density versus current density plots are shown in Figure 6.2.

As seen from Figure 6.2, the open cell voltages (OCV's), 0.65 V and 0.75 V for measurements at  $p_{\text{H}_2\text{O}} = 0.03$  atm and at  $p_{\text{H}_2\text{O}} = 0.3$  atm, respectively, are distinctly lower than the corresponding theoretical OCV's (Nernst potential), 1.16 V, indicating that significant hydrogen crossover (from the anode to the cathode) occurred. Supplementary measurements of the hydrogen permeability of KH(PO<sub>3</sub>H)-SiO<sub>2</sub> ( $\omega = 0.2$ ,  $d_p \approx 14$  nm) electrolyte discs demonstrated that crossover could be reduced to negligible values by hot-pressing the electrolyte disc at 140 °C and 700 MPa in air for 10 min. Clearly, more attention needs to be given to appropriate methods for consolidation and densification of the solid acid-based electrolyte. An additional concern in this respect is the thermal and associated mechanical behavior of the dual-phase electrolyte. As such it cannot be excluded that differences in the thermal expansion of both constituents and the thermal phase behavior of the solid acid contributes to the formation of possible defects and micro-cracks in the solid electrolyte during heating and/or thermal cycling.

Also seen from Figure 6.2 is that the peak power densities increased from 0.15 mW cm<sup>-2</sup> at 0.5 mA cm<sup>-2</sup> to 0.55 mW cm<sup>-2</sup> at 1.5 mA cm<sup>-2</sup> upon increasing humidification of the gas streams from  $p_{\text{H}_2\text{O}} = 0.03$  atm to  $p_{\text{H}_2\text{O}} = 0.3$  atm,

respectively. Obvious reasons for the poor fuel cell performance, which remains unsatisfactory even at the highest level of humidification, are the poor conductivity of the electrolyte in the form of a pressed disc and the poor electrochemical activity exhibited by the electrodes.

A number of low cost methods are readily available for the deposition of thin electrolyte films in order to minimize Ohmic polarization, such as colloidal dip-coating, tape casting, spin coating, spray coating, etc. In Chapter 3, colloidal dip-coating was exploited to prepare thin films of  $\text{KH}(\text{PO}_3\text{H})\text{-SiO}_2$  ( $\omega = 0.2$ ,  $d_p \approx 14$  nm) in the  $\mu\text{m}$  range. The procedure described in Chapter 3 may need some optimization to obtain films with, for example, a minimum number of defects and/or a high relative density. In Chapter 4, it was found that the conductivity of the  $\text{SiO}_2$ -dispersion-strengthened composite electrolyte increases profoundly, at  $142^\circ\text{C}$ , upon increasing  $p\text{H}_2\text{O}$  over more than one order of magnitude in the  $p\text{H}_2\text{O}$  range 0.05-0.6 atm. The role of  $\text{H}_2\text{O}$  and that of microporosity of the nano-particulate  $\text{SiO}_2$  dispersant on proton conductivity of the composite electrolyte  $\text{KH}(\text{PO}_3\text{H})\text{-SiO}_2$  certainly deserves more attention. Alternatively other, for example, polymeric dispersants could be used to improve the morphological, rheological and mechanical properties of the solid acid.

Finally, as emphasized in Chapter 5, further attention needs to be given to improve the performance of the  $\text{Pt}/\text{KH}(\text{PO}_3\text{H})$  electrodes and to elucidate the origins of the involved kinetic processes. The values measured for the charge transfer resistance and other mass transport resistances (see Figure 5.7) need a ten- to hundred-fold decrease to become competitive with state-of-the-art PEMFC's [12]. Especially, the roles of thickness, morphology, level of humidification of the gas streams and catalyst loading on the electrode

properties need to be investigated, and individual variables tailored to achieve a high performance.

## **References**

1. S. Unnikrishnan, Micromachined Dense Palladium Electrodes for Thin-film Solid Acid Fuel Cells, PhD thesis University of Twente, Enschede (2009).
2. S.M. Haile, Fuel Cells Bull. 2004 (2004) 3.
3. S. Martwiset, High temperature proton conducting materials and fluorescent-labeled polymers for sensor applications, PhD thesis, University of Massachusetts, Amherst (2009).
4. Q.F. Li, R.H. He, J.O. Jensen, N.J. Bjerrum, Chem. Mater. 15 (2003) 4896.
5. A.I. Baranov, V.P. Khiznichenko, L.A. Shuvalov, Ferroelectrics 100 (1989) 135.
6. V.G. Ponomareva, G.V. Lavrova, Solid State Ionics 145 (2001) 197.
7. W. Zhou, A.S. Bondarenko, B.A. Boukamp, H.J.M. Bouwmeester, Solid State Ionics 179 (2008) 380.
8. Y. Ma, The fundamental studies of polybenzimidazole/phosphoric acid polymer electrolyte for fuel cells, PhD Thesis Case Western Reserve University (2004).
9. Q. Li, C. Xiao, W. Li, H. Zhang, F. Chen, P. Fang, M. Pan, Colloid. Polym. Sci. 288 (2010) 1369.
- 10 Chapter 2 of this thesis.
11. Q.F. Li, J.O. Jensen, R.F. Savinell, N.J. Bjerrum, Prog. Polym. Sci. 34 (2009) 449.
12. For example, see D. Malevich, E. Halliop, B.A. Peppley, J.G. Pharoah, K. Karan, J. Electrochem. Soc. 156 (2009) B216.





## Reverse microemulsion synthesis of the superprotonic conductor $\text{CsHSO}_4$

### ***Abstract***

*A reverse water-in-oil (w/o) microemulsion technique has been used to prepare nanoparticles of the water-soluble solid acid superprotonic conductor  $\text{CsHSO}_4$ . The synthesis is based on the controlled evaporation of water from the surfactant-stabilized reverse micelles, inducing crystallization of the solid acid within the confines of the micelles. Ultra small particles within the range 0.6 – 2.5 nm are obtained as confirmed by dynamic light scattering and atomic force microscopy. X-ray powder diffraction shows that despite their small size the nanoparticles of  $\text{CsHSO}_4$  are crystalline in nature. Impedance measurements, at 150°C, of nanocrystalline powder compacts show that the proton conductivity drops profoundly with decreasing particle size (almost three orders of magnitude within the specified range of particle size), which seems linked to the concomitant increase in the density of blocking grain boundaries limiting overall proton transport.*

## A.1 Introduction

Among superprotonic solids acids, CsHSO<sub>4</sub> has received almost the most attention [1-6]. Since its discovery in 1982 by Baranov and co-workers [7], many studies have been focused on its structural and transport properties. The anhydrous proton transport in the solid acids, eliminating the need for continuous humidification of reactant gases, renders these solids highly attractive alternatives to perfluorinated sulfonated polymers (*e.g.* Nafion<sup>®</sup>) for fuel-cell applications [1, 2, 8-10]. The higher operating temperature (up to 250 °C) thereby increases tolerance of commonly used precious metal electrocatalysts such as Pd and Pt to carbon monoxide.

Major aim of the project, in which this PhD work has been carried out, is to assemble a solid acid-based fuel cell using micromachining techniques. One of the challenges concerns the development of a technology for deposition of a micro- or submicrometer thin film of the solid acid to reduce Ohmic polarisation losses. The solid acid may be dispersed in a polymer or ceramics to improve mechanical robustness. It is immediately obvious that nanoscale particles are needed for fabrication of such composite thin films. The present work aims at preparation of nanoparticles of a solid acid. The choice of available techniques for their preparation, however, is limited due to water solubility and low thermal stability (250 °C) of the solid acids. Because of prior experience in our laboratory [11], a microemulsion-based synthesis route was chosen. To our knowledge, this is the first time that a solid acid, using CsHSO<sub>4</sub> as the prototype for this class of compounds, has been prepared using a reverse microemulsion (water-in-oil) synthesis technique. Results from characterisation of CsHSO<sub>4</sub> nanoparticles and measurements of the proton conductivity of nanocrystalline powder compacts are discussed.

## A.2 Experimental

### A.2.1 Powder synthesis

Nanosized powders of CsHSO<sub>4</sub> were prepared by a reverse microemulsion-mediated technique. The microemulsions consisted of surfactant Brij<sup>®</sup> 30 (C<sub>12</sub>H<sub>25</sub>(OCH<sub>2</sub>-CH<sub>2</sub>)<sub>4</sub>OH, Mw = 362 g/mol, HLB = 9, Acros Chemicals), *n*-decane (Fluka > 95%) and an aqueous phase containing 0.5 mol<sup>-1</sup> CsHSO<sub>4</sub> in deionized water. Preliminary experiments identified the region where a single-phase water-in-oil microemulsion forms. Corresponding results are shown in Figure A.1, where the single-phase region is labeled with I. All microemulsions

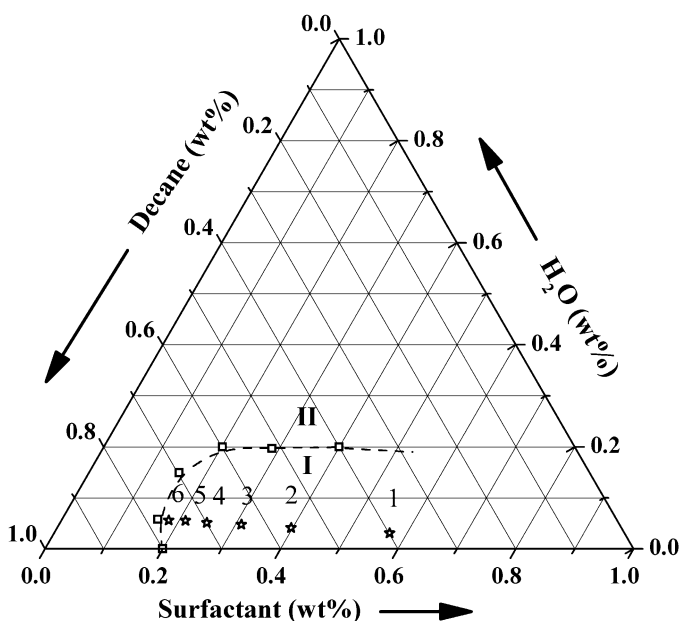


**Figure A.1** Phase diagram for the water/Brij 30/*n*-decane system at 20°C, showing single and inhomogeneous phase regions, designated I and II, respectively. The stars denote the compositions of micellar solutions M1-M6 (see also Table A.1).

within this region remained stable for at least 12 h. Microemulsions with different compositions were prepared in this region as illustrated in Figure A.1. Corresponding water-to-surfactant weight fractions,  $R_w$ , used in the preparation are indicated in Table A.1. The oil-to-water weight fraction,  $R_o$ , was fixed at 11.9. The microemulsions were obtained by adding the surfactant to mixtures of the oil and aqueous phases under constant stirring at room temperature. The water was removed, at 40 °C, by evaporation in a rotating evaporator. The white precipitate was isolated by a centrifuge (7000 RPM) for 20 min, washed several times in decane and diethyl ether, and dried in air at 105 °C.

Polycrystalline powders of  $\text{CsHSO}_4$  several micrometers in size were prepared by slow evaporation of aqueous solutions of cesium carbonate (Fluka, > 99%) in sulphuric acid (95%, Aldrich), in which the mole ratio  $\text{Cs}:\text{H}_2\text{SO}_4$  was fixed at 1:1. The powders were dried in an oven at ~105 °C during 20 h, ground in an agate mortar and stored in a desiccator, due to hygroscopicity of the pure salt.

### A.2.2 Characterization

The reverse microemulsions as prepared were characterized by dynamic light scattering (Nano ZS, Malvern Instruments). The powders obtained from synthesis were characterized by several techniques. Powder X-ray diffraction (XRD) was performed using the Philips XRD PW3020 (50kV, 35 mA,  $\text{Cu K}_{\alpha-1}$ ) diffractometer at room temperature, and processed with the Philips X'Pert program for phase identification. Thermal analysis was carried out using differential scanning calorimeter (METTLER TOLEDO DSC823) at a scan rate of  $3 \text{ K min}^{-1}$  in flowing  $\text{N}_2$  ( $40 \text{ ml min}^{-1}$ ). Particle size distribution measurements were performed by dynamic light scattering (DLS, Zetasizer Nano, Malvern) and atomic force microscopy (AFM, Dimension D3100). For DLS measurements, powders were redispersed in decane. For AFM

measurements, a drop of the prepared solution (sample CHS4) was applied on a mica substrate.

For proton conductivity measurements, powders were isostatically pressed at 400 MPa into discs of 10 mm diameter and 0.5 mm thickness. Gold electrodes were sputtered (JOEL JFC-1300) on both sides of the discs. Complex impedance spectroscopy was conducted using a PGstat20 Autolab Potentiostat with integrated frequency response analyzer (ECO-Chemie). Measurements were performed in flowing, dry nitrogen ( $20 \text{ ml min}^{-1}$ ) either at  $150^\circ\text{C}$  or as a function of temperature. The temperature was incremented stepwise, with a heating/cooling rate of  $0.8 \text{ K min}^{-1}$ , at which the sample was equilibrated for at least 30 min prior to data acquisition. Impedance spectra were collected over the frequency range 0.5 MHz to 100 Hz below and from 50 kHz to 10 Hz above the superprotonic phase transition temperature. An excitation voltage with an amplitude of 10 mV was used to ensure that measurements were performed in the linear regime. No bias voltage was applied. Spectra were analyzed after passing a Kramer-Kronig transformation test [12]. Data analysis was carried out using complex nonlinear least squares fitting routines [13].

## **A.3 Results and discussion**

### **A.3.1 Microemulsion synthesis**

Microemulsions constitute a controlled environment for chemical reactions and precipitations, in which the surfactant-stabilized droplets act as individual nanosized reactors [14, 15]. The micelles collide via random Brownian motion and exchange their solubilized contents. This exchange process is fundamental in microemulsion-based syntheses, allowing different reactants in two separate microemulsions to react upon mixing. Rather, in this work, a single w/o

microemulsion is used, where the aqueous phase contains the solute CsHSO<sub>4</sub>. Crystallization of the solid acid within the spatial confines of the reverse micelles is induced by evaporation of water. Table A.1 lists micelle sizes ( $d_{50}$ ) of microemulsions M1-M6 in the water/Brij<sup>®</sup> 30/decane system, obtained along the line corresponding to an oil-to-water weight fraction  $R_o = 11.9$  (see also Figure A. 1). Corresponding size distributions obtained from dynamic light scattering are shown in Figure A.2. In general, a number of parameters may influence the micelle size. Besides temperature, these include the type of oil phase, surfactant (and co-surfactant), concentration of salt in the aqueous phase, the oil-to-water ( $R_o$ ) and the water-to-surfactant ( $R_w$ ) ratios. No systematic study was made in this work to investigate this in detail, as this has been discussed extensively in literature, for example, see Ref. [16] As seen from Table A.1,  $R_w$  has a clear influence on the apparent micelle size and, hence, on the amount of

**Table A.1** Water-to-surfactant weight fraction,  $R_w$ , oil-to-water weight fraction,  $R_o$ , and micelle size ( $d_{50}$ ) of microemulsions M1-M6. Also indicated are calculated and measured ( $d_{50}$ ) particle sizes of CsHSO<sub>4</sub> nanopowders (after re-dispersion in decane). Corresponding size distributions from dynamic light scattering are shown in Figures A2 and A3.

Sample	$R_w$	$R_o$	Micelle size (nm)	Measured particle size (nm)	Calculated particle size (nm)
M1	0.05	11.9	2.6	0.6	0.8
M2	0.10	11.9	3.6	0.8	1.2
M3	0.15	11.9	4.3	1.2	1.4
M4	0.20	11.9	5.3	1.5	1.7
M5	0.25	11.9	7.4	1.6	2.4
M6	0.30	11.9	8.7	2.5	2.8

encapsulated aqueous phase. No significant changes in micelle sizes were observed within 24 h at room temperature.

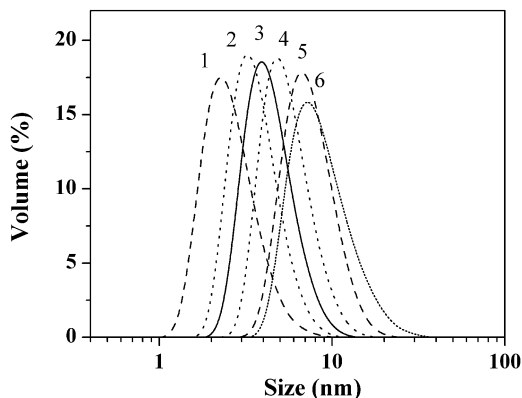


**Figure A.2** Size distributions of the micelles in microemulsions M1-M6 having a different  $R_w$  (See Table A1).

The monodisperse size distributions of  $\text{CsHSO}_4$  nanoparticles obtained from reverse microemulsions M1-M6, after washing, drying in air at 105 °C and re-dispersion of the powder in decane, are shown in Figure A.3. The corresponding average particle sizes ( $d_{50}$ ), listed in Table A.1, closely resemble the particle sizes calculated from the volumes of the aqueous phase, 0.5 M  $\text{CsHSO}_4$ , encapsulated by the reverse micelles in each of the microemulsions. These calculations were performed assuming a spherical particle size of  $\text{CsHSO}_4$  with molar volume  $V_m = 69 \text{ cm}^3 \text{ mol}^{-1}$ . Figure A.4 shows an AFM image of nanoparticles  $\text{CsHSO}_4$  obtained from microemulsion M4. The line profile indicates a particle size of approximately 2.0 nm, which fairly agrees with the value of 1.5 nm measured by dynamic light scattering. Unfortunately, recording of scanning electron microscopy (SEM) micrographs was not possible as the focused electron beam induced evaporation.



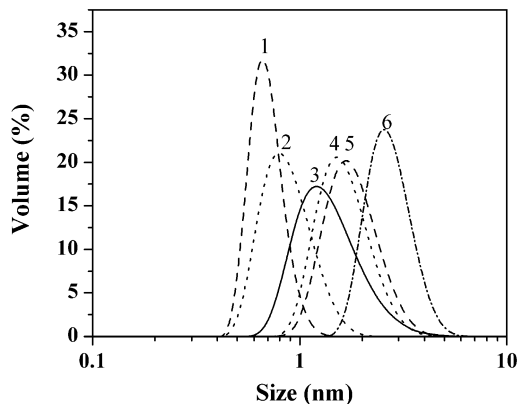


**Figure A.3** Size distributions of nanoparticles  $\text{CsHSO}_4$ . Powders obtained from reverse microemulsions M1-M6 (See Table A1) were re-dispersed in decane.

X-Ray powder patterns of the nanosized powders  $\text{CsHSO}_4$  obtained from reverse microemulsion synthesis are given in Figure A.5. These show that despite the ultra small particle sizes all prepared powders are crystalline.  $\text{CsHSO}_4$  has a complicated phase behavior. When grown at room temperature, it is known to adopt a monoclinic phase with space group  $P2_1/c$ , referred to as Phase III and believed to be metastable [17, 18]. Upon heating it irreversibly transforms between 60-100 °C to another monoclinic phase, also with space group  $P2_1/c$  and referred to as Phase II. The precise transformation temperature depends on details such as humidity, heating rate, and sample surface conditions etc [17]. Only upon heating above 141°C,  $\text{CsHSO}_4$  transforms into a superprotonic-conducting phase, referred to as Phase I, which has tetragonal symmetry [7]. The diffraction patterns obtained for nanopowders CHS3 - CHS6 (as obtained from microemulsions M3-M6) are interpreted to reflect mixed behavior of phases III [19] and II [17]. A precise interpretation is, however, complicated by the systematic absence of some reflections (see Figure A.5), which might be related to the ultra small size or due to preferred growth and/or

orientation of the nanocrystals. Analysis of the spectra obtained for samples CHS1 and CHS2 suggests the co-presence of CsHSO<sub>4</sub> and Cs<sub>2</sub>SO<sub>4</sub>, and possibly Cs<sub>3</sub>H(SO<sub>4</sub>)<sub>2</sub>. Clearly, a more systematic study is required to analyze the structures of the nanocrystals of CsHSO<sub>4</sub> obtained from reverse microemulsion synthesis. For reasons above mentioned, it cannot be excluded that in addition

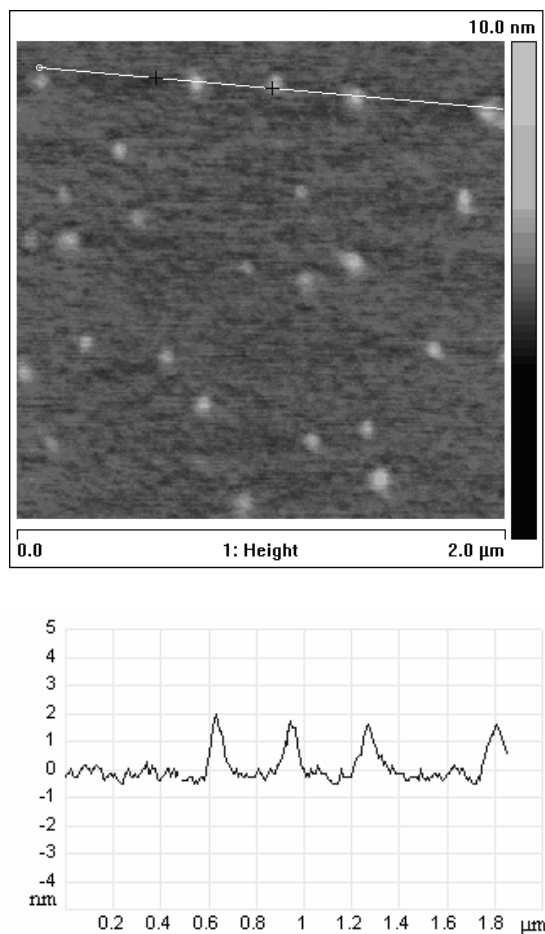


**Figure A.4** AFM image of CsHSO<sub>4</sub> nanoparticles on a mica substrate. Also shown is the AFM line profile, following the line shown in the upper figure. Nanoparticles of CsHSO<sub>4</sub> were obtained from reverse microemulsion M4.

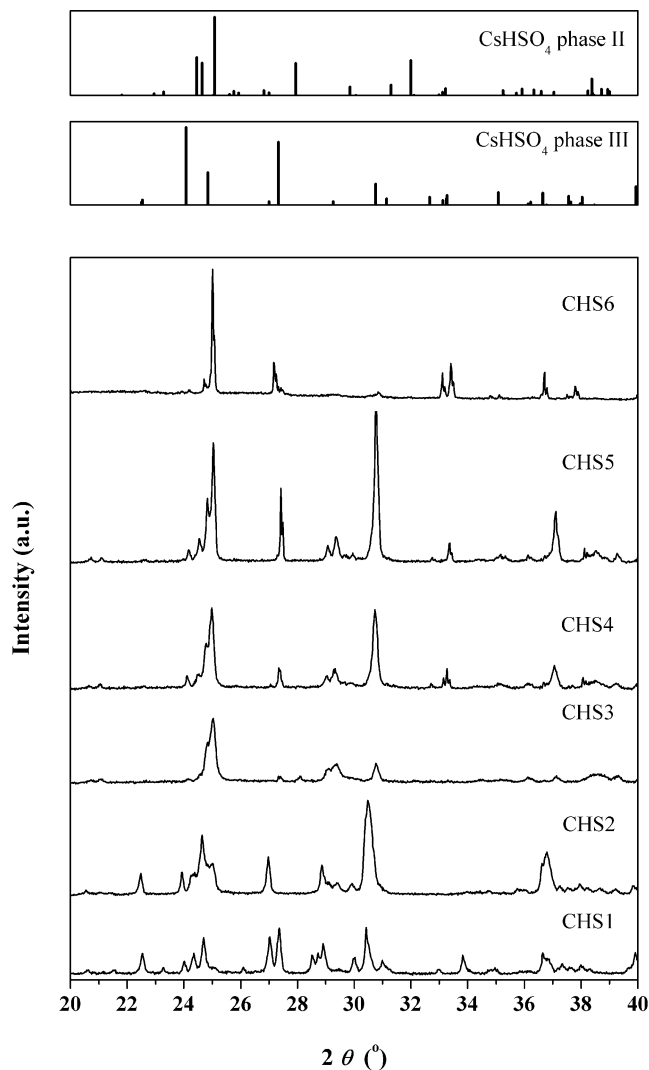


**Figure A.5** Room temperature X-ray diffraction patterns of nanopowders CsHSO<sub>4</sub>. Powders CHS1-CHS6 were obtained from reverse microemulsions M1-M6, respectively. Also shown are the theoretical diffraction patterns of phases III and II of CsHSO<sub>4</sub> calculated from crystallographic structure data given in Refs. 17 and 19.

to size and growth of the nanocrystals, drying temperature, curing time and cooling rate affect the phase behavior of nanocrystalline CsHSO<sub>4</sub>.

### A.3.2 Proton conductivity

$\text{CsHSO}_4$  is known to exhibit a first-order transition, at  $141\text{ }^\circ\text{C}$ , from the low-temperature phase (Phase II) to the high-temperature superprotonic phase (Phase I), at which the proton conductivity increases profoundly [18]. Data of differential thermal analysis from this study are presented in Figure A.6. The extrapolated onset temperatures of the superprotonic phase transition in nanopowders CHS3 – CHS6 all are in excellent agreement with the reported result from literature. Endothermic events observed at more elevated temperatures can be attributed to melting/decomposition of  $\text{CsHSO}_4$ . For samples CHS1 and CHS2, the superprotonic transition temperatures are found around  $146\text{ }^\circ\text{C}$ . This might indicate that  $\text{Cs}_3\text{H}(\text{SO}_4)_2$  has formed in the corresponding microemulsions, rather than  $\text{CsHSO}_4$ , since the superprotonic

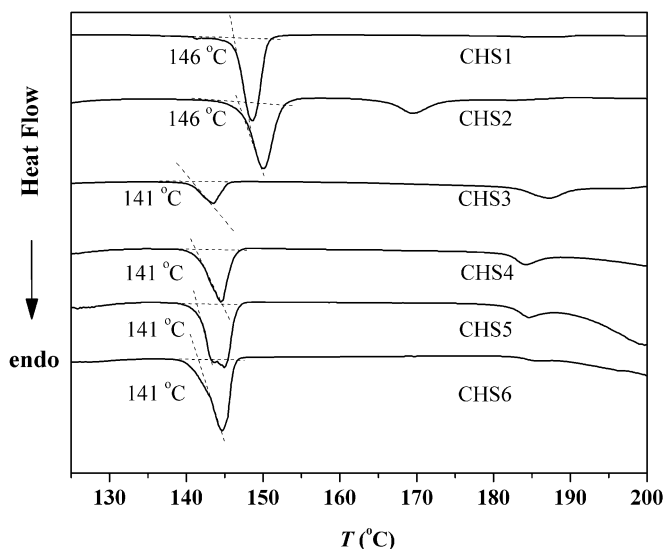


**Figure A.6** DTA curves of  $\text{CsHSO}_4$  nanopowders CHS1-CHS6, collected under flowing nitrogen at a heating rate of  $3\text{ K min}^{-1}$ . The extrapolated onset temperatures of the superprotonic phase transition are indicated.

phase transition for the former has been reported to occur at 145 °C [20]. Due to time limitations, no further consideration was given to this observation.

Figure A.7 shows the proton conductivity, at 150 °C, of nanocrystalline powder compacts of CHS1-CHS6 as a function of inverse particle size. Also included in the figure are data from conductivity measurements on a polycrystalline sample of CsHSO<sub>4</sub> with a grain size of ~10 μm, obtained from slow evaporation of an aqueous solution of stoichiometric amounts of Cs<sub>2</sub>CO<sub>3</sub> and H<sub>2</sub>SO<sub>4</sub> (see experimental section). It is seen from the figure that the proton

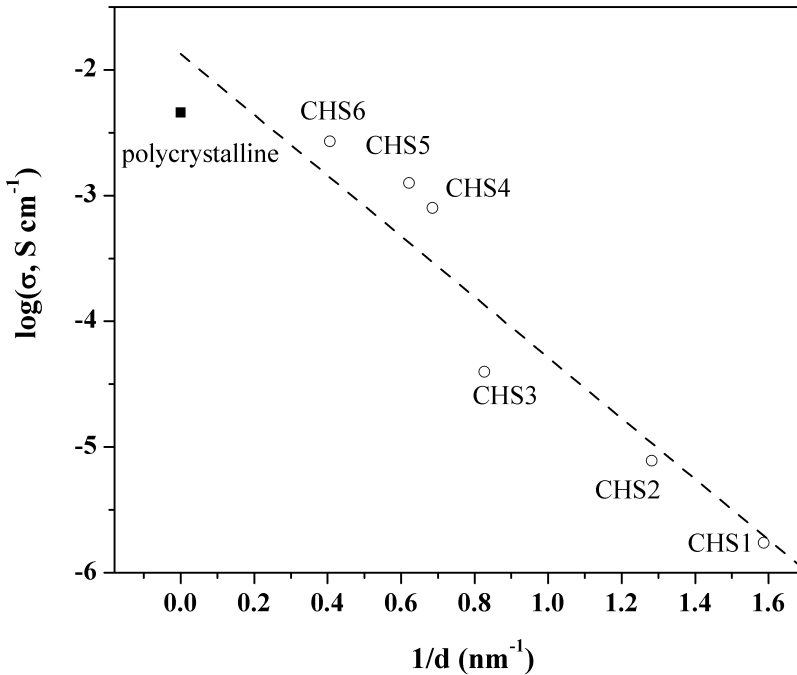


**Figure A.7** Proton conductivity of compacts of nanopowders CHS1-CHS6 as a function of inverse particle size. Also shown is the result (square symbol) obtained from measurement of a polycrystalline sample of CsHSO<sub>4</sub> with a grain size of ~10 μm. Data were collected at 150 °C under flowing nitrogen.

conductivity drops almost three orders of magnitude within the range of particle size covered experimentally, which seems linked to the concomitant increase in the density of blocking grain boundaries limiting overall proton transport. This observation clearly demonstrates that there are constraints with respect to the reduction of particle size in the fabrication of thin films of the proton-conducting electrolyte CsHSO<sub>4</sub>.

#### **A.4 Conclusions**

The results from this study demonstrate that slow evaporation of the aqueous phase of a single reverse water-in-oil (w/o) microemulsion can be successfully exploited to prepare ultra-small nanoparticles of the water-soluble solid acid CsHSO<sub>4</sub>. To the best of our knowledge, this is the first time that nanoparticles of a water-soluble salt has been prepared with nanoscale dimensions in the range 0.6 – 2.5 nm as confirmed by AFM and dynamic laser scattering measurements. X-ray powder diffraction experiments show that despite their small sizes the nanoparticles of CsHSO<sub>4</sub> are crystalline in nature. Conductivity measurements of the nanocompacts, at 150 °C, show that their proton conductivity drops profoundly with decreasing particle size (almost three orders of magnitude within the specified range of particle size), which seems linked to the concomitant increase in the density of blocking grain boundaries limiting overall proton transport. This observation puts constraints on decreasing the particle size in thin films of CsHSO<sub>4</sub>, which is widely investigated as a potential electrolyte in solid acid based fuel cells.

## **References**

1. S.M. Haile, D.A. Boysen, C.R.I. Chisholm, R.B. Merle, *Nature* 410 (2001) 910.
2. C.R.I. Chisholm, Y.H. Jang, S.M. Haile, W.A. Goddard, *Phys. Rev. B* 72 (2005).
3. N.G. Chainovskii, *Izvestiya Sibirskogo Otdeleniya Akademii Nauk Sssr Seriya Khimicheskikh Nauk* (1984) 18.
4. A.V. Belushkin, R.L. McGreevy, P. Zetterstrom, L.A. Shuvalov, *Physica B* 241 (1997) 323.
5. C.R.I. Chisholm, S.M. Haile, *Chem. Mater.* 19 (2007) 270.
6. M. Kislitsyn, S.M. Haile, *Chem. Mater.* 22 (2010) 2417.
7. A.I. Baranov, L.A. Shuvalov, N.M. Shchagina, *JETP Lett.* 36 (1982) 459.
8. A.I. Baranov, V.V. Grebenev, A.N. Khodan, V.V. Dolbinina, E.P. Efremova, *Solid State Ionics* 176 (2005) 2871.
9. T. Uda, D.A. Boysen, C.R.I. Chisholm, S.M. Haile, *Electrochem. Solid-State Lett.* 9 (2006) A261.
10. S.M. Haile, C.R.I. Chisholm, K. Sasaki, D.A. Boysen, T. Uda, *Faraday Discuss.* 134 (2007) 17.
11. F.C.M. Woudenberg, *Nanostructured oxide coatings via modified emulsion precipitation*, Ph.D. Thesis, University of Twente, the Netherlands (2001).
12. B.A. Boukamp, *J. Electrochem. Soc.* 142 (1995) 1885.
13. A.S. Bondarenko, W.H. Zhou, H.J.M. Bouwmeester, *J. Power Sources* 194 (2009) 843.
14. I. Capek, *Adv. Colloid Interface Sci.* 110 (2004) 49.
15. A.K. Ganguli, A. Ganguly, S. Vaidya, *Chem. Soc. Rev.* 39 (2010) 474.
16. A. Forgiarini, J. Esquena, C. Gonzalez, C. Solans, *Langmuir* 17 (2001) 2076.
17. C.R.I. Chisholm, S.M. Haile, *Mater. Res. Bull.* 35 (2000) 999.

18. E. Ortiz, R.A. Vargas, B.E. Mellander, *J. Phys. Condens. Matter* 18 (2006) 9561.
19. K. Itoh, T. Ukeda, T. Ozaki, E. Nakamura, *Acta Crystallogr., Sect. C: Cryst. Struct. Commun.* 46 (1990) 358.
20. A.R. Lim, J.-H. Chang, *J. Appl. Phys.* 104 (2008) 063502.





## Summary

Solid acids, such as  $\text{CsHSO}_4$  and  $\text{CsH}_2\text{PO}_4$ , are a novel class of anhydrous proton-conducting compounds that can be used as electrolyte in  $\text{H}_2/\text{O}_2$  and direct methanol fuel cells. The disordering of the hydrogen-bonded network above the so-called superprotonic phase transition results in an increase of the proton conductivity by several orders of magnitude. Unlike conventional polymer electrolytes, such as Nafion<sup>®</sup>, proton conduction in the solid acids does not rely on transport of hydronium ions.

The research described in this thesis is mainly focused on developing proton-conducting solid acid electrolytes for potential use in a micro solid acid-based fuel cell [1]. In **Chapter 1**, a brief survey is given of different classes of proton-conducting electrolytes, with special emphasis on solid acid compounds, providing a background for further reading of this thesis.

In **Chapter 2**, the ionic conductivity and thermal stability of solid acid phosphites,  $\text{MH}(\text{PO}_3\text{H})$ , are investigated. High proton conductivity occurs in  $\text{MH}(\text{PO}_3\text{H})$ , with  $\text{M} = \text{Na}^+, \text{K}^+, \text{Rb}^+, \text{Cs}^+, \text{NH}_4^+$ , above the superprotonic phase transition (120 - 190 °C), which compositions adopt a monoclinic crystal structure at room temperature, while no superprotonic phase transition is observed for orthorhombic  $\text{LiH}(\text{PO}_3\text{H})$ . In the given series, however, only  $\text{KH}(\text{PO}_3\text{H})$  and  $\text{CsH}(\text{PO}_3\text{H})$  are found to exhibit a good stability against dehydration (or melting), with superprotonic conductivities of  $4.2 \cdot 10^{-3} \text{ S cm}^{-1}$  (at 140 °C) and  $3 \cdot 10^{-3} \text{ S cm}^{-1}$  (at 160 °C), respectively. These values are comparable to that of widely investigated  $\text{CsHSO}_4$ . Unlike  $\text{CsHSO}_4$ ,  $\text{KH}(\text{PO}_3\text{H})$  shows a good stability in both oxidizing and reducing atmospheres, which is of prime importance with regard to its potential use as electrolyte in a fuel cell.

In **Chapters 3 and 4**, respectively, heterogeneous and homogeneous doping of  $\text{KH}(\text{PO}_3\text{H})$  are explored, attempting to improve its performance. As

described in **Chapter 3**, dispersion of nano-particulate SiO<sub>2</sub> in KH(PO<sub>3</sub>H) is found to lower proton conductivity of KH(PO<sub>3</sub>H) in its superprotonic state. Simultaneously, the superprotonic phase transition temperature is reduced and the conductivity jump at the superprotonic phase transition is smoothed due to significant enhancement of the low-temperature proton conductivity. The former observation is accounted for by reduced volume and blocking effects by insulating SiO<sub>2</sub> particles. The latter, i.e., the enhancement of the low-temperature conductivity, is attributed to the presence of fast conduction pathways along KH(PO<sub>3</sub>H)/SiO<sub>2</sub> interfaces. It is further demonstrated that dehydration and associated degradation of the proton conductivity, at 140 °C, can be prevented by a slight humidification of the gas streams, corresponding to a water partial pressure as low as ~0.02 atm. Under these conditions, the dispersion-strengthened electrolyte, KH(PO<sub>3</sub>H)-SiO<sub>2</sub> ( $\omega = 0.2$ ;  $d_p \approx 14$  nm), which can be fabricated as a thin film in the  $\mu\text{m}$  range by dip-coating, shows a proton conductivity of  $1.15 \cdot 10^{-3} \text{ S cm}^{-1}$ .

The results presented in **Chapter 4** indicate that the method of homogeneous doping offers a useful strategy for tuning and optimizing the properties of proton-conducting solid acids. It is found that partial substitution of Cs<sup>+</sup> or NH<sub>4</sub><sup>+</sup> substitution for K<sup>+</sup> in KH(PO<sub>3</sub>H) lowers the onset temperature of the superprotonic phase transition relative to those exhibited by the end-members in both series K<sub>1-x</sub>Cs<sub>x</sub>H(PO<sub>3</sub>H) ( $0 \leq x \leq 1$ ) and K<sub>1-x</sub>(NH<sub>4</sub>)<sub>x</sub>H(PO<sub>3</sub>H) ( $0 \leq x \leq 1$ ). This is most pronounced for K<sub>0.1</sub>(NH<sub>4</sub>)<sub>0.9</sub>H(PO<sub>3</sub>H), where the onset temperature of the superprotonic phase transition is observed as low as 67 °C, as compared to 125 °C and 127 °C observed for KH(PO<sub>3</sub>H) and (NH<sub>4</sub>)H(PO<sub>3</sub>H), respectively (albeit noted that for the given composition two superprotonic transitions are observed, besides 67 °C also one at 114 °C). The observations suggest that in the solid solutions of solid acids the hydrogen bonds are either

weakened, relative to those in the parent compounds, or broken. Contrary to  $K_{1-x}(NH_4)_xH(PO_3H)$ , isovalent substitution of  $Cs^+$  for  $K^+$  in  $KH(PO_3H)$  significantly increases its low-temperature conductivity.

In **Chapter 5**, the effect of water partial pressure,  $pH_2O$ , on the performance of porous Pt/ $KH(PO_3H)$  electrodes on  $KH(PO_3H)-SiO_2$  ( $\omega = 0.1$ ;  $d_p \approx 14$  nm) is studied by AC impedance spectroscopy. It is found that, at 142 °C, the electrode reaction is comprised of three rate-determining processes, each strongly dependent on  $pH_2O$ , though their origins remain unclear from the data of the experiments. A remarkable observation is that the proton conductivity of the composite electrolyte is improved strongly with increasing  $pH_2O$ , while no such conductivity enhancement is found in phase pure  $KH(PO_3H)$  or  $SiO_2$ . The observation is interpreted to reflect fast protonic transport along  $KH(PO_3H)/SiO_2$  interfaces, being assisted by  $H_2O$  molecules.

**Chapter 6** concludes the work presented in this thesis with an outlook on the potential application of solid acids as a fuel cell electrolyte and with suggested activities for continued research. It is concluded that (i) consolidation and thermo-mechanical behavior of the electrolyte, with an eye on possible  $H_2$  cross-over, (ii) the role of  $H_2O$  and that of microporosity of the nano-particulate  $SiO_2$  dispersant on proton conductivity of the composite electrolyte  $KH(PO_3H)-SiO_2$ , and (iii) fabrication and morphology control of catalyst electrodes, besides presenting scientific challenges, definitely deserve more attention.

Finally, in the **Appendix** of this thesis, a one-pot reverse water-in-oil (w/o) microemulsion technique is presented, enabling generic preparation of nanoparticles of water-soluble solid acids. The method has been used to prepare ultrananocrystalline  $CsHSO_4$  (0.6 – 2.5 nm).

## **Reference**

1. S. Unnikrishnan, Micromachined Dense Palladium Electrodes for Thin-film Solid Acid Fuel Cells, PhD thesis, University of Twente, Enschede (2009).

## Samenvatting

Vaste zuren, zoals  $\text{CsHSO}_4$  and  $\text{CsH}_2\text{PO}_4$ , vormen een nieuwe klasse van water vrije protonengeleidende verbindingen die gebruikt kunnen worden als elektrolyt in  $\text{H}_2/\text{O}_2$  and direct methanol brandstofcellen. De wanorde in het netwerk van waterstofbindingen boven de zogenoemde superprotonische faseovergang leidt tot een toename van de protonengeleiding van meerdere ordes van grootte. In tegenstelling tot conventionele polymerelektrolyten, zoals Nafion®, is de protonengeleiding in vaste zuren niet gebaseerd op transport van hydroniumionen.

Het onderzoek beschreven in dit proefschrift is vooral gericht op het ontwikkelen van protonengeleidende vaste zure elektrolyten voor potentieel gebruik in een op vaste zuur gebaseerde microbrandstofcel [1]. In **hoofdstuk 1** wordt een kort overzicht gegeven van verschillende klassen van protonengeleidende elektrolyten, met speciale nadruk op vaste zure verbindingen, als basis voor verdere lezing van dit proefschrift.

In **hoofdstuk 2** worden de ionengeleiding en thermische stabiliteit van vaste zure fosfieten,  $\text{MH}(\text{PO}_3\text{H})$ , onderzocht. Een hoge protonengeleiding in  $\text{MH}(\text{PO}_3\text{H})$ , met  $\text{M} = \text{Na}^+, \text{K}^+, \text{Rb}^+, \text{Cs}^+, \text{NH}_4^+$ , treedt op boven de superprotonische faseovergang (120 - 190 °C), welke samenstellingen bij kamertemperatuur een monokliene kristalstructuur bezitten. Voor orthorhombisch  $\text{LiH}(\text{PO}_3\text{H})$  wordt geen superprotonische faseovergang waargenomen. In de gegeven serie wordt echter alleen voor  $\text{KH}(\text{PO}_3\text{H})$  en  $\text{CsH}(\text{PO}_3\text{H})$  een goede stabiliteit gevonden tegen uitdroging (of smelten), waarbij superprotonische geleidingsvermogens van respectievelijk  $4,2 \cdot 10^{-3} \text{ S cm}^{-1}$  (bij 140 °C) en  $3 \cdot 10^{-3} \text{ S cm}^{-1}$  (bij 160 °C) gemeten worden. Deze waarden zijn vergelijkbaar met die het op grote schaal onderzochte  $\text{CsHSO}_4$ . In tegenstelling tot  $\text{CsHSO}_4$ , laat  $\text{KH}(\text{PO}_3\text{H})$  een goede stabiliteit zien in zowel

oxiderende als reducerende atmosfeer, hetgeen van essentieel belang is voor potentiële toepassing als elektrolyt in een brandstofcel.

In **hoofdstukken 3 en 4** worden respectievelijk heterogene en homogene dotering van  $\text{KH}(\text{PO}_3\text{H})$  bestudeerd in een poging om de performance hiervan te verbeteren. Zoals beschreven in **hoofdstuk 3** leidt dispersie van  $\text{SiO}_2$  nanodeeltjes in  $\text{KH}(\text{PO}_3\text{H})$  tot een verlaging van de protonengeleiding van  $\text{KH}(\text{PO}_3\text{H})$  in zijn superprotonische toestand. Tegelijkertijd wordt de temperatuur van de superprotonische faseovergang verlaagd en de sprong in de geleiding nabij de superprotonische faseovergang afgevlakt als gevolg van een aanzienlijke verhoging van de protonengeleiding bij lage temperatuur. Het eerste kan verklaard worden door volume-effecten en blokkering door isolerende  $\text{SiO}_2$  deeltjes. Het tweede, de toename van de geleiding bij lage temperatuur, kan toegeschreven worden aan de aanwezigheid van paden voor snelle geleiding langs  $\text{KH}(\text{PO}_3\text{H})/\text{SiO}_2$  interfaces. Verder wordt aangetoond dat dehydratatie en de daarmee samenhangende reductie van de protonengeleiding bij  $140\text{ }^\circ\text{C}$  kan worden voorkomen door een geringe bevochtiging van de gasstromen, overeenkomend met een dampdruk van water van  $\sim 0,02\text{ atm}$ . Onder deze omstandigheden toont het dispersie-versterkte elektrolyt,  $\text{KH}(\text{PO}_3\text{H})\text{-SiO}_2$  ( $\omega = 0,2$ ;  $d_p \approx 14\text{ nm}$ ), dat in de vorm van een dunne film gefabriceerd kan worden door dip-coating, een protonengeleiding van  $1,15 \cdot 10^{-3}\text{ S cm}^{-1}$ .

De resultaten weergegeven in **hoofdstuk 4** suggereren dat de methode van homogene dotering een bruikbare strategie biedt voor het afstemmen en optimaliseren van de eigenschappen van protonengeleidende vaste zuren. Het blijkt dat partiële substitutie van  $\text{Cs}^+$  of  $\text{NH}_4^+$  voor  $\text{K}^+$  in  $\text{KH}(\text{PO}_3\text{H})$  de onset-temperatuur van de superprotonische faseovergang verlaagt ten opzichte van die gevonden voor de begin- en eindsamenstellingen in beide series  $\text{K}_{1-x}\text{Cs}_x\text{H}(\text{PO}_3\text{H})$  ( $0 \leq x \leq 1$ ) and  $\text{K}_{1-x}(\text{NH}_4)_x\text{H}(\text{PO}_3\text{H})$  ( $0 \leq x \leq 1$ ). Dit is het meest uitgesproken

voor  $K_{0.1}(NH_4)_{0.9}H(PO_3H)$ , waar de onset-temperatuur van de superprotonisch faseovergang wordt waargenomen bij de lage temperatuur van  $67\text{ }^\circ\text{C}$ , in vergelijking met  $125\text{ }^\circ\text{C}$  en  $127\text{ }^\circ\text{C}$  zoals waargenomen wordt voor respectievelijk  $KH(PO_3H)$  en  $(NH_4)H(PO_3H)$  (ofschoon opgemerkt moet worden dat voor de gegeven samenstelling twee superprotonische overgangen worden waargenomen, naast die bij  $67\text{ }^\circ\text{C}$  eveneens één bij  $114\text{ }^\circ\text{C}$ ). De waarnemingen wijzen erop dat in vaste oplossingen van vaste zuren de waterstofbruggen ofwel verzwakt zijn ten opzichte van die in de oorspronkelijke verbindingen, ofwel gebroken. In tegenstelling tot  $K_{1-x}(NH_4)_xH(PO_3H)$ , leidt isovalente vervanging van  $Cs^+$  voor  $K^+$  in  $KH(PO_3H)$  tot een significante verhoging van de geleiding bij lagere temperaturen.

In **hoofdstuk 5** wordt de invloed van de waterdampdruk,  $p_{H_2O}$ , op de performance van poreuze Pt/ $KH(PO_3H)$  elektroden op  $KH(PO_3H)$ - $SiO_2$  ( $\omega = 0.1$ ;  $d_p \approx 14\text{ nm}$ ) bestudeerd met AC impedantie spectroscopie. Gevonden wordt dat bij  $142\text{ }^\circ\text{C}$  de elektrodereactie bestaat uit drie snelheidsbepalende processen, elk sterk afhankelijk van de  $p_{H_2O}$ , ofschoon hun oorsprong niet opgemaakt kan worden uit de gegevens van de experimenten. Een opmerkelijke waarneming is dat de protonengeleiding van het composiet dat als elektrolyt gebruikt wordt sterk verbetert bij een toename van  $p_{H_2O}$ , terwijl dit niet gevonden wordt voor fasezuiver  $KH(PO_3H)$  of  $SiO_2$ . De waarneming wordt in verband gebracht met een snel transport van protonen langs  $KH(PO_3H)/SiO_2$  interfaces, mogelijk gemaakt door  $H_2O$ -moleculen.

**Hoofdstuk 6** sluit de werkzaamheden beschreven in dit proefschrift af met een vooruitblik op de mogelijke toepassing van vaste zuren als elektrolyt in brandstofcellen en met voorstellen voor aanvullend onderzoek. Geconcludeerd wordt dat (i) consolidatie en thermo-mechanisch gedrag van het elektrolyt, met het oog op mogelijke  $H_2$  cross-over, (ii) de rol van  $H_2O$  en dat van de



microporositeit van het SiO<sub>2</sub> nanopoeier dat als dispergeermiddel gebruikt wordt op de protonengeleiding van het composiet-elektrolyt KH(PO<sub>3</sub>H)-SiO<sub>2</sub>, en (iii) fabricage en controle over de morfologie van katalysator-elektroden, behalve dat zij wetenschappelijke uitdagingen zijn, beslist meer aandacht verdienen.

Tenslotte, wordt in de **bijlage** van dit proefschrift, een een-pot water-in-olie ‘omgekeerde micro-emulsie’ techniek beschreven, waarmee op generieke manier nanodeeltjes van de in water oplosbare vaste zuren gemaakt kunnen worden. De methode wordt gebruikt voor de bereiding van ultrananokristallijn CsHSO<sub>4</sub> (0,6 - 2,5 nm).

## **Reference**

1. S. Unnikrishnan, Micromachined Dense Palladium Electrodes for Thin-film Solid Acid Fuel Cells, PhD Thesis, University of Twente, Enschede (2009).



## Acknowledgement

After a four-year long, challenging, intensive, and fruitful life in Inorganic Membranes Group, finally, everything tends to the calm end. It is not easy indeed, but I GET it with all the encouragement and supports from my dear colleagues, friends, and family. In this section, I would like to express my heartfelt gratitude to all the persons who, by any means, helped me in my research and daily life.

First of all, I would like to thank Prof. Matthias Wessling and Prof. Arian Nijmeijer who gave me this great opportunity to realize my academic ambition and perform my doctoral research at the University of Twente.

My special gratitude must be expressed to my supervisor, Henny Bouwmeester. I am really amazed at his enthusiasm in chemistry and strictness in research. He is an energetic “captain” to guide our research group. His kind email, regardless for our discussion or reading reference, could come into my mail box 24-7, including at the midnight during the weekend. I really appreciate his helpful guidance in scientific exploration and great efforts in correcting my theses. Besides, I also would like to thank Bernard Boukamp and Louis Winnubst for their attentive care in helping me laid a solid foundation in the theoretical studies of fuel cell.

Rome was not built by one person alone, and neither will my research project. I appreciate the good coordination with my working partners, Aliaksandr Bandarenka and Sandeep Unnikrishnan. Thanks for their activeness in the project discussions and great patience for the experimental results. My appreciation also goes to our kind technicians, Frank Morssinkhof, Mieke Luiten-Olieman and Cindy Huiskes for their helpful advices and technical assistance for my laboratory work. I also want to thank my great colleagues,

Chunlin Song, Jianxin Yi, Hong Qi, Chung-Yul Yoo, Schwan Hosseiny, Zeynep Kanlıdere, and all the members and pre-members of our IM group. Without their kind help, encouragement and supports, I cannot achieve today's success. Thanks for our excellent secretary, Susanne van Rijn. She is really a professional expert to handle all the tough "troubles" that I met in the working life. And I also have to appreciate our outstanding "language experts" and "local guiders", Chielant, Martin and Emiel. With their great patience in translating all the stuff that I could not understand, either in Dutch or German, I adapted to the local life quickly and smoothly.

Furthermore, I would like to thank Gaby Janssen, Henri Jansen and all the committee members in my research project for their strategic suggestions and helpful advices. It is also important to express my gratitude to the University of Twente and STW for their sponsorship and supports in my doctoral research project.

Five working days and two weekend days consist of a whole week. It is my friends that make my life more colorful in Enschede beyond working hours. Kamloon Fow is the first friend I would like to thank since he helped me finalize all the graduation procedures in the National University of Singapore, including collecting my master degree diploma there. Without his help, there is no way for me to start the doctoral project. My appreciation also should be given to my dear friends: Yelei Zhang, Yizhi He, Xiaoquan Zhao, Xiaofeng Sui, Yuying Gao, Lixian Xu, Hao Gu, Lanti Yang, Tian Gang, Qi Chen, Yujie Ma, Meng Wang, Peng Zhang, Tingting Luan and all the others that I have ever met in the Netherlands.

At last, my deepest gratitude must go to my family. Great thanks for my parents to successively support and encourage me even if they live more than 7,000 kilometers away from the Netherlands. I am very proud to inherit the chemist's career from my father. It is he who initially leads me into this

wonderful research field and keeps me inspired to pursue innovative ideas. Thanks for their successive supports and encouragement for my research. Qiwei He, my dearest wife, is the most fascinating woman I have ever met. Her patience, understandings, consideration and great love make me brave to confront various challenges and to ultimately realize my ambition. Darling, I love you forever!

*Weihua Zhou*

周卫华

*January, 2011*

*Enschede, the Netherlands*